



Diese Dissertation haben begutachtet:

Prof. Dr. Antoni Szczurek

Prof. Dr. Klaus Reygers

DISSERTATION

Dielectron production and a search for highly-charged particles in Pb–Pb collisions

Ausgeführt zum Zwecke der Erlangung des akademischen Grades eines Doktors der Naturwissenschaften unter Leitung von

Prof. Dr. Eberhard Widmann
Stefan-Meyer Institut für subatomare Physik
der Österreichischen Akademie der Wissenschaften

eingereicht an der Technischen Universität Wien Fakultät für Physik

von
DI Sebastian Lehner
Matr.-Nr. 0755679
Kohlgraben 47/41, 1050 Wien

Ort, Datum

Unterschrift



Die approbierte gedruckte Originalversion dieser Dissertation ist an der TU Wien Bibliothek verfügbar.
The approved original version of this doctoral thesis is available in print at TU Wien Bibliothek.

Zusammenfassung

Relativistische Schwerionen-Kollisionen erlauben es Materie und fundamentale Kräfte unter den extremsten Temperaturen, Dichten und elektromagnetischen Feldern, die in Laboratorien erreichbar sind, zu untersuchen. Analysen dieser Kollisionen geben einzigartige Einblicke in die Entstehung von Materie und in das Quark-Gluon Plasma (QGP), einen exotischen Materiezustand, von dem angenommen wird, dass er $\sim 10^{-6}$ Sekunden nach dem Urknall im Universum vorherrschend war. Dielektronen (e^+e^-) werden in jeder Phase dieser Kollisionen produziert. Sie erreichen die Detektoren, ohne signifikant von dem ebenfalls produzierten, stark wechselwirkenden Medium beeinflusst zu werden. Daher stellen sie eine ideale Möglichkeit dar, Schwerionen-Kollisionen zu untersuchen. Dielektronanalysen liefern experimentelle Daten zu thermischer Strahlung des QGPs, der partonischen Struktur von Nukleonen im Atomkern, chiraler Symmetriebrechung und der Produktion von Materie durch elektromagnetische Felder.

Die größte Herausforderung in der Analyse von Dielektronen ist der überwältigend große Hintergrund von Photon-Konversions Prozessen im Detektormaterial in der Nähe des Kollisionpunktes. Teilchenspuren dieser Konversionen führen zu kombinatorischem Hintergrund im gesamten Dielektronen Massenspektrum, welcher das Signal der direkt in der Kollision erzeugten Dielektronen um bis zu drei Größenordnungen übertrifft. Zahlreiche Observablen von Teilchenspuren erlauben es, auf den Konversionsursprung eines Teilchens rückzuschließen. Dieser Umstand motiviert eine multivariate Klassifikation von Konversions-Teilchenspuren mit maschinellem Lernen. Die Anwendung dieser Methode vergrößert die statistische Signifikanz des gemessenen Signals im Vergleich zu konventioneller, Schnitt-basierter Hintergrundreduktion.

In der vorliegenden Analyse wird Dielektronen-Produktion differenziell im transversalen Paar-Impuls untersucht. Dies ist motiviert durch einen kürzlich gefundenen Dielektronenüberschuss in Au–Au Kollisionen am Relativistic Heavy Ion Collider (RHIC). Die vorherrschende Erklärung dafür ist Dielektronen Photoproduktion, ein Prozess in dem Dielektronen durch das elektromagnetische Feld der Kollision erzeugt werden. Die spärlich vorhandenen experimentellen Daten sind jedoch nicht vollständig mit entsprechenden Modellberechnungen kompatibel. Es wird vorhergesagt, dass dieses Phänomen auch in Pb–Pb Kollisionen mit dem ALICE Detektor am Large Hadron Collider beobachtbar ist. In dieser Arbeit werden die entsprechenden Dielektronen Spektren extrahiert. Ein Überschuss im Vergleich zu den erwarteten hadronischen Quellen wird gefunden. Er stimmt weitgehend, aber nicht vollständig, mit den Erwartungen für Photoproduktion überein.

Diskrepanzen zwischen den Daten und den Modellen für Dielektronen-Photoproduktion am RHIC führten zu Spekulationen über soweit noch nicht be-

rücksichtigte zusätzliche Effekte. Diese hängen mit Streuung von Leptonen im QGP, Ablenkung durch das äußerst starke Magnetfeld oder der Ausdehnung der Atomkerne zusammen. Jedes dieser Szenarien postuliert eine Abhängigkeit der Dielektron-Photoproduktion von der Richtung relativ zur Reaktionsebene der Kollision. In dieser Arbeit werden erste vorläufige Resultate einer entsprechenden Analyse präsentiert.

Ein weiteres Projekt in dieser Arbeit befasst sich mit der Suche nach magnetischen Monopolen. Die Abwesenheit solcher Teilchen stellt eher einen empirischen Befund als eine Notwendigkeit der derzeit bekannten physikalischen Gesetze dar. Zudem lieferte Dirac eine ansprechende theoretische Motivation für deren Existenz. Er zeigte, dass sie einen weiteren, theoretisch unverstandenen Umstand, nämlich die Quantisierung elektrischer Ladungen, erklären würden. Suchen nach Monopolen blieben bislang erfolglos. In der Vergangenheit war es nicht möglich, von diesen Suchen allgemein gültige untere Schranken für die Masse magnetischer Monopole abzuleiten. In Suchen nach Monopolproduktion in Teilchenkollisionen ist es notwendig, die zu erwartende Produktionsrate zu berechnen, um Schranken auf die Masse setzen zu können. Dies ist momentan nicht möglich, da störungstheoretische Berechnungsmethoden nicht auf dieses Problem anwendbar sind. Wie kürzlich vorgeschlagen wurde, kann diese Problematik im Prinzip umgangen werden, wenn man Monopolproduktion in starken magnetischen Feldern betrachtet. Da die Magnetfelder in Schwerionen-Kollisionen für die stärksten im heutigen Universum gehalten werden, gelten sie als ideale Gelegenheit für Suchen nach Monopolen. Zusätzlich wäre es prinzipiell noch möglich, von diesen Suchen allgemein gültige Massenschranken abzuleiten.

Eine entsprechende Monopol-Suchstrategie in Schwerionen-Kollisionen mit ALICE wird in der vorliegenden Arbeit entwickelt. Aufgrund der zu erwartenden exotischen Eigenschaften der Monopole ist es schwierig, das Ziel der Suche in den Detektordaten festzulegen. Es stellt sich heraus, dass Kernfragmente, die im Detektor stoppen, ein ähnliches Signal verursachen sollten. Sie können daher bei der Definition der Suchkriterien Daten-basierte Aufschlüsse liefern. Die erfolgreiche Identifikation solcher Teilchenspuren in den Detektordaten demonstriert die Machbarkeit der vorgesehenen Suche nach Monopolen.

Abstract

Relativistic heavy-ion collisions offer a way to study matter and fundamental forces under the most extreme temperatures, densities, and electromagnetic fields accessible in laboratories. Analyses of these collisions provide unique insights into the physics governing the creation of matter and the Quark Gluon Plasma (QGP), an exotic state of matter expected to have been prevalent in the Universe at $\sim 10^{-6}$ seconds after the Big Bang. Dielectrons (e^+e^-) are produced at each phase of the collisions. They reach the detectors without being significantly affected by the strongly interacting medium, which is also created in the collision. Therefore, they offer an ideal opportunity to examine heavy-ion collisions. Analyses of dielectrons provide experimental input to questions regarding thermal radiation of the QGP, the partonic structure of nucleons in nuclei, chiral-symmetry restoration, and the production of matter by electromagnetic fields.

The main challenge in the analysis of dielectron production is the overwhelming background originating from photon-conversion processes in the detector material close to the interaction vertex. Tracks from these conversions lead to combinatorial background in the whole dielectron mass spectrum which exceeds the signal of dielectrons produced directly in the collision by up to three orders of magnitude. Numerous track observables can be used to infer the conversion origin of a track. This motivates a multivariate classification of conversion tracks using machine learning. Applying this method enhances the statistical significance of the measured dielectron signal in comparison to conventional cut-based background rejection.

In the presented analysis dielectron production is studied differentially in the pair transverse momentum. This is motivated by the recently reported dielectron excess in Au–Au collisions at the Relativistic Heavy Ion Collider (RHIC). The prevalent explanation in theoretical studies is dielectron photo-production, a process in which a dielectron is produced from the electromagnetic field in the collision. However, the scarce experimental data related to this phenomenon is not completely in line with corresponding model calculations. It is predicted that this phenomenon is observable in Pb–Pb collisions with the ALICE detector at the Large Hadron Collider. In this work the corresponding dielectron spectra are extracted. An excess with respect to the expected hadronic sources is found. It agrees to a large extent, but not entirely, with expectations for photo-production.

Discrepancies between data and models for dielectron photo-production at the RHIC led to speculations about so far not considered additional effects. These are related to rescattering of leptons in the QGP, deflections due to the extremely strong magnetic field, or effects of the finite nucleus size. All of these scenarios posit a dependence of dielectron photo-production on the direction relative to the

reaction plane of the collision. In this thesis first preliminary results of a corresponding analysis are presented.

A further project in this thesis deals with the search for magnetic monopoles. The absence of these particles represents rather an empirical finding than a necessity of the presently known laws of physics. In addition, Dirac provided appealing theoretical motivation for their existence. He showed that they would lead to understanding of another, theoretically unanticipated, empirical finding, namely that electric charges are quantised. Searches for monopoles were unsuccessful so far. Deriving robust lower limits for the magnetic monopole mass from these searches was not possible in the past. In searches for monopole production at colliders, setting mass limit requires the calculation of the expected monopole production rates. This is currently not possible as perturbative methods cannot be applied to this problem. It was recently found that this issue can in principle be circumvented by considering monopole production in strong magnetic fields. Since heavy-ion collisions are widely believed to produce the strongest magnetic field in the present Universe, they were proposed as a promising opportunity for searches, which could be interpreted in terms of rigorous mass limits.

A corresponding strategy for a monopole search in heavy-ion collisions with ALICE is developed. Due to the expected exotic properties of monopoles, a key problem is to define the search target in the detector data. It is found that nuclear fragments which stop in the detector should yield a comparable detector response. They can therefore provide data-driven guidance for the definition of search criteria. The successful identification of corresponding particle tracks in detector data demonstrates the feasibility of the foreseen monopole search.

Danksagung

Zuallererst möchte ich Eberhard dafür danken, dass er es mir ermöglichte diese Arbeit am Stefan-Meyer Institut anzufertigen. Schon während meines Diplomstudiums nahm er maßgeblich Einfluss auf meine wissenschaftlichen Interessen. Darüber bin ich rückblickend äußerst glücklich, nicht zuletzt auch weil ich dadurch zu meiner Doktorandenstelle kam.

Michael stellte mich als erstes Mitglied seiner neu gegründeten Gruppe an. Egal ob Fragen zur Physik, Organisatorisches oder technische Angelegenheiten, er bewies stets schier endlose Geduld mir mit Problemen aller Art weiterzuhelfen. Mein Arbeitsplatz an seinem Nebentisch war daher zumindest für mich eine ideale Wahl. Zusätzlich ermöglichte er es mir eigene Ideen zu verfolgen und war dabei stets eine große Unterstützung. Für das und vieles mehr gebührt ihm meine vollste Dankbarkeit.

Hervorheben möchte ich auch das Kollegium unter den Studenten an unserem Institut. Ihr habt dafür gesorgt, dass der Spaß nie zu kurz kam.

Dem Doktoratskolleg - Particles and Interactions danke ich für das vielseitige und hervorragend zusammengestellte Angebot an schools und retreats.

Meiner Freundin Petra danke ich für ihre cleveren Ratschläge zu meinen nachhause mitgebrachten Problemen und ganz viel mehr. Ohne dich wäre der bisherige Weg nicht so ein schöner gewesen, du lässt mich zuversichtlich in die Zukunft blicken.

Zu guter Letzt möchte ich den Menschen zutiefst danken, die schon immer für mich da waren, meiner Familie. Meine Eltern und Großeltern haben es mir ermöglicht, regelmäßig der Arbeit in Kurzurlauben auf das Land zu entfliehen, um dort den Kopf frei zu bekommen. Auch mein Neffe Clemens erleichtert mir dies stets ungemein, wofür ich ihm und seinen Eltern äußerst dankbar bin.

*Everything we call real is
made of things that cannot
be regarded as real.*

Niels Bohr

Contents

1. Introduction	1
2. Aspects of quantum chromodynamics	3
2.1. Deconfinement	6
2.2. Chiral symmetry	8
3. Heavy-ion collisions	11
3.1. Collision geometry	13
3.2. Dileptons	17
3.2.1. Low-mass dielectrons	18
3.2.2. Intermediate-mass dielectrons	23
3.3. Electromagnetic interactions in heavy-ion collisions	24
3.3.1. Previous experimental results	27
3.3.2. Theoretical approaches	34
3.4. Magnetic monopoles	40
3.4.1. Theoretical perspective	40
3.4.2. Search techniques	45
3.4.3. Overview of experimental searches	46
4. The ALICE detector	49
4.1. Particle identification	51
5. Analysis of dielectrons	55
5.1. Monte Carlo simulations	56
5.2. Dataset and event selection	57
5.3. Signal and background definitions	59
5.4. Track selection	61
5.4.1. Standard selection cuts	61
5.4.2. Preselection cuts	64
5.4.3. BDT based photon-conversion rejection	66
5.5. Pair analysis	74
5.5.1. Benchmark for BDT based conversion rejection	76
5.5.2. Efficiency correction	78

5.6. Hadronic cocktail	80
5.7. Model calculations	83
5.8. Dielectron $p_{T,ee}$ spectra in 70–90% centrality	87
5.8.1. Efficiency correction	87
5.8.2. Result selection and systematic cut uncertainty	91
5.8.3. Results	97
5.9. Dielectron $p_{T,ee}$ spectra in 0–40% centrality	97
5.9.1. Results	101
5.10. Event plane differential spectra	103
5.11. Cross-checks	107
5.11.1. PID contamination	107
5.11.2. Cut selection bias	109
5.11.3. Like-sign subtraction	111
5.12. Discussion and outlook	112
6. A search strategy for highly-charged particles	114
6.1. Concept	115
6.2. Data structure	118
6.3. Demonstration	119
6.4. Discussion and outlook	123
7. Conclusion	125
A. Kinematic variables	126
Bibliography	i



Die approbierte gedruckte Originalversion dieser Dissertation ist an der TU Wien Bibliothek verfügbar.
The approved original version of this doctoral thesis is available in print at TU Wien Bibliothek.



Die approbierte gedruckte Originalversion dieser Dissertation ist an der TU Wien Bibliothek verfügbar.
The approved original version of this doctoral thesis is available in print at TU Wien Bibliothek.

1. Introduction

As one of the three interactions in the Standard Model of particle physics, the strong interaction is a central pillar of fundamental physics. For instance, only 1–2% of the mass in baryonic matter¹ can be attributed to interactions with the Higgs field, leaving the vast majority to the dynamics of the strong interaction. The absence of free and fundamental strongly interacting particles is one of the reasons why the strong interaction was discovered much later than the electromagnetic force. This can be related to another peculiarity of this force. The phenomenon of confinement asserts that strongly interacting, fundamental particles do, under conditions common in the present Universe, not exist as free particles but are bound in composite particles. In these particles, called hadrons, the strong interactions of the constituent particles is limited to very short distances which impedes its detection at macroscopic distances. These two examples and several more in fields like cosmology, astro-, particle- and nuclear-physics motivate the extensive scientific efforts put into ongoing studies of the phenomenology of the strong interaction using heavy-ion collisions (HICs).

Chapter 2 provides a brief introduction to the theory of the strong interaction and relevant associated phenomena. Chapter 3 introduces general concepts in the analysis of HICs. An overview of results in the context of dielectrons is given in Section 3.2.

Besides the strong interaction, colliding nuclei interact via the electromagnetic force. Corresponding processes lead to dielectron production from photon-photon interactions, the so-called photo-production. Associated experimental results are scarce and not completely understood from a theoretical point of view, which may indicate the presence of so far not considered effects. An overview of the status of this field is given in Section 3.3.

Data used for the analysis in this thesis are taken and processed by the ALICE experiment at the Large Hadron Collider (LHC). An overview of the ALICE detector is provided in Chapter 4.

The analysis of dielectrons and the corresponding results are presented and discussed in the context of photo-production in Chapter 5.

¹Baryonic matter constitutes practically all the mass of the luminous matter (i.e. excluding dark matter) we know.

As electromagnetic interactions can produce dielectrons, i.e. an electric monopole-antimonopole pair, they should in principle be able to create a magnetic monopole-antimonopole pair. Indeed, theoretical studies indicate that the ultra strong magnetic field of the colliding nuclei in HICs provides an ideal opportunity for magnetic monopole searches. More details on this aspect of HICs are provided in Section 3.4.1 and a strategy for a search of magnetic monopoles in HICs is given in Chapter 6.

2. Aspects of quantum chromodynamics

The quantum field theory underlying the strong interaction is Quantum Chromodynamics (QCD). Its Lagrangian describes the fundamental fields and their interactions:

$$\mathcal{L} = \bar{\psi}_f^\alpha \left[i\gamma^\mu \partial_\mu \delta_{\alpha\beta} - \frac{g}{2} (\lambda_a)_{\alpha\beta} \gamma^\mu A_\mu^a + m_f \delta_{\alpha\beta} \right] \psi_f^\beta - \frac{1}{4} G_{\mu\nu}^a G_a^{\mu\nu}, \quad (2.1)$$

where ψ_f^α denotes fermionic degrees of freedom of spin 1/2, represented by four-component Dirac spinors. These quantum fields correspond to quarks of flavour f and colour¹ $\alpha \in \{1, 2, 3\}$. The Dirac matrices γ^μ act in the space of these spinors. A guiding principle in the construction of this Lagrangian is gauge invariance with respect to local SU(3) gauge transformations. As a result the quark fields couple to the gauge boson field A_μ^a , which represents gluons. The term in which A_μ^a appears explicitly also contains the matrices $(\lambda_a)_{\alpha\beta}$, indicating that the gluon field couples quark fields of colours α and β . These matrices are the Gell-Mann matrices, which are enumerated by $a \in \{1, \dots, 8\}$. The strength of the quark–gluon interaction is set by the coupling strength parameter g . The mass of the quarks of flavour f is defined by m_f .

$G_{\mu\nu}^a$ is the gluon field strength tensor, which is defined as:

$$G_{\mu\nu}^a = \partial_\mu A_\nu^a - \partial_\nu A_\mu^a + gf_{bc}^a A_\mu^b A_\nu^c, \quad (2.2)$$

where f_{bc}^a are the structure constants of SU(3). The last term in Eq. (2.1) gives rise to self-interactions among the gluon fields. The self-interaction of gauge bosons is a key difference between QCD and Quantum Electrodynamics (QED), the quantum field theory of electromagnetism. The Lagrangian of QED is constructed from a different group, U(1), which does not give rise to a term representing interactions among the QED gauge bosons, the photons. As discussed in the next two sections

¹In the context of QCD the term “colour” refers to a property of particles that can be thought of as a generalisation of the concept of electromagnetic charge, to more than two possible charge states.

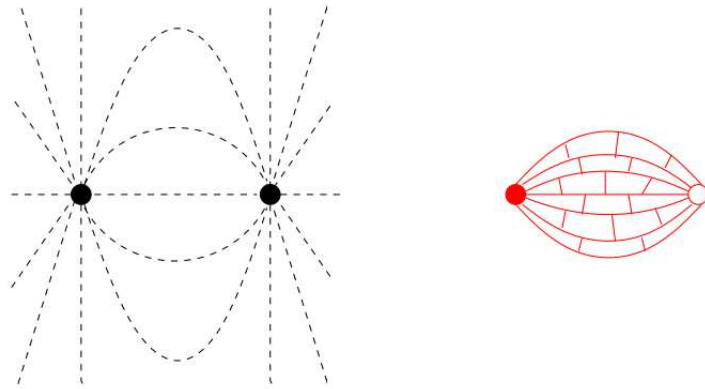


Figure 2.1.: Left: The electromagnetic field lines between attracting electric charges. Right: The field lines between two colour charges [3].

these self-interactions of gauge bosons play a key role in the striking differences between the phenomenology of QCD and QED.

Field lines of two attracting electromagnetic charges are spreading out from the charges radially (see Fig. 2.1 left). For colour charges like quarks the gluon self-interaction leads to a collimation of field lines between the charges (see Fig. 2.1 right). This field configuration is often called a “string” and provides an intuitive picture² of one of QCD’s most distinguishing phenomena, confinement. Since the number of field lines connecting two quarks remains constant as their distance r increases, the potential $V(r)$ between them is approximately linear [1]:

$$V(r \rightarrow \infty) \propto \sigma \cdot r. \quad (2.3)$$

Here σ (also called “string tension”) sets the strength of the force between the quarks in the limit of large r . As a quark antiquark pair ($q\bar{q}$) is pulled apart the potential energy increases, until the field switches into an energetically more favourable state at some critical point by producing a new $q\bar{q}$ pair between the original ones [2]. This mechanism prevents the production of free individual quarks and anti-quarks.

Gluon self-interaction turns out to also be a key ingredient for a closely related feature of QCD. Quantum effects lead to a dependence of the coupling strength g on the energy scale [4, 5]. The gluon fluctuations surrounding a colour charge can be imagined to lead to an anti-screening effect. Thus, the effective colour charge becomes smaller as the probed distance decreases. Expressed in different terms, this implies that in scattering experiments with hadrons the strong coupling be-

²Despite the development of models of confinement, it can so far not be deduced from first principles, i.e. from Eq. (2.1).

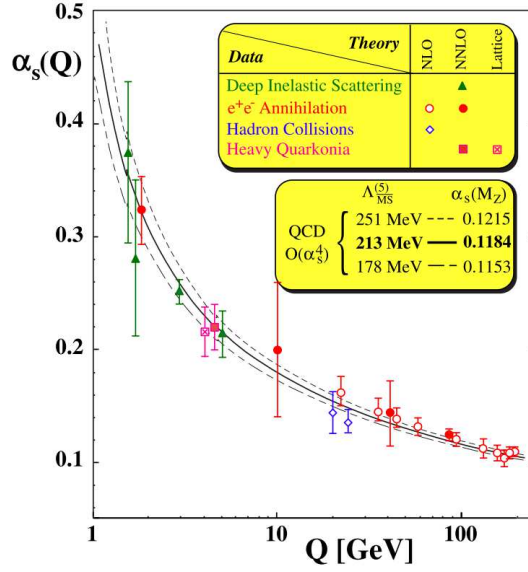


Figure 2.2.: Comparison of various measurements of α_s to theory predictions (lines) at different momentum transfer scales Q . The energy scale at which $\alpha_s(Q^2)$ diverges is denoted by $\Lambda_{\overline{MS}}^{(5)}$. NLO and NNLO represent the order to which calculations of the measured observables are carried out and M_Z is the mass of the Z boson and indicates the energy scale at which α_s is evaluated in the lower legend. See [6] for further details.

comes small at increasingly high momentum transfers. This phenomenon is known as asymptotic freedom. Conversely, the coupling strength increases with large distances and low momentum transfers. Figure 2.2 shows the comparison of measurements and theory predictions of the QCD fine structure constant $\alpha_s = g/(4\pi)$ as a function of the momentum transfer Q . This dependence of the coupling strength on the momentum scale is a distinguishing feature related to the SU(3) gauge group underlying QCD. For instance, it would be steeper for SU(4) and flatter for SU(2) [1].

Perturbative methods in QCD are not applicable to phenomena at energy scales below ≈ 1 GeV, which are the realm of confinement (see Section 2.1) and chiral symmetry breaking (see Section 2.2) [7]. Currently such calculations are only possible using lattice QCD. In this method space-time is discretised, which reduces the infinite number of degrees of freedom (DoF) of a continuous field to a finite number of DoF on a space-time lattice. Gauge invariance is maintained in this approximation, which allows this method to incorporate the interactions corresponding to gauge theories like QCD and QED. Physical results are obtained in the continuum limit, i.e. by extrapolating the result to the case of vanishing lattice spacing [7].

2.1. Deconfinement

Following the discovery of asymptotic freedom a new state of strongly interacting matter was conjectured to exist at sufficiently high temperatures and densities [8,9]. This can be derived intuitively from asymptotic freedom since with increasing temperature of a hadron gas the average momentum of individual hadrons rises. According to asymptotic freedom this should ultimately lead to vanishing interactions in the plasma. Similarly, at high hadron densities hadrons will start to overlap and individual quarks are able to move through the dense medium. This argument of overlapping hadrons provides an alternative picture of the connection between high temperatures and deconfinement. As the temperature of a hadron gas is increased and becomes relativistic, not only does the strong interaction become weaker but also additional hadrons are produced and deconfinement sets in as the hadron density increases. From this perspective high hadron density can be regarded as a decisive condition for the transition to a deconfined state. Apart from high temperatures, also compression can be used to obtain high hadron densities. A state of compressed baryonic matter is present in neutron stars and nuclear collisions at center-of-mass energies per nucleon of approximately $\sqrt{s_{NN}} \approx 10$ GeV. In contrast to these states, high-temperature states like in the early Universe or in HICs at the LHC, are characterised by almost zero net-baryon density. In thermodynamics the net-baryon density of the system is reflected by the baryochemical potential, which represents the energy required to add a nucleon to the system [2,3]. This quantity rises with the net-baryon density and thus controls the imbalance between quarks and anti-quarks. A vanishing baryochemical potential indicates balance between quarks and anti-quarks.

The state of deconfined quarks and gluons is commonly referred to as the Quark Gluon Plasma (QGP). Lattice QCD results support the expectation of this deconfinement transition at vanishing baryochemical potential. Under these conditions the critical temperature of the deconfinement transition is predicted to be $T_c \approx 150$ MeV [10].

The so-called QCD Phase Diagram (see Fig. 2.3) provides an overview of the present expectation of the states of QCD matter as a function of the baryochemical potential and the temperature. In addition to the hadron gas and the QGP phase, a colour superconducting phase is indicated at low temperature and high baryochemical potential. This theorised state consists of diquarks which resemble Cooper pairs in superconductors. Carrying colour charge, these diquarks could

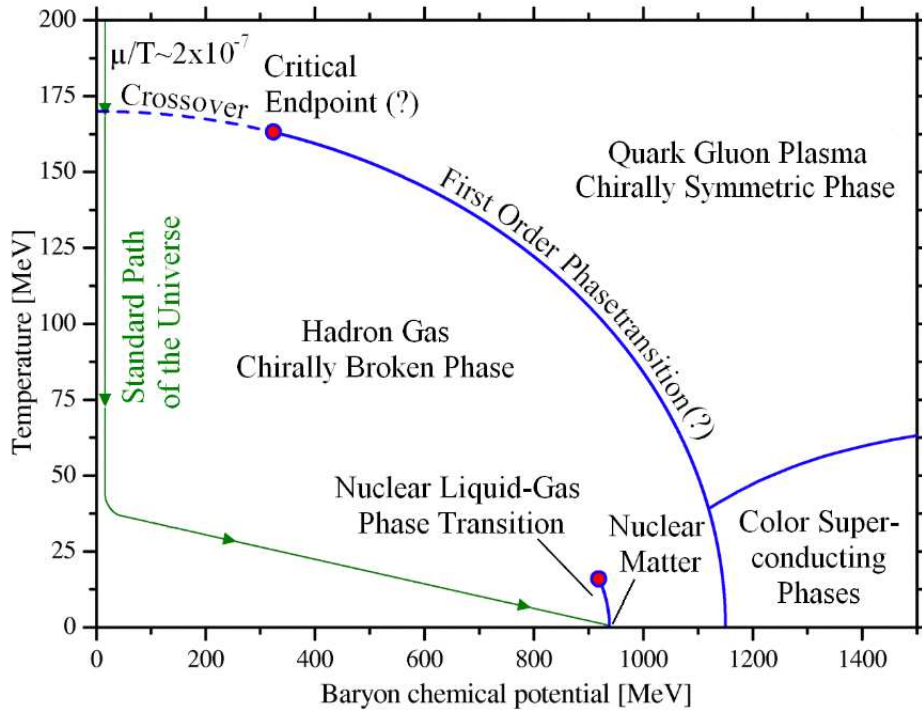


Figure 2.3.: The QCD phase diagram [11].

lead to colour-superconductivity. Lattice results suggest that at low net-baryon density (i.e. low baryochemical potential) the phase transition is a continuous cross-over. With increasing density the transition is expected to become more abrupt until it becomes a first order phase transition at the so-called critical endpoint [2, 10, 12].

This transition indicates a maximum temperature for the existence of hadrons. At this point it is worthwhile pointing out that before QCD (1964) and asymptotic freedom (1973) were established very similar temperature limits had already been conjectured. In 1951 Pomeranchuk predicted a maximum temperature of $T_c \approx 200$ MeV [13]. The derivation is based on a finite hadron size and the resulting maximum density for a pion gas. However, this result remained widely unnoticed until Hagedorn reached a compatible conclusion from a different approach. In the 1960's it was found experimentally that with increasing mass the density of hadronic states with given quantum numbers rises. Motivated by this observation Hagedorn developed a model [14] to describe the number of hadronic resonances per mass interval, i.e. the resonance density $\rho(m)$ at a mass m . The model is built on the picture that a heavy resonance consists of lighter resonances, whose four-momenta add up to the one of the heavy resonance. All resonances except the lightest one are assumed to be composed in this way. The possible ways

to compose heavy resonances from lighter ones are determined by the available hadronic states at lower mass. Thus, $\rho(m)$ at the mass of the heavy resonance can be determined only with knowledge of $\rho(m)$ at lower masses. The resulting self-similar structure leads to an exponential growth in the density of states with mass:

$$\rho(m) \propto m^{-3} e^{\frac{m}{T_H}}, \quad (2.4)$$

where the parameter T_H is called Hagedorn temperature. Using Eq. (2.4) it can be shown that as the hadron gas temperature T rises and $T \rightarrow T_H$ an increasing fraction of the added energy is used to produce more particles of ever larger masses and consequently a smaller energy fraction is used to increase the temperature of the gas. Consequently, the required energy to reach T_H diverges and T_H represents the maximum temperature. The value of T_H can be related to the range of the strong interaction. A corresponding estimation yields $T_H \approx 200$ MeV [15].

2.2. Chiral symmetry

The large discrepancy between the π^0 mass ($m_\pi = 135$ MeV/ c^2) and the corresponding current quark masses³ ($m_{u,d} \approx 1.8 - 5.2$ MeV/ c^2), associated to the constituent up and down quarks, reveals that additional mass is generated dynamically in the confined state [10]. This suggests a connection between confinement and mass generation.

The mass term in Eq. (2.1) is the only term which is not invariant under the axial-vector transformation of a isospinor ψ :

$$\psi \rightarrow \lambda_A \psi = \exp(-i\gamma_5 \vec{\tau} \vec{\Theta}) \psi. \quad (2.5)$$

Here γ_5 acts in the Dirac spinor space, $\vec{\tau}$ is a vector of Pauli matrices, which act on the isospinors $\psi^T = (\psi_u, \psi_d)$, where $\psi_{u,d}$ are the Dirac spinors for up and down quarks. The direction of the isospin rotation of λ_A is defined by $\vec{\Theta}$. Since γ_5 is related to the handedness of a state, called chirality, the transformation Eq. (2.5) is called a chiral transformation [16].

Chiral symmetry of Eq. (2.1), which encompasses invariance with respect to λ_A , is violated by the non-vanishing quark masses, i.e by the term $m_f \delta_{\alpha\beta} \bar{\psi}_f^\alpha \psi_f^\beta$. However, these masses are small in comparison to the energy scale of confinement $\Lambda_{\text{QCD}} \approx 200$ MeV (see Fig. 2.2) and should leave chiral symmetry an approximate symmetry in QCD.

The axial-vector transformation λ_A mixes chiral partners among the vector mesons.

³These are the masses used in Eq. (2.1).

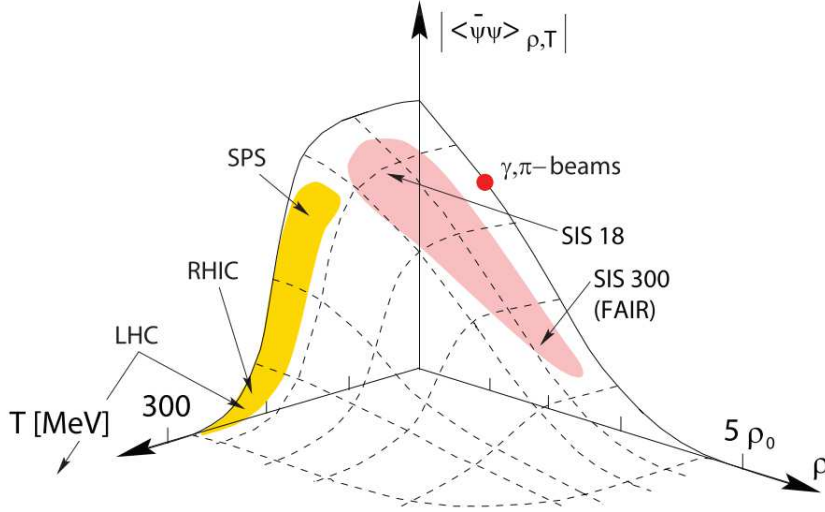


Figure 2.4.: The chiral condensate (z-axis) as a function of the temperature T ($100 \text{ MeV} \approx 10^{12} \text{ K}$) and matter density ρ (in units of the nuclear matter density $\rho_0 \approx 2 \cdot 10^{11} \text{ kg/cm}^3$) according to calculations based on the NJL-model. Coloured regions are accessible at different present and future facilities (SIS 300) [18, 19].

Examples are the states corresponding to ρ and a_1 mesons:

$$\vec{\rho}_\mu \equiv \bar{\psi} \vec{\tau} \gamma_\mu \psi, \quad \vec{a}_{1\mu} \equiv \bar{\psi} \vec{\tau} \gamma_\mu \gamma_5 \psi \quad (2.6)$$

$$\lambda_A \vec{\rho}_\mu = \vec{\rho}_\mu + \vec{\Theta} \times \vec{a}_{1\mu}. \quad (2.7)$$

The large mass gap between the ρ^0 meson ($m_\rho = 770 \text{ MeV}/c^2$) and the a_1 meson ($m_{a_1} = 1260 \text{ MeV}/c^2$) cannot be attributed to the minor violation of chiral symmetry due to the non-vanishing quark masses [17].

Therefore, an additional source of symmetry breaking is required as an explanation. This is provided by the so-called chiral condensate, which represents a finite vacuum expectation value for the density of quark-antiquark pairs $\langle \bar{q}q \rangle$. Similar to the mass term in Eq. (2.1) this term also violates chiral symmetry [10, 17].

The appearance of this condensate was predicted by the Nambu and Jona-Lasinio (NJL) model [20, 21] even before QCD was developed. Based on this model, the disappearance of the chiral condensate at sufficiently high temperature and densities is predicted (see Fig. 2.4), which is supported by more recent lattice calculations [12].

Predictions of the critical temperature at vanishing baryochemical potential for the chiral transition and the deconfinement transition, which are a priori unrelated, yield the same values of $T_c \approx 160 \text{ MeV}$ [7]. This coincidence is regarded as

a possible manifestation of a fundamental, still unknown connection between the two transitions [3, 22].

As illustrated in Fig. 2.4, HICs at present and future facilities probe regions of the QCD phase diagram in which the chiral condensate substantially varies, which shall allow the corresponding experiments to study associated effects.

3. Heavy-ion collisions

There is wide consensus today that experimental data indicate the production of a QGP in HICs. Based on asymptotic freedom, one may expect that the strong interaction becomes weak at $T > T_c$ and thus the plasma produced in HICs exhibits weak coupling. First results from the Relativistic Heavy Ion Collider (RHIC), however, showed signs of strong hydrodynamical collective flow and energy loss of jets in the medium (jet-quenching). Consequently, the data is interpreted today in terms of a strongly coupled QGP. This conclusion is founded on diverse experimental evidence coming from the RHIC and the LHC. Together with theoretical approaches these are reviewed in [23].

The following discusses the picture of the consecutive stages of an HIC, which emerges from experimental results. The focus is placed on hadronic interactions. Electromagnetic interactions are discussed separately in Section 3.3.

1. Initial state: Due to Lorentz contraction the colliding nuclei appear as approaching discs. When the LHC is colliding Pb ions at $\sqrt{s_{NN}} = 5.02$ TeV nuclei are contracted by a factor of $\gamma \approx 2500$. In the center-of-mass rest frame the colliding nuclei appear as discs with a transverse extension of ≈ 14 fm and a longitudinal size of about $14/\gamma$ fm. Due to time dilation the constituents quarks, the virtual quarks, anti-quarks and gluons (which are all collectively referred to as partons) can be viewed as static, colour-charged particles. As the collision energy rises gluons play an increasingly important role (this phenomenon can be regarded as consequence of the gluon-gluon interactions discussed in Chapter 2 [2]). In fact, the initial state of highly relativistic HICs can be modelled as two colliding sheets of gluons.
2. Pre-equilibrium: Immediately after the collision longitudinal colour fields form between the receding nuclei and produce partons which are presumably out of equilibrium. In this fireball partons are expected to be deconfined and a QGP is formed. The partons are subject to strong mutual interactions leading to the development of local equilibrium. Presently the mechanisms and time scales for equilibration are debated [23].

3. Expansion: Once created, the QGP is subject to collective, hydrodynamic expansion. Transversal and longitudinal expansion of the QGP leads to a decrease of the energy density. Thermal energy is primarily transferred into particle production leading to a decrease of temperature [15]. At a critical temperature hadronisation takes place, i.e. partons are bound into hadrons and become confined. The resulting hadron gas continues to expand and cools down. Inelastic collisions, which can change the involved hadron species, lead to the development of a chemical equilibrium. This implies that the relative abundance of hadron species is connected to the temperature and the hadron masses. Once the hadron gas becomes too dilute for these collisions to maintain the equilibrium, the system reaches the so-called chemical freeze-out. The hadron abundances are locked in from this point onwards, except for particle decays, which are accounted for in the interpretation of experimental results. Therefore, the observed hadron abundances can be used to infer in principle the temperature at the chemical freeze-out [10]. Elastic collisions continue past this point and maintain kinetic thermal equilibrium. Once the hadron gas becomes too dilute for these collisions the particles have reached their final momenta. The corresponding temperature can be measured using distributions of kinematic variables of detected particles.

One of the most simple ways to motivate the expectation of a phase transition in HICs is Bjorken's estimate [24], which shall be discussed in the following. It relates the initial energy density ϵ in HICs to the total observed transverse energy density $E_T = \sum_i E(\theta_i) \sin(\theta_i)$ in pseudorapidity η (see Appendix A). Here θ_i denotes the angle of particle i with respect to the beam axis and E the energy measured in the corresponding direction. The underlying model assumes that after the interpenetration of the colliding disc partons are produced in a cylinder that has a transverse area which is defined by the overlap region of the nuclei. In the longitudinal direction (the z -axis is centered at the collision point) this cylinder undergoes a longitudinal Hubble-like expansion, i.e. the z position of a point in the cylinder and its longitudinal velocity v_z are related by $v_z \approx z/t_0$. This expansion lasts for a time period t_0 , which is the typical time it takes after the collision until partons form. Therefore, the z position of particle production and the resulting pseudorapidity η can be related. For relativistic hadrons and small z/t_0 the following relation can be derived:

$$\eta \approx y = \operatorname{arctanh} \frac{p_z}{E} \approx \operatorname{arctanh} \frac{z}{t_0} \rightarrow dz \approx d\eta \cdot t_0, \quad (3.1)$$

where E is the energy of the particle and p_z the z component of its momentum vector. The rapidity is denoted by y (see Appendix A).

This relation is used to express the spatial energy density in terms of the observable transverse energy density in pseudorapidity:

$$\epsilon = \frac{dE_T}{dz} \frac{1}{A} \approx \left. \frac{dE_T}{d\eta} \right|_{\eta=0} \frac{1}{At_0}. \quad (3.2)$$

Typically t_0 is assumed to be approximately 1 fm/c and A is given by the transverse area of the overlap of the colliding nuclei, which depends on the collision centrality (see Section 3.1). For the LHC this results in an estimated transverse energy density of $\epsilon_T \approx 14$ GeV/fm³ [25]. As stated in this reference, this value is an order of magnitude higher than the expected energy density of the deconfinement transition. Consequently, HICs at the LHC are considered as an opportunity to study QCD phenomena like chiral symmetry restoration and deconfinement in the laboratory.

3.1. Collision geometry

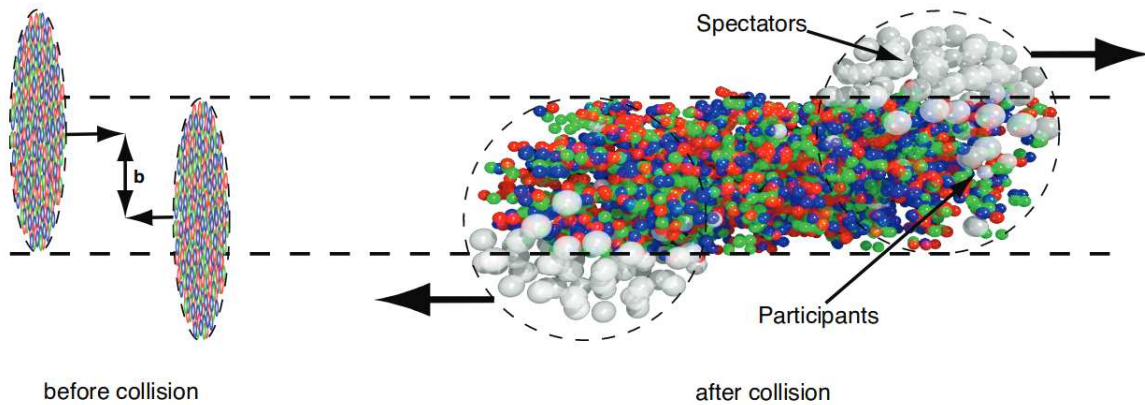


Figure 3.1.: Illustration of the impact parameter (b), participants and spectators in a heavy-ion collision [26].

Numerous aspects of HICs depend on the impact parameter of the collision. This quantity measures the distance between the centers of the colliding nuclei. As illustrated in Fig. 3.1 it determines the expected number of nucleons that participate (N_{part}) in the collision, i.e. which are in the overlap region, and the number of remaining nucleons (N_{spec}). In Glauber Monte Carlo (MC) simulations nuclei are treated quantum mechanically, i.e. based on nuclear density profiles. These simulations are used to obtain the expectation value $\langle N_{\text{part}} \rangle$ as a function of the

impact parameter [27]. In addition, also the average number of binary nucleon-nucleon collisions, $\langle N_{\text{coll}} \rangle$ can be determined with this method. Neither the impact parameter nor N_{part} or N_{coll} can be directly measured, due to the subatomic length scales involved. However, the plausible assumption that the number of charged particles produced in the collision, N_{ch} , rises monotonically with decreasing impact parameter b , implies that percentiles of b correspond to percentiles of N_{ch} . The resulting mapping between the impact parameter (b), $\langle N_{\text{part}} \rangle$ and N_{ch} is illustrated in Fig. 3.2. The percentile to which the events used in an analysis belong is called the centrality. Events corresponding to small (large) b are called central (peripheral), which corresponds to a low (high) centrality.

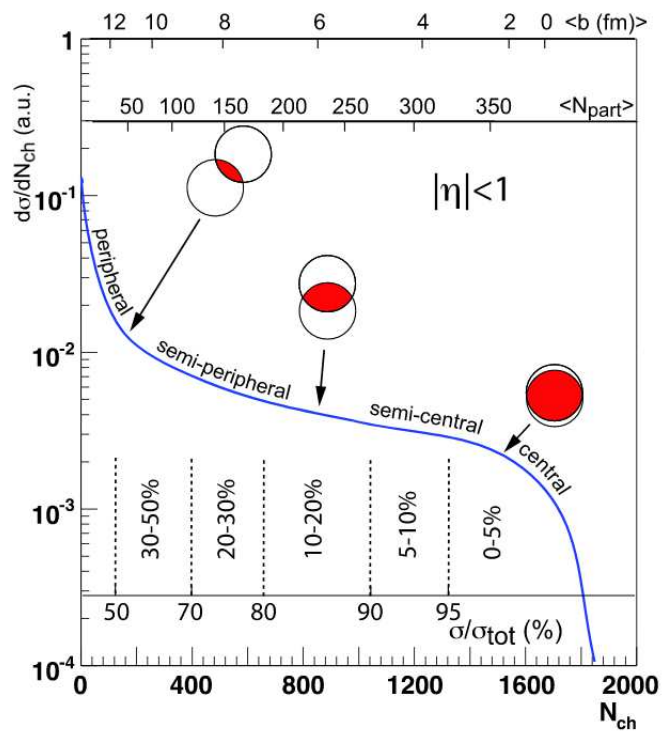


Figure 3.2.: Schematic illustration of the multiplicity (N_{ch}) differential inelastic cross section σ . The various x-axes show the connection between the impact parameter (b), $\langle N_{\text{part}} \rangle$ and N_{ch} [27].

In this analysis the centrality of an event is estimated based on the associated amplitude in the V0 detectors (see Chapter 4), which is approximately proportional to the charged particle multiplicity. A model of particle production that is based on Glauber MC simulations is used to describe the distribution of the charged particle multiplicity [28]. It incorporates hard and soft processes that scale with N_{coll} and N_{part} , respectively, and models the produced charged particle multiplicity

with a Negative Binomial Distribution (NBD). The model parameters are fit to experimental data of the V0 detectors. Based on this fit, the V0 amplitude can be used to estimate the centrality, which can be related to microscopic quantities like b , $\langle N_{\text{part}} \rangle$ and $\langle N_{\text{coll}} \rangle$ (see Fig. 3.3).

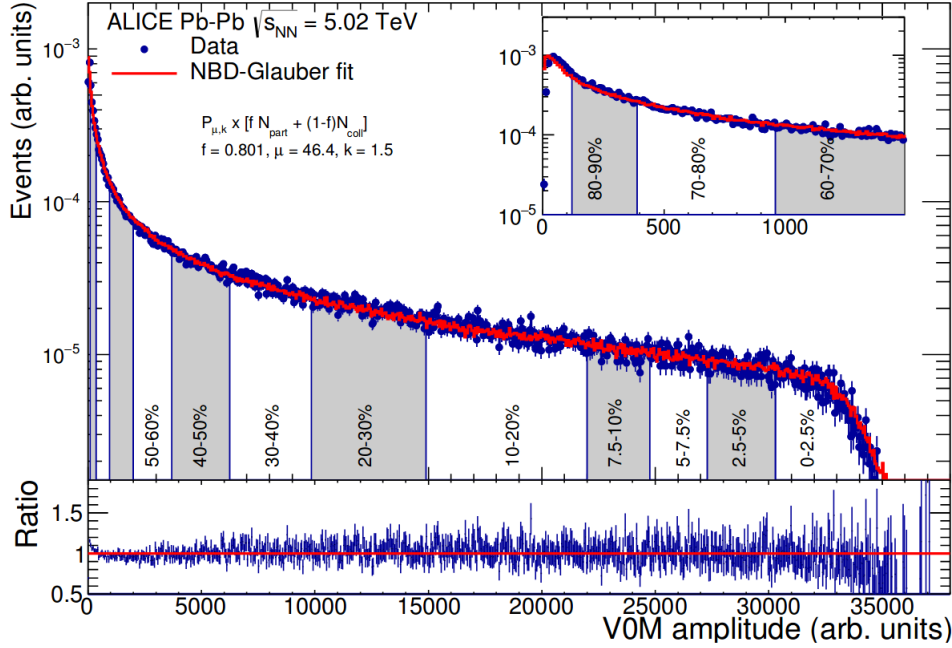


Figure 3.3.: The distribution of the V0 signal amplitude (blue), the model fit for charged particle production (red) and the corresponding centrality classes [28].

Apart from the centrality, individual HIC events are geometrically characterised by their reaction plane. The reaction plane is spanned by the vector connecting the centers of the colliding nuclei and the beam axis. In the collision an almond shaped fireball is produced and starts to expand. The pressure gradient in the reaction plane is larger than in the perpendicular direction. Thus, the expansion adds momentum to the particles' momentum vectors anisotropically, i.e. the component added in the reaction plane is on average larger than the out of reaction plane component. Consequently, a larger number of tracks is observed in the reaction plane than in the perpendicular direction (see Fig. 3.4). This effect is commonly called elliptic flow.

This asymmetry in the multiplicity distribution can be measured and used to determine the reaction plane. The corresponding observable is called event plane. It is constructed for each event using the sum of the unit vectors of the measured

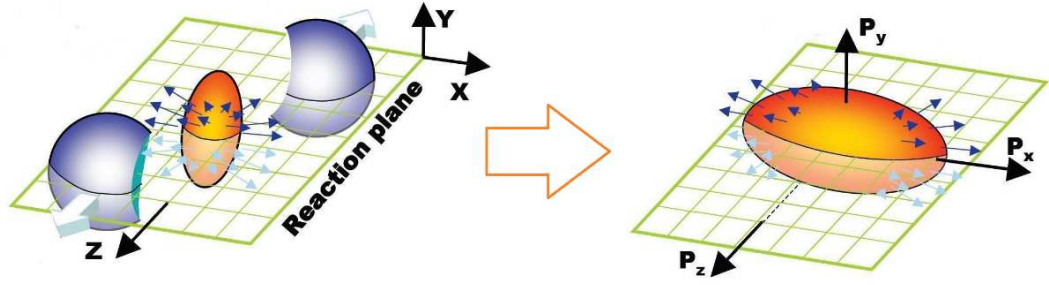


Figure 3.4.: Left: Depiction of the reaction plane in a HIC. Right: During the expansion of the fireball its spatial asymmetry is turned into an asymmetry in momentum space ($P_{x,y}$) of the produced particles [29].

particle momenta in the transverse plane [30]:

$$\vec{Q} = (Q_x, Q_y) = \sum_i (\cos(2\varphi_i), \sin(2\varphi_i)), \quad (3.3)$$

where φ_i is the azimuthal angle of the i -th particle. From this vector the azimuthal angle of the event plane (Ψ) is estimated via [30]:

$$\Psi = \frac{1}{2} \arctan2(Q_y, Q_x). \quad (3.4)$$

In this thesis the event plane is determined using tracks in the ALICE Time Projection Chamber (TPC, see Chapter 4 and Section 5.10) and the event plane extraction method described in [31]. The resolution of the event plane is typically estimated by evaluating correlations of event planes obtained with different detectors. For instance, the resolution of detector A can be estimated by comparing its event plane (Ψ^A) with the ones of detector B and C ($\Psi^{B/C}$). The corresponding resolution of detector A is typically defined by [30]:

$$R_2^A = \sqrt{\frac{\langle \cos(2(\Psi^A - \Psi^C)) \rangle \langle \cos(2(\Psi^A - \Psi^B)) \rangle}{\langle \cos(2(\Psi^B - \Psi^C)) \rangle}}. \quad (3.5)$$

For ideal detectors all event planes would be identical and the R_2^A would be unity. The actually achievable resolution is, however, limited due to, e.g. the finite number of tracks and non-flow particle correlations, like jets and resonance decays [31]. The resolution obtained with the TPC can be estimated by comparing the TPC and V0A and V0C (A and C indicate in which direction along the beam the detector is located) event planes. Figure 3.5 shows this resolution in dependence

of the centrality for Pb–Pb collisions at $\sqrt{s_{NN}} = 5.02$ TeV [32]. Here R_2^{TPC} is evaluated according to Eq. (3.5), with detector A being the TPC and detectors B and C being the V0A and V0C detectors (red crosses). In very central collisions the initial fireball becomes increasingly circular and therefore elliptic flow is small in these collisions. This causes a low event plane resolution in central events. In very peripheral collisions the resolution becomes worse as the track multiplicity is low.

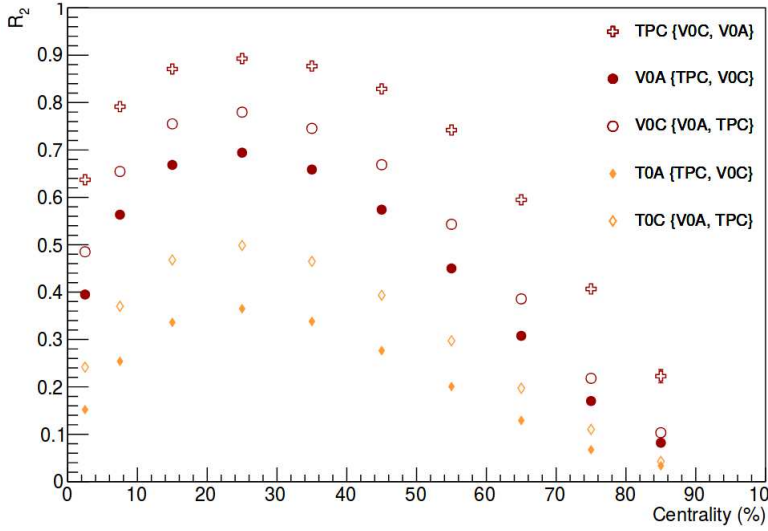


Figure 3.5.: Event plane resolution for the TPC and the V0 and T0 detectors in Pb–Pb collisions at $\sqrt{s_{NN}} = 5.02$ TeV [32]. A and C indicate the two different detector positions of the T0 and V0 detectors along the beam directions (see Fig. 4.1).

3.2. Dileptons

This section introduces the research topics related to dileptons with an emphasis on dielectrons, which are the probe used in this thesis to study HICs. The associated phenomenology and related results of dielectron or dimuon analyses are discussed.

The ALICE detector (Chapter 4) can identify and track electrons with its central-barrel detectors while muon track reconstruction is restricted to the forward region. A larger acceptance is available for electrons. On the other hand dielectron analyses have to deal with a larger amount of combinatorial background (see Sec-

tion 5.3). Due to these practical differences dielectron and dimuon analyses are typically carried out separately in ALICE.

Dileptons have additional degrees of freedom compared to single particle probes, which are the invariant mass m_{ee} and transverse pair momentum $p_{T,ee}$. The present work focusses on $p_{T,ee}$ spectra of dielectrons in the invariant mass range $m_{ee} \leq m_{J/\psi}$. As shown in Fig. 3.6, the relative contribution of different dielectron sources varies with their invariant mass. Different mass regions are therefore discussed separately in the following.

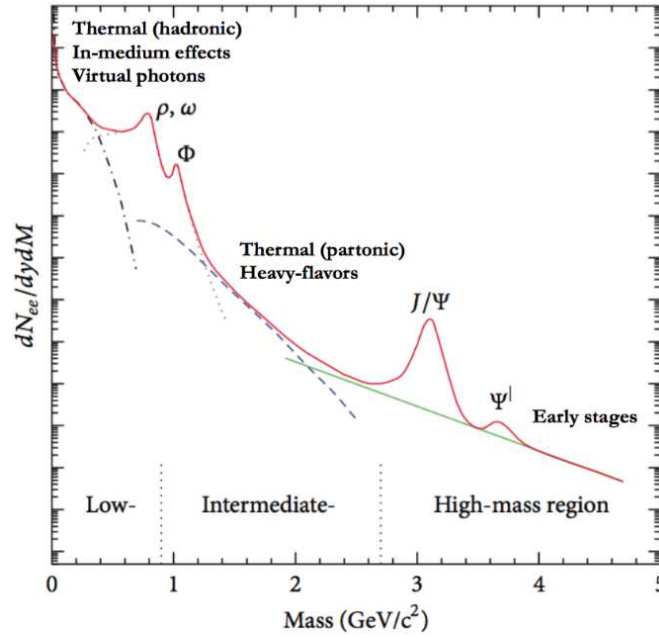


Figure 3.6.: Schematic invariant mass spectrum of dielectrons [33]. Single letters indicate the resonance peaks associated to the dielectron decays of the corresponding vector mesons.

3.2.1. Low-mass dielectrons

The low-mass region ($m_{ee} \leq m_{\phi}$) is dominated by decays of light-flavour mesons, i.e. mesons containing only up, down or strange quarks, in the e^+e^- channel (see Fig. 5.13 and Fig. 5.14). In this region dilepton spectroscopy of light vector mesons is of particular interest since it may reveal indications of the restoration of chiral symmetry in the QGP. The effect of chiral symmetry breaking is most pronounced in the light-quark sector, where it generates the dominant fraction of mass com-

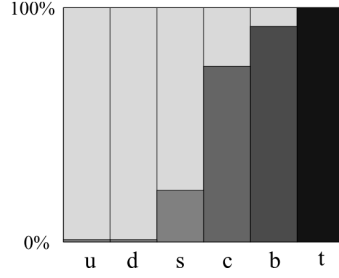


Figure 3.7.: Fraction of the mass generated by chiral symmetry breaking (light grey) and via the Higgs field (dark grey) for effective quark masses. The light quarks of flavour up (u), down (d) and strange (s) receive their mass predominantly through chiral symmetry breaking [12].

pared to the Higgs field (see Fig. 3.7). In addition, light vector mesons like the ρ^0 meson have a life time ($\tau_\rho \approx 1.3 \text{ fm}/c$) short enough to decay within the QGP and thus may reveal effects of the chiral phase transition. Decay channels into dileptons are ideal for the study of in-medium properties since leptons are not subject to the strong interactions and thus are almost unaffected by other collision products. Therefore, the mass of their mother particles in the medium can be inferred, which may reveal signs of chiral symmetry restoration.

The connection between spectrum of the ρ^0 meson and chiral symmetry restoration is rather involved and based on model assumptions. As pointed out in Section 2.2, the restoration of chiral symmetry implies that the ρ^0 and a_1 mesons obtain the same mass. The prediction of a dropping mass of the ρ^0 resonance, known as Brown-Rho scaling [34], was refuted by results from experiments at the SPS. This was first found in dielectron data of Pb–Au collisions at $\sqrt{s_{NN}} \approx 17 \text{ GeV}$ by CERES which shows a broad enhancement with respect to expected hadronic dielectron sources in the mass region below $m_\rho \approx 770 \text{ GeV}/c^2$ [35]. The NA60 collaboration at the SPS confirmed this finding in a dimuon analysis of In–In collisions at $\sqrt{s_{NN}} \approx 17 \text{ GeV}$ with higher precision [36]. For this analysis the expectations from hadronic dimuon sources except the ρ^0 are subtracted from the measured spectrum. The resulting excess spectrum in Fig. 3.8 shows that the data and the Brown-Rho prediction (green line) are in incompatible. The data, however, exhibit a broadening of the ρ^0 resonance which is in good agreement with a hadronic many-body model of the in-medium vector mesons spectral function (blue line in Fig. 3.8) [37]. In addition, the data are found to be incompatible with the assumption of no modification of the line shape, which is represented in Fig. 3.8 by the vacuum ρ^0 and the cocktail ρ^0 . The cocktail represents the expected dielectron yield from known hadronic sources. In contrast to the vacuum ρ^0 , the cocktail ρ^0 accounts for the expected production of additional ρ^0 mesons by the medium.

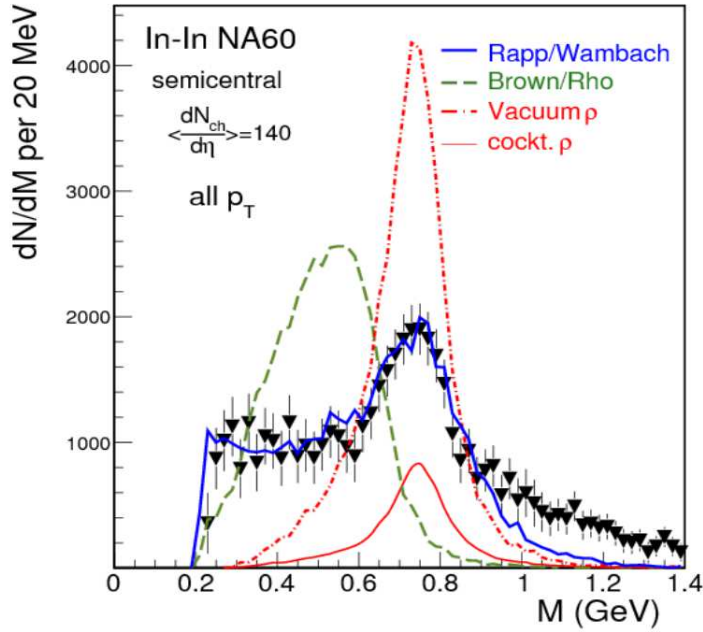


Figure 3.8.: Comparison of the dimuon excess spectrum by NA60 to theoretical predictions [38].

Experimental data from the RHIC consolidate the conclusions drawn from the SPS analyses [39–41]. Figure 3.9 (left) shows the dielectron spectrum measured by STAR at RHIC in comparison to predictions for the ρ^0 based on hadronic many-body approach (Rapp) and a microscopic transport model called Parton-Hadron String Dynamics (PHSD). Both predictions are in line with the data.

Due to limited statistics analyses at the LHC could so-far not achieve sensitivity to effects of in-medium modification of the ρ^0 meson (Fig. 3.9, right).

More recent theoretical results establish a connection between the observed ρ^0 broadening and the restoration of chiral symmetry [43]. Apart from the broadening these models assert that the peak of the ρ^0 resonance remains approximately constant while the mass of the a_1 drops. Deducing chiral symmetry unambiguously from the observation of a modified ρ^0 width alone appears difficult at this moment and may require extremely high experimental precision to allow discrimination of other effects like collisional broadening [44]. To this end broadening and chiral symmetry restoration are found to be compatible and further theoretical connections are under investigation.

Besides light-flavour meson decays, dielectrons in the low-mass region are produced by thermal radiation from the QGP and the hadron gas. Corresponding microscopic processes are for example quark anti-quark annihilation in the QGP phase and $\pi^+\pi^-$ annihilation in the hadron gas phase. The invariant mass spectrum of

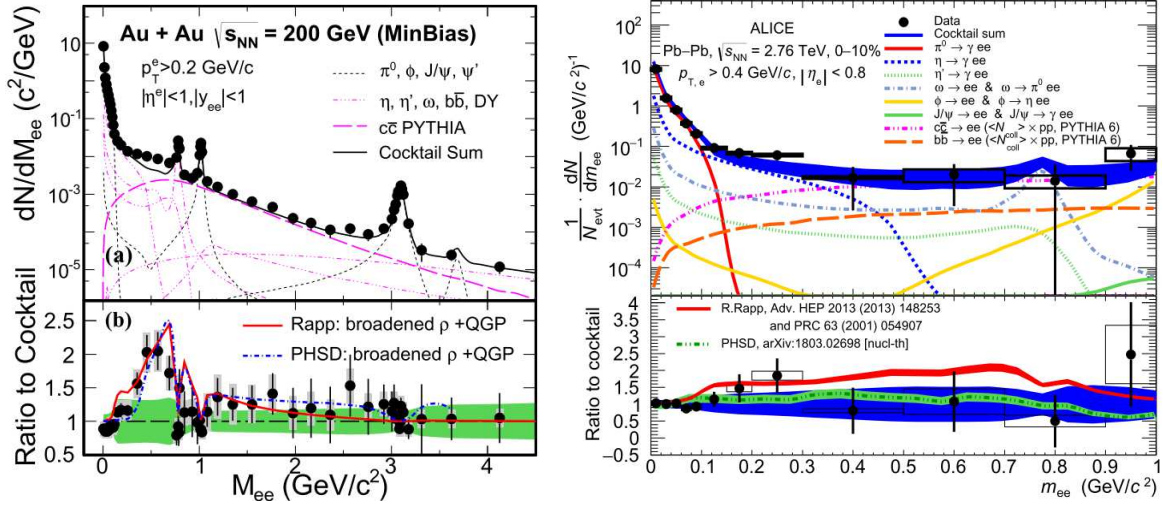


Figure 3.9.: Comparison of the measured dielectron mass spectrum to two predictions for thermal radiation and in-medium modifications by STAR [40] (left) and ALICE [42] (right). The spectra are normalised to the number of events N_{evt} .

the thermal dielectrons is schematically related to the temperature of the emitting medium via [3]:

$$\frac{dN_{ee}}{dm_{ee}} \propto e^{-m_{ee}/T}. \quad (3.6)$$

The emission of thermal dileptons takes place throughout the evolution of the expanding fireball. Due to the varying parameters, like number of degrees of freedom (transition from partons to hadrons) and temperature, the precise relation between the thermal spectrum and the temperature relies on models of the transport properties and the equation of state of the fireball.

Thermal dielectron analyses at low masses face the problem of an overwhelming background from the neutral pion Dalitz decay $\pi^0 \rightarrow \gamma e^+ e^-$. In general, dielectron production from photon sources becomes more suppressed with rising mass (i.e. with rising virtuality of the virtual photon)¹. The suppression, however, is less severe for dielectrons from so-called quasi real photons, i.e. virtual photons for which $p_{T,ee} \gg m_{ee}$. Background from π^0 Dalitz decay dielectrons can be eliminated by restricting an analysis to masses between $m_\pi = 135$ MeV/ c^2 and the broad ρ^0 resonance, centered at $m_\rho \approx 770$ MeV/ c^2 . In addition, choosing a $p_{T,ee}$ range such that the associated photons are quasi real enhances the signal-to-background ra-

¹The ratio between the number of real and virtual photons as a function of virtual photon mass is described by the Kroll-Wada equation [2, 45].

tio with respect to other hadronic dielectron sources and combinatorial dielectron background (see Section 5.5).

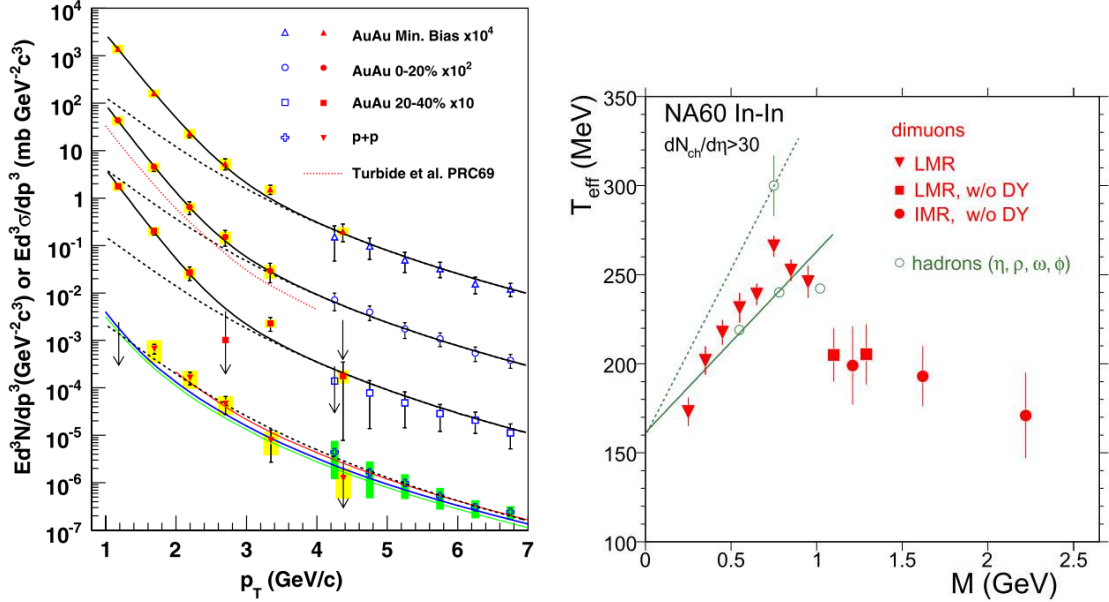


Figure 3.10.: Left: Transverse momentum spectra of excess dielectrons by PHENIX. The lines around the pp data show pQCD calculations. Filled symbols represent data points obtained from a dielectron analysis, while open symbols indicate data points obtained in a photon analysis. Dashed black lines show a power-law fit to the pp data, which is scaled to corresponding collision system and centrality. The solid lines show the result of a fit using the scaled power-law function and an exponential function [46]. Right: Effective temperatures, which are extracted from different $p_{T,ee}$ integrated dimuon m_T spectra, as a function of invariant dimuon mass by NA60 (red) [36]. The values obtained from hadron analyses are shown in green.

Using this approach the PHENIX collaboration at RHIC found an excess of dielectrons in Au–Au collisions at $\sqrt{s_{NN}} = 200$ GeV with respect to the hadronic cocktail in the mass range of $0.1–0.3$ GeV/ c^2 and the p_T^2 interval $1–5$ GeV/ c [46]. This result was obtained using a two-component fit of the $p_{T,ee}$ excess spectrum (Fig. 3.10, left). The first component is a power-law function which describes

²To be consistent with notation used by PHENIX p_T is used instead of $p_{T,ee}$ for the pair-transverse momentum in the context of this result.

proton-proton (pp) collision data (dashed black line for pp). Perturbative QCD calculations (green, red and blue curves) match the pp data and thus allow the interpretation of the power-law function as a template for spectra of hadronic contributions. These templates are scaled up to match expectations for Au–Au collisions (dashed black lines for Au–Au). At low p_T the Au–Au excess spectra over-shoot the power-law templates. In this range the Au–Au data is compatible with an exponential function $\propto \exp(-p_T/T)$. Assuming a thermal origin of the dielectrons corresponding to this exponential component would suggest to interpret the fit parameter $T = 221 \pm 19^{\text{stat}} \pm 19^{\text{sys}}$ MeV as an effective temperature of the emitting medium. In the context of models of the evolution of the fireball, this result is compatible with an initial temperature of 300 – 600 MeV [46].

So far corresponding analyses of Pb–Pb data at the LHC could not achieve high enough precision to measure thermal dielectrons [42].

Another result related to thermal radiation in the low-mass region was produced by NA60 at the SPS [36]. Here the aforementioned dimuon excess spectrum in the low-mass region is used to extract the inverse slope parameter T_{EFF} of the $p_{T,\mu\mu}$ integrated transverse mass spectrum ($m_{T,\mu\mu} = \sqrt{p_{T,\mu\mu}^2 + m_{\mu\mu}^2}$) as shown in Fig. 3.10 (right). The rise of T_{EFF} in the low-mass region is interpreted as an effect of the radial expansion of the fireball. Due to the strong coupling of pions to the ρ^0 ($\pi\pi \rightarrow \rho^0 \rightarrow \mu^+\mu^-$) the dimuons exhibit a flow effect that is comparable to hadrons (green). At higher masses T_{EFF} is constant at a lower value, which is regarded as an indication of dimuon emission from the partonic stage ($q\bar{q} \rightarrow \mu^+\mu^-$) in which flow effects are less pronounced.

3.2.2. Intermediate-mass dielectrons

In contrast to the low-mass region the intermediate mass region ($m_\phi \leq m_{ee} \leq m_{J/\psi}$, see Fig. 3.6) of the dielectron spectrum exhibits no resonances and thus less background with respect to thermal sources. On the other hand, the amount of measured dielectrons is in general lower in this region, resulting in larger statistical uncertainties.

Apart from thermal production, correlated decays of heavy-flavour hadrons (charm and beauty) are the dominant dielectron source. In these processes heavy-flavour quark and anti-quark pairs ($c\bar{c}$ and $b\bar{b}$) are produced in inelastic hard scattering of partons or thermally in the medium. Afterwards the individual (anti-) quarks hadronise into a meson or a baryon. Subsequently the hadrons originating from the initial quark and anti-quark may decay semi-leptonically and produce a dielectron. Due to their common origin, the two legs of this dielectron are correlated.

In the intermediate mass range thermal emission is primarily emitted in the par-

tonic phase [2, 36]. As shown in Fig. 3.11, dielectrons from heavy-flavour hadron decays ($c\bar{c} \rightarrow e^+e^-$ and $b\bar{b} \rightarrow e^+e^-$) are expected to be produced in comparable numbers to thermal dielectrons from partonic sources ($q\bar{q} + q(\bar{q})g$). Therefore, the heavy-flavour contribution needs to be subtracted to isolate thermally produced dielectrons. Consequently, the precision to which the heavy-flavour yield is known plays a crucial role in such analyses.

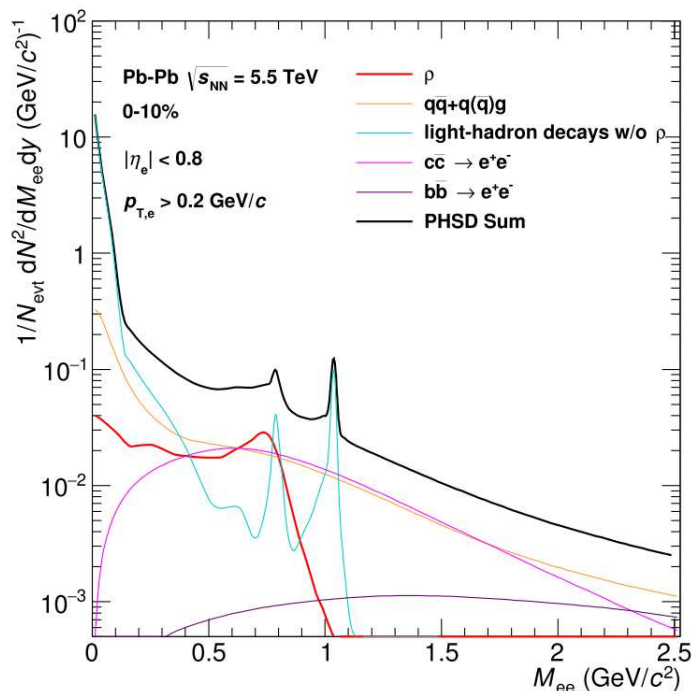


Figure 3.11.: Prediction for the dielectron spectrum including QGP radiation (orange) and hadronic sources (see legend) with the PHSD model [47].

Besides their importance for a measurement of thermal radiation, dielectrons from heavy-flavour hadron decays are essential in the analysis of photo-produced dielectrons at low- $p_{T,ee}$ (see Section 5.6).

3.3. Electromagnetic interactions in heavy-ion collisions

Apart from the study of strong interaction phenomena, HICs offer the opportunity to access extremely strong electromagnetic fields in the laboratory. The maximum

electric field strength E_{\max} in relativistic Pb–Pb (nuclear charge $Z = 82$) collisions at the LHC (Lorentz factor $\gamma \approx 3000$) at an impact parameter $b \approx 15$ fm (see Section 3.1) can be estimated to be on the order of [48]:

$$E_{\max} \approx \frac{Ze\gamma}{b^2} = 1.5 \cdot 10^{18} \text{ V/cm}, \quad (3.7)$$

where e is the electric unit charge.

As argued in [48] this field strength is more than two orders of magnitude larger than the critical field strength for Schwinger production of e^+e^- pairs, i.e. dielectron production from a strong and constant electric field. Setting aside the time variation of electromagnetic fields of colliding nuclei, this suggests that dielectron production from electromagnetic interactions is possible in HICs.

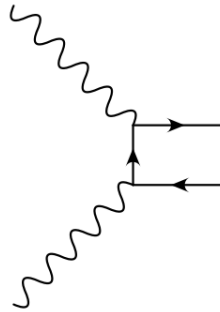


Figure 3.12.: The leading order QED Feynman diagram for dilepton photoproduction. Time proceeds from the left to the right hand side of the diagram. Two photons (waved lines) exchange a virtual electron (line with arrow) and go into a dielectron [49].

The production cross section of a e^+e^- pair from two real photons (see Fig. 3.12) was first obtained by Breit and Wheeler in the 1930s [50]. Today this process is commonly referred to as the Breit-Wheeler process. Due to crossing symmetry in quantum field theory, the matrix elements for this process are the same as the ones for e^+e^- annihilation ($e^+e^- \rightarrow \gamma\gamma$) [51]. The different cross sections of annihilation and the Breit-Wheeler process come from the fact that only in the latter the final state particles are identical and not massless. While $e^+e^- \rightarrow \gamma\gamma$ annihilation was soon observed after the discovery of the positron, the Breit-Wheeler process has eluded observation to this day. Experimental attempts in the laboratory usually rely on high-energy lasers. The extreme conditions around black holes may allow observational studies to identify the Breit-Wheeler process in astrophysics [51].

In 1934 E.J. Williams and C. von Weizsäcker found independently that the electromagnetic field of relativistic charges can be regarded as a flux of quasi-real photons [52, 53]. The method of treating an electromagnetic field as a photon flux is

called the Equivalent Photon Approximation (EPA). In this picture the interaction of the electromagnetic fields of colliding nuclei involves collisions of the associated photon fluxes. Thus, HICs could involve e^+e^- production via the Breit-Wheeler process with quasi-real photons. This process is also called photon-photon fusion. Another dielectron production mechanism is the photo-nuclear process. Here a photon associated to the electromagnetic field of one nucleus interacts with the gluon field of the other nucleus to produce a vector meson which may decay into a dielectron. In this process the gluon field can be treated as a quantum state with the same quantum numbers as the vacuum, which is typically called Pomeron [1]. According to the rules of angular momentum addition in quantum mechanics the photon (spin 1) and the Pomeron (spin 0) can only produce another vector particle (spin 1). This can be a vector meson which may decay into a dielectron.

If the involved photons have a sufficiently large wavelength in the transverse direction, i.e. low transverse momentum (p_T), they probe the whole nucleus and the resulting interactions are called coherent. Using the uncertainty principle the coherence requirement can be used to estimate the corresponding values for Pb ions at the LHC to be $p_T \lesssim \hbar/R_A \approx 28 \text{ MeV}/c$ [54]. In the direction along the beam the same argument can be used when considering the Lorentz contraction ($\gamma \approx 2676$) of the nucleus. For Pb ions at the LHC a maximum longitudinal photon momentum of $p_L \lesssim \gamma\hbar/R_A \approx 75 \text{ GeV}/c$ is obtained. Thus, in coherent photon-photon collisions the maximum center-of-mass energy is $\sqrt{s_{\gamma\gamma}} \approx 150 \text{ GeV}/c^2$ [54]. The associated photon densities rise quadratically with the charge number Z of the nucleus (see Eq. (3.9)). Since the photon p_T is low, the nuclei typically do not break up in such interactions [55]. Photon-fusion involves two photons and thus the corresponding cross section scales with Z^4 for symmetric HICs. Therefore, the cross section is increased by a factor $\sim 4.5 \cdot 10^7$ when colliding Pb ions ($Z = 82$) instead of protons ($Z = 1$) [56]. The photo-nuclear process involves only one photon and consequently scales with Z^2 [57].

HICs without hadronic interactions, so-called Ultra Peripheral Collisions (UPCs), allow the observation of dielectron production in electromagnetic interactions without background from other sources. The condition for a UPC is approximately equivalent to demanding that the impact parameter b is larger than the sum of the radii of the two colliding nuclei (see Fig. 3.13). Models of coherent J/ψ and dielectron production in UPCs successfully describe corresponding measurements by ALICE [58], ATLAS [56], CMS [55], and STAR [59].

While photo-production in UPCs seems to be well understood, the situation in hadronic collisions, i.e. collisions with overlapping nuclei, is quite different. As outlined in the following sections, coherent photon interactions in these collisions pose conceptual questions about the applicability of the models used for UPCs. In addition, results of dilepton photo-production in hadronic collisions are presently

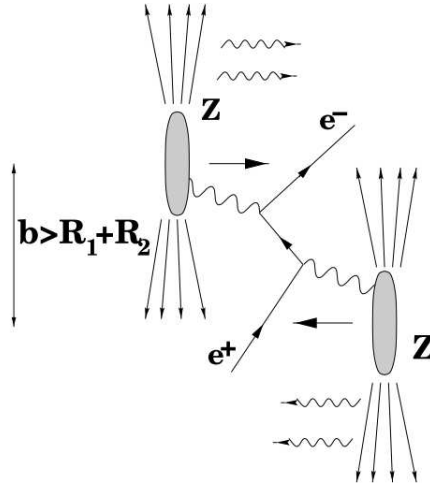


Figure 3.13.: Dielectron photo-production in an Ultra Peripheral Collision [48].

not completely compatible with calculations. The next two sections provide an overview of experimental results and theory approaches which are relevant in this context.

3.3.1. Previous experimental results

Before discussing coherent dilepton photo-production, two J/ψ analyses are briefly summarised, because they are interpreted as indications for a similar process, which is the photo-nuclear process in hadronic collisions.

The ALICE collaboration reported the measurement of an excess in the J/ψ yield in peripheral Pb–Pb collisions at $\sqrt{s_{NN}} = 2.76$ TeV [60]. The analysis uses the dimuon decay channel ($m_{\mu\mu}$: 2.8 – 3.4 GeV/ c^2) and muon reconstruction in the muon detectors (see Chapter 4). A comparison of the data to expectations based on the measured J/ψ production cross section in pp collisions ($\sigma_{J/\psi}^{pp}$) is carried out. For this purpose $\sigma_{J/\psi}^{pp}$ is multiplied by the number of events N_{events} , the average nuclear overlap function $\langle T_{AA} \rangle^3$, the acceptance A , the reconstruction efficiency ϵ , and the branching ratio of J/ψ into dimuons ($\text{BR}_{J/\psi \rightarrow \mu^+ \mu^-}$). The ratio of the measured J/ψ yield ($N_{J/\psi}^{AA}$) and the corresponding expectation is called the nuclear

³This factor accounts for the increased number of nucleon-nucleon interactions in Pb–Pb collisions with respect to pp collisions. It is related to N_{Coll} (see Section 3.1) and the inelastic nucleon–nucleon cross section $\sigma_{NN}^{\text{inel}}$ via $\langle T_{AA} \rangle = N_{\text{Coll}} / \sigma_{NN}^{\text{inel}}$.

modification factor R_{AA} :

$$R_{AA} = \frac{N_{J/\psi}^{AA}}{\text{BR}_{J/\psi \rightarrow \mu^+ \mu^-} \cdot A \cdot \epsilon \cdot \langle T_{AA} \rangle \cdot N_{\text{events}} \cdot \sigma_{J/\psi}^{\text{pp}}}. \quad (3.8)$$

This quantity is expected to be unity if J/ψ production is not changed with respect to pp collisions. It is determined for different bins of the pair-transverse momentum $p_{T,\mu\mu}$ and centrality.

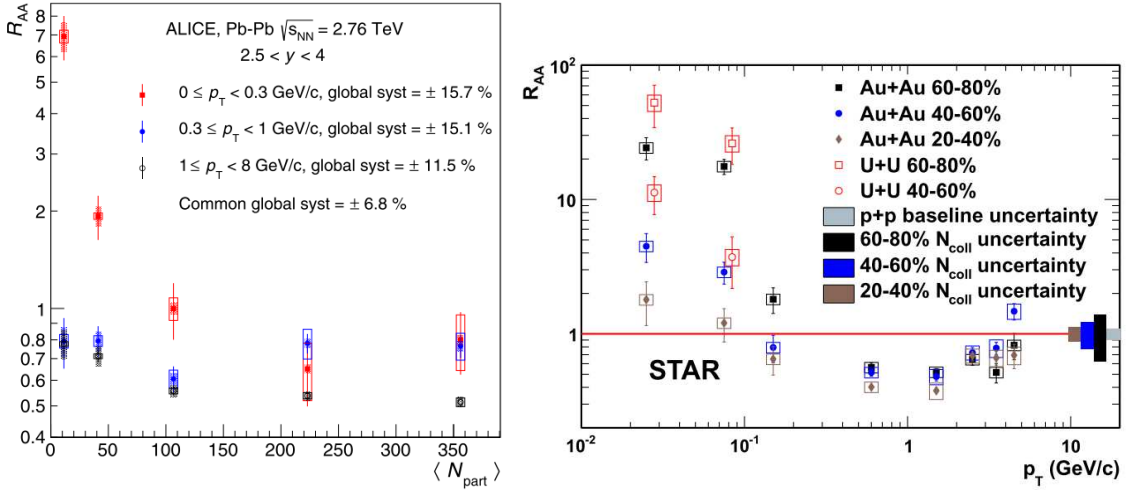


Figure 3.14.: Left: Dependence of R_{AA} on centrality and pair-transverse di-muon momentum p_T in Pb–Pb collisions at $\sqrt{s_{NN}}=2.76$ TeV [60]. Right: R_{AA} in dependence of the pair-transverse dielectron momentum p_T and centrality in Au–Au and U–U collisions [61].

Figure 3.14 (left) shows that an excess ($R_{AA} > 1$) is measured at low $p_{T,\mu\mu}$ (p_T in the figure) which increases with decreasing $\langle N_{\text{part}} \rangle$, the average number of participant nucleons for a centrality class (see Fig. 3.1). The first two $\langle N_{\text{part}} \rangle$ bins correspond to the centrality ranges 70–90% and 50–70%. According to the definition of R_{AA} , this is an indication of additional J/ψ production to the expectation from nucleon-nucleon interactions like in pp collisions. In the absence of dedicated calculations ALICE estimates the expected yield by coherent photo-nuclear production based on UPC models. This leads to the conclusion that this process is a likely candidate to explain the excess. Subsequent theoretical studies confirm this conclusion, as will be discussed in Section 3.3.2 [62, 63]. Transport models [64, 65], which were successfully used to describe previous J/ψ measurements [66–68], cannot provide a suitable explanation.

The STAR collaboration measured the J/ψ yield in Au–Au collisions at $\sqrt{s_{NN}} =$

200 GeV and U–U collisions at $\sqrt{s_{\text{NN}}} = 193$ GeV [61]. In this analysis the dielectron decay channel is used (m_{ee} : 2.9 – 3.2 GeV/ c^2). Also here the nuclear modification factor R_{AA} is determined. Extrapolations of global experimental data to $\sqrt{s_{\text{NN}}} = 200$ GeV serve as a baseline, since there were no measurements available at this collision energy. Figure 3.14 (right) shows R_{AA} in Au–Au and U–U collisions for various bins of the pair-transverse momentum (p_{T}) and centrality. For p_{T} : 0.0 – 0.2 GeV/ c the data exhibit an excess. As in the ALICE measurement, here the excess also becomes more pronounced for more peripheral collisions. Coherent photo-production is found to provide a suitable description of the data (details in Section 3.3.2). The suppression ($R_{\text{AA}} < 1$) observed at $p_{\text{T}} > 0.2$ GeV/ c can be attributed to known cold and hot medium effects [65, 69].

The ATLAS collaboration observed dimuon production via photon-fusion ($\gamma\gamma \rightarrow \mu^+\mu^-$) in Pb–Pb collisions at $\sqrt{s_{\text{NN}}} = 5.02$ TeV [70]. This analysis uses muon tracks with $p_{\text{T}} > 4.0$ GeV/ c and a dimuon mass range of 4 – 45 GeV/ c^2 . Dimuons are analysed in terms of pair acoplanarity α and asymmetry A , which are defined as:

$$\alpha = 1 - \frac{\varphi^+ - \varphi^-}{\pi},$$

$$A = \frac{|p_{\text{T}}^+ - p_{\text{T}}^-|}{|p_{\text{T}}^+ + p_{\text{T}}^-|},$$

where φ^\pm are the azimuthal angles of the μ^\pm tracks and p_{T}^\pm are the corresponding transverse track momenta. Due to the low total p_{T} of the $\gamma\gamma$ system both variables, α and A , are expected to peak at low values for photon-fusion. The main background for dimuons from photon-fusion is expected to stem from correlated decays of heavy-flavour hadrons. It is estimated from the data using background isolation cuts in α and A and a template fit of the distribution of the transverse dimuon impact parameter with respect to the collision vertex. For the template fits the photon-fusion component is obtained from STARlight [71] MC simulations. Figure 3.15 shows the background-subtracted distributions of α and A for different centrality classes (the data of the centrality class $> 80\%$ is shown in each panel in red). STARlight MC simulations of photon-fusion (blue shaded areas) are compared to the data (black). The data are compatible with zero at high values of α and A . This indicates that background sources were adequately subtracted. In terms of acoplanarity α the data is accurately described in the centrality class $> 80\%$, which is dominated by UPCs. Going to more central collisions the data exhibit an increasing broadening. The ATLAS collaboration states that qualitatively this is expected if the broadening is due to interactions of the muons with the QGP. The absence of any broadening in A (lower row in Fig. 3.15) is explained by the limited detector resolution.

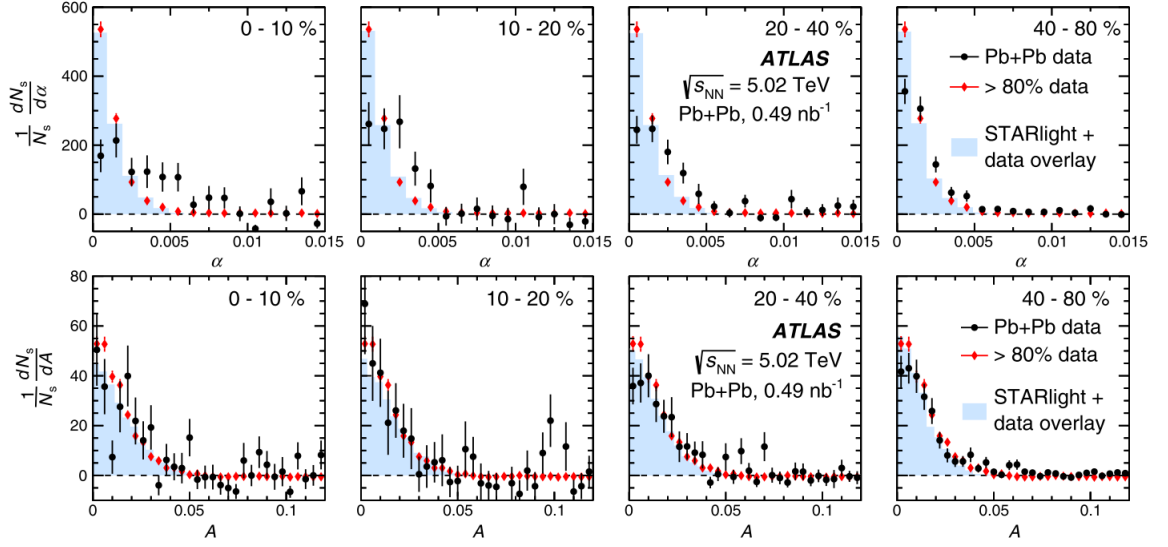


Figure 3.15.: Background-subtracted acoplanarity (α) and asymmetry (A) spectra of dimuons in different centrality classes measured in Pb–Pb collisions at $\sqrt{s_{\text{NN}}} = 5.02$ TeV by ATLAS [70].

Further evidence for dilepton production by coherent photon-fusion in HICs with hadronic overlap was reported by STAR [72]. This analysis probes a lower track transverse momentum and invariant mass regime than the aforementioned analysis by ATLAS. Electron tracks with $p_{\text{T}} > 0.2$ GeV/ c are used to analyse dielectron $p_{\text{T,ee}}$ spectra in the mass range of $0.4 - 2.6$ GeV/ c^2 . As discussed in Section 3.2.1 this kinematic range contains numerous hadronic dielectron sources, which is sensitive to contributions from thermal radiation and may be affected by a modified line shape of the ρ^0 meson. Therefore, the data is in a first step compared to the baseline of the expected hadronic sources, called the cocktail. The cocktail does not contain the ρ^0 meson, since this contribution is typically studied separately to identify potential modifications.

The m_{ee} spectra at $p_{\text{T,ee}} < 0.15$ GeV/ c show an excess with respect to hadronic sources over the whole studied mass range (see Fig. 3.16, left). The data-to-cocktail ratio in the lower panel shows that the relative enhancement decreases up to m_{ϕ} (≈ 1 GeV/ c^2) and increases again for higher masses. A maximum is reached around $m_{\text{J}/\psi}$ (≈ 3.1 GeV/ c^2). This variation is regarded as an indication that different processes play a role in these two mass ranges. Therefore, this analysis is limited to masses up to 2.6 GeV/ c^2 . As in the other analyses discussed so far, the excess is rising for more peripheral collisions. The $p_{\text{T,ee}}$ spectrum (Fig. 3.16, right) shows that the excess over the cocktail is mostly contained in the range of $p_{\text{T,ee}}$: $0 - 0.15$ GeV/ c .

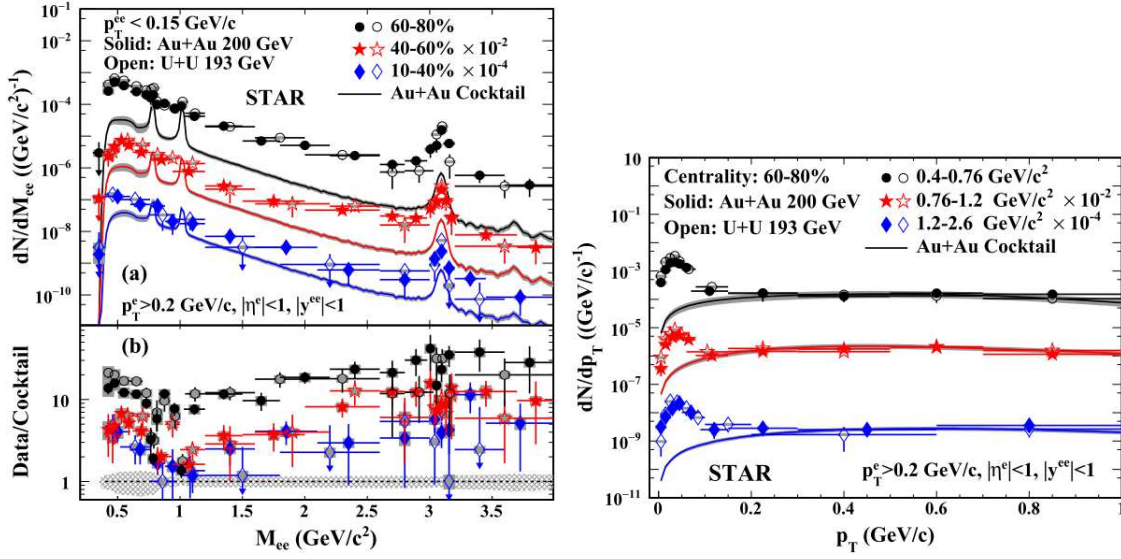


Figure 3.16.: Comparison of mass and transverse-momentum dielectron spectra to the cocktail in Au–Au and U–U collisions by STAR [72].

Subtracting the cocktail from the measured invariant mass spectrum allows the comparison of the excess spectrum to other dielectron sources (see Fig. 3.17, top). These sources include the thermal radiation from the QGP and a broadened ρ^0 resonance (Hot_Med), photon-fusion ($\gamma\gamma \rightarrow e^+e^-$) and photo-nuclear production of ρ^0 and ϕ mesons. Thermal radiation and the modified ρ^0 meson alone cannot account for the observed spectrum at $p_{T,ee} < 0.15$ GeV/c. Inclusion of the two calculations of photon-fusion, however, drastically improves the agreement with data. One of these calculations is based on the STARlight Monte Carlo generator [71], which successfully describes UPC data [73]. Potential short-comings of this model are that it uses a point-like nuclear form factor for the photon sources and ignores photo-production inside the nuclei. The other model by Zha et al. uses a more realistic form factor based on a Woods-Saxon distribution and accounts for photo-production inside the nuclei [74]. Both models provide a reasonable description of the data. Contributions from photo-nuclear vector meson production are found to be negligible.

As photon-fusion takes place primarily outside of the colliding nuclei the associated dielectron yield is expected to have a weaker dependence on centrality than the yield from hadronically-produced sources. Figure 3.17 (bottom) shows that the excess yield at $p_{T,ee} < 0.15$ GeV/c is in line with this expectation.

The shapes of the squared transverse momentum (p_T^2) excess spectra and of the aforementioned photon-fusion models for Au–Au collisions are compared in Fig. 3.18

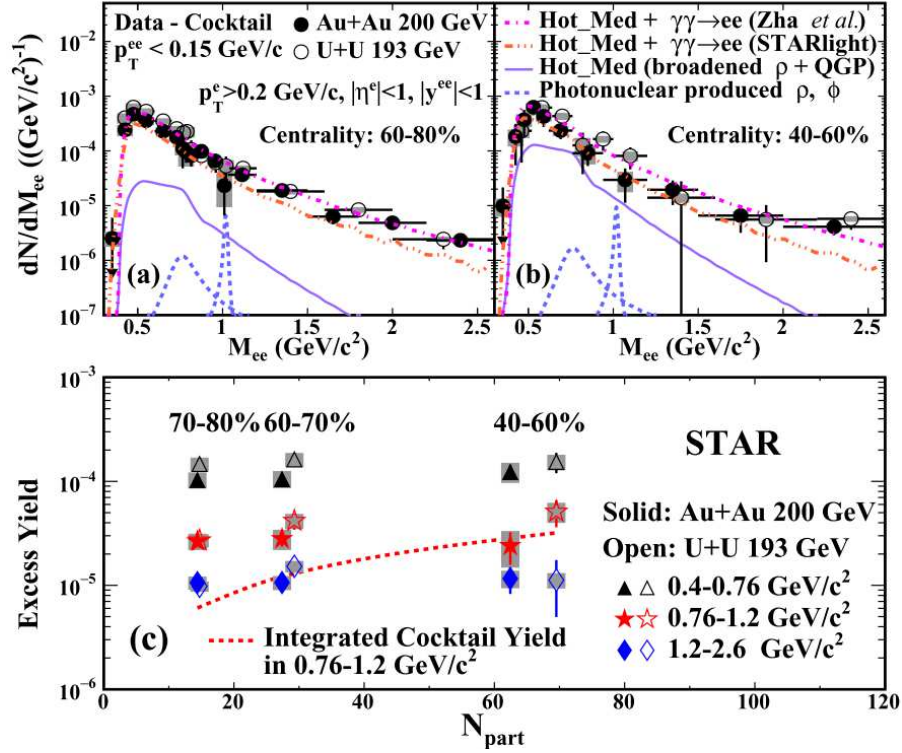


Figure 3.17.: Top row: Mass spectra at $p_{T,ee} < 0.15$ GeV/ c of the dielectron excess measured by STAR in Au–Au and U–U collisions. Bottom: Centrality dependence of the excess yield and the hadronic cocktail. Model calculations are performed for Au–Au collisions at $p_{T,ee} < 0.15$ GeV/ c [72].

(panels (a), (b) and (c)). The shape of the distributions is also expected to be sensitive to the extremely strong magnetic field produced by the spectators (see Fig. 3.1) in the collision. To investigate the associated effect on the spectrum, the model by Zha et al. is also shown with a magnetic field of 10^{14} T applied for the first 1 fm along the track paths (EM). Due to the collision geometry, this field is perpendicular to the beam line. So far the magnetic field in heavy-ion collisions has not been observed directly but would be of great interest due to its central role in the search for anomalous transport in the QGP [75] and magnetic monopoles (see Section 3.4.1).

For $p_T^2 < 0.001$ (GeV/ c)² the models by Zha et al. (with and without EM) overshoot the corresponding Au–Au data. In the higher p_T^2 region these models predict yields that describe the data fairly well. The STARlight calculations show a similar shape but result generally in a lower yield. The width of the spectra is quantified

by $\sqrt{\langle p_T^2 \rangle}$, which is calculated from fits of the data. Figure 3.18 (d) shows that the data exhibit larger broadening than the model by Zha et al. without a magnetic field. Invariant mass and p_T spectra are successfully described in UPC data using the theoretical approaches in this model. Therefore, the observed discrepancy in the broadening between data and model is interpreted as an indication for additional effects in hadronic collisions. One possibility investigated in [72] is that the strong magnetic field generated by the spectator nuclei is trapped inside the QGP (which would be absent in UPCs) and deflects the electron tracks. The associated broadening of the p_T^2 spectra describes the data much better (see blue line in Fig. 3.18 (d)). The STAR collaboration concludes that this may indicate the possible existence of a strong magnetic field in the QGP.

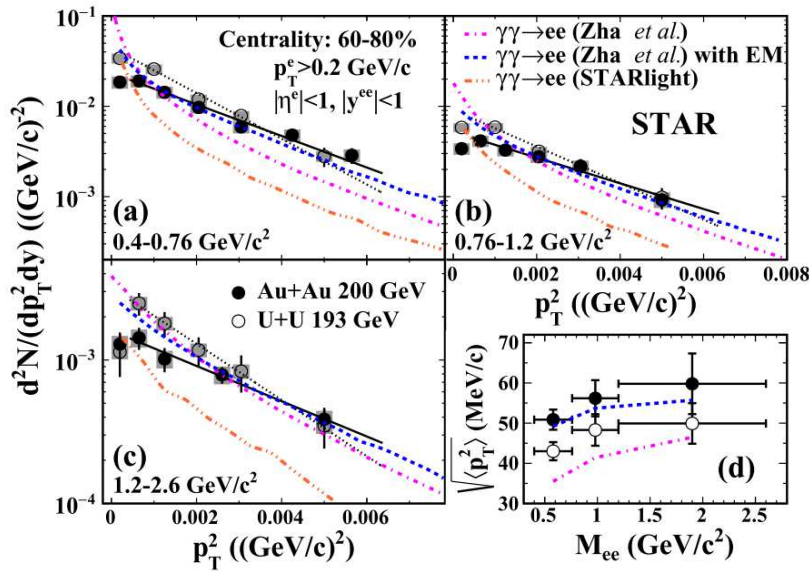


Figure 3.18.: Squared transverse-momentum excess spectra compared to models of photon-fusion. EM indicates that for this model both dielectron legs are assumed to traverse a strong magnetic field (see text for details). Model calculations are performed for Au–Au collisions [72].

In summary, the ALICE and STAR collaboration found an enhancement of J/ψ production in hadronic HICs. The centrality and p_T dependences of the excesses match the expectations for coherent photo-nuclear production. Similarly, dimuon and dielectron data by ATLAS and STAR in hadronic HICs are in line with photon-photon fusion models. However, both collaborations find that the dilepton data exhibit a broadening of the $p_{T,ee}$ spectra (for dielectrons) and acoplanarity (for dimuons) which does not match expectations based on UPC results and thus may indicate additional effects.

3.3.2. Theoretical approaches

This section discusses theoretical developments which are relevant in view of the experimental results outlined in Section 3.3.1. Emphasis is put on the photon-fusion process since this will be more relevant in the context of this thesis.

The correct theoretical approach to the coherence condition is a common question in the discussion of photo-production in hadronic collisions. Most approaches are based on the aforementioned EPA (see Section 3.3), which successfully describes data of UPCs. In this picture the electromagnetic fields of the colliding nuclei are treated as photon fluxes. In collisions with hadronic overlap the impact parameter (b) is smaller than twice the radius of the nuclei. This may necessitate a modification of the treatment of photo-production used in UPCs. For instance, it is argued in [63] that in the centers of the nuclei the photon-flux associated to the electromagnetic fields vanishes for symmetry reasons. In addition, the hadronic interaction may distort the coherence in the overlap region. It is not clear to which extent these effects modify the coherent interactions. In [63] four scenarios are studied which shall represent the limiting cases in terms of the coherence condition in photo-nuclear J/ψ production. The coherent photon emission process is assuming either only participation of the spectator (S) nucleons, i.e. the nucleons outside the overlap region, or of all nucleons (N) in the emitting nucleus. The same two cases are considered for the coherent scattering of the photon with the other nucleus. Combining the cases for emission and scattering leads to four different scenarios (N,N), (N,S), (S,S) and (S,N). The first letter denotes the coherence assumption in the photon emission and the second in the scattering. These cases lead to different centrality dependences of the photo-produced J/ψ yield. A comparison of these predictions to the data by ALICE and STAR shows that in both cases most data points fall in between the extreme cases of (N,N) and (S,S) (see Fig. 3.19).

In the following, theoretical results on dilepton photo-production in hadronic HICs are discussed. In UPCs the impact parameter b is large enough to justify a point-like approximation of the nucleus. In hadronic collisions b is comparable to the size of the nuclei which may invalidate this approximation. Since the equivalent photon spectrum depends on b and, through the electromagnetic nuclear form factor F_{EM} , on the charge distribution inside the nuclei, the $p_{T,ee}$ spectrum is expected to be sensitive to these geometrical aspects. The electromagnetic nuclear form factor accounts for the spatial electric charge distribution and the resulting interference of amplitudes associated to interactions involving the nucleus. The

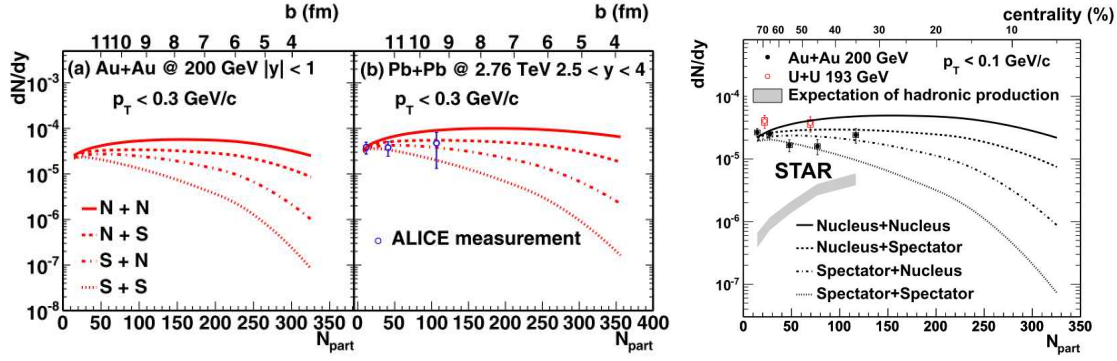


Figure 3.19.: Left: Predictions for various coherence assumptions in J/ψ production in HICs at RHIC (left) and LHC (right). For the latter the corresponding data by ALICE is compared to the model [63]. Right: The comparison of the predictions of J/ψ production for HICs to corresponding data by STAR [61].

equivalent photon spectrum $N(\omega, b)$ of a relativistic ion at impact parameter b takes the form [76]:

$$N(\omega, b) = \frac{Z^2 \alpha_{EM}}{\pi^2} \left| \int_0^\infty dq_T \frac{q_t^2 F_{EM}(q_T^2 + \frac{\omega^2}{\gamma^2})}{q_T^2 + \frac{\omega^2}{\gamma^2}} J_1(bq_T) \right|^2, \quad (3.9)$$

where ω denotes the photon energy, q_T the photon transverse momentum, Z the charge of the nucleus, α_{EM} the fine structure constant, γ the Lorentz factor of the nucleus in the lab rest frame and J_1 a modified Bessel function.

To account for a realistic nuclear charge distribution and photo-production inside the nuclei, the shape of the nuclei can no longer be assumed to be point-like as in [73]. In [74] a more realistic charge distribution is used to calculate the form-factor of the nuclei. The assumed charge distribution is a Woods-Saxon (WS) distribution ρ_A :

$$\rho_A(r) = \frac{\rho_0}{1 + \exp((r - R_{WS})/d)},$$

where r is the distance from the center of the nucleus, ρ_0 is a normalisation factor, R_{WS} is the nuclear radius and d is called the skin depth.

As shown in Fig. 3.17 both approaches, with point-like (STARlight, [73]) and WS (Zha et al., [74]) form factor, lead to reasonable descriptions of the low- $p_{T,ee}$ mass spectrum measured by STAR. However, both disagree with the shape of $p_{T,ee}$ spectrum (see Fig. 3.18).

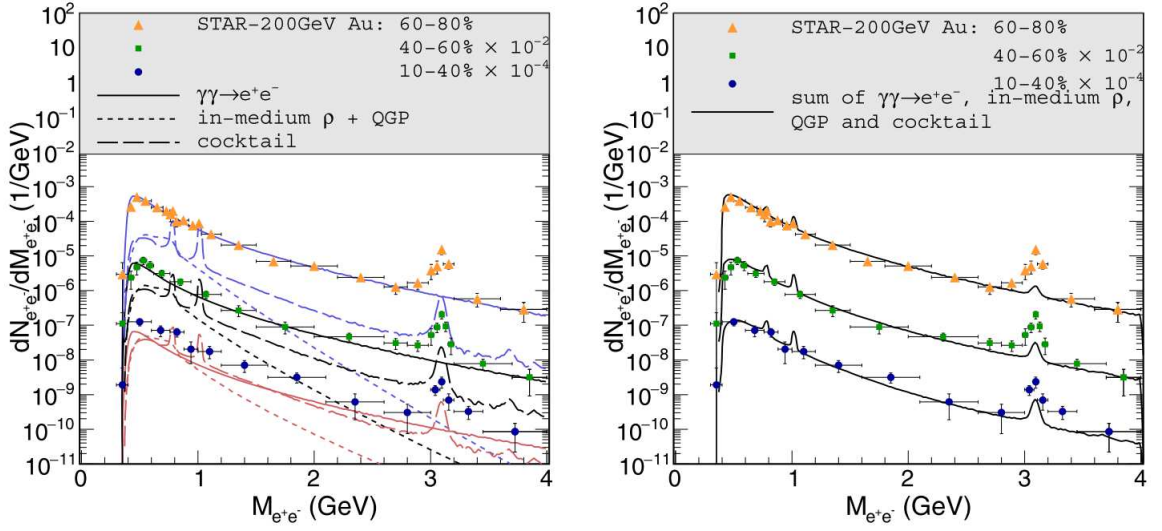


Figure 3.20.: Dielectron mass spectra at $p_{T,ee} < 0.15$ GeV/ c for three centrality classes. Left: Comparison of models for individual dielectron sources to data by STAR. Right: Comparison of the sum of models for dielectron sources to data by STAR [76].

A further photon-photon fusion calculation aiming to describe the STAR low- $p_{T,ee}$ spectra is brought forward in [76]. Exemplarily this approach shall be discussed in more detail in the following. Also here a form factor based on the WS distribution is used. In this calculation the impact parameter dependence of the spectrum in Eq. (3.9) is integrated out, yielding the following differential spectrum:

$$\frac{dN(\omega, q_T^2)}{d^2\vec{q}_T} = \frac{Z^2\alpha_{EM}}{\pi^2} \left| \frac{q_T^2}{(q_T^2 + \frac{\omega^2}{\gamma^2})^2} F_{EM}^2\left(q_T^2 + \frac{\omega^2}{\gamma^2}\right) \right|. \quad (3.10)$$

The $p_{T,ee}$ distribution is calculated as the convolution of the photon spectra of the two colliding nuclei (denoted by the indices 1 and 2) with the cross section $\sigma_{BW}(\gamma\gamma \rightarrow e^+e^-)$ of the Breit-Wheeler process. The resulting $p_{T,ee}$ differential production cross section, which is restricted to experimental selection cuts, can be written as:

$$\frac{d\sigma_{ee}}{d^2\vec{P}_T} = \int \frac{d\omega_1}{\omega_1} \frac{d\omega_2}{\omega_2} d^2\vec{q}_{1,T} d^2\vec{q}_{2,T} \frac{dN(\omega_1, q_{1,T}^2)}{d^2\vec{q}_{1,T}} \frac{dN(\omega_2, q_{2,T}^2)}{d^2\vec{q}_{2,T}} \times \delta^{(2)}(\vec{q}_{1,T} + \vec{q}_{2,T} - \vec{P}_T) \sigma_{BW}(\gamma\gamma \rightarrow e^+e^-)|_{cuts}. \quad (3.11)$$

Here \vec{P}_T denotes the dielectron transverse momentum vector and σ_{BW} is given by [73]:

$$\sigma_{\text{BW}}(\gamma\gamma \rightarrow e^+e^-) = \frac{4\pi\alpha_{\text{EM}}^2}{m_{ee}^2} \left(\left(2 + \frac{8m_e^2}{m_{ee}^2} - \frac{16m_e^4}{m_{ee}^4} \right) \ln \left(\frac{m_{ee} + \sqrt{m_{ee}^2 - 4m_e^2}}{2m_e} \right) - \sqrt{1 - \frac{4m_e^2}{m_{ee}^2}} \left(1 + \frac{4m_e^2}{m_{ee}^2} \right) \right),$$

where m_e is the rest mass of the electron. The kinematics of the photons and the dielectron are related via $m_{ee}^2 = 4\omega_1\omega_2 - P_T^2$ ⁴. To obtain the photon-fusion spectrum for a particular centrality class the cross section in Eq. (3.11) is rescaled to the photo-production cross section at vanishing P_T associated to this centrality class. Directly calculating the impact parameter and P_T differential cross section was avoided since it is very involved.

Using this model of photon-photon fusion together with a model for thermal sources and the hadronic cocktail allows an accurate description of the low- $p_{T,ee}$ mass spectra measured by STAR (see Fig. 3.20, right). In the 60–80% centrality class photo-production dominates the mass spectrum (see Fig. 3.20, left), showing that the photon-fusion model works well. In the more central class of 10–40% all three sources contribute a significant fraction to the yield at masses $< 1 \text{ GeV}/c^2$. The agreement with the data suggests that all relevant sources are well described. An exception is the mass region of the J/ψ , in which the sum of the expectations undershoots the data in all three centrality classes. The authors of [76] interpret this discrepancy as a sign of additional processes which were not considered. Coherent J/ψ production is provided as a likely candidate.

Also the $p_{T,ee}$ spectra corresponding to this model are compared to the STAR data. Figure 3.21 shows the comparison of the model and the data for three different mass intervals in 60–80% centrality. While the low- $p_{T,ee}$ peak due to photo-production is qualitatively reproduced, the width of the peak appears to be underestimated. Thus, a similar discrepancy in the shape as in Fig. 3.18 (lower, right) is found. Since the models based on EPA agree in general with UPC data, one may conclude that additional effects need to be considered in hadronic collisions [72]. This would be in accordance with the centrality dependent broadening of the acoplanarity distributions in the results by ATLAS (see Fig. 3.15, top).

While effects related to trapped magnetic fields in the QGP and rescattering in the medium are discussed as possible explanations for the broadening by the ATLAS [70] and STAR [72] collaborations, [77] proposes a closer investigation of the

⁴This relation can be derived using the four-momenta of the equivalent photons $\mathbf{q} = (\omega, q_x, q_y, \frac{\omega}{v})$ [49] and the approximation $v \rightarrow 1$ (in units where $c = 1$).

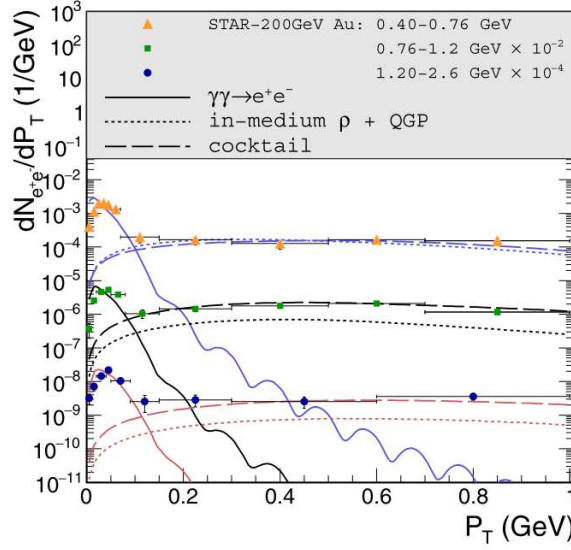


Figure 3.21.: Dielectron $p_{T,ee}$ spectra of expectations for photon-fusion, thermal radiation and the cocktail in comparison to STAR data in 60–80% centrality [76].

photon-fusion process. It is pointed out that in the calculation of the $p_{T,ee}$ spectrum the b dependence of the equivalent photon spectrum has to be considered. This issue is addressed by the generalised EPA (gEPA), which represents is an alternative to the approach based on the b integrated photon spectrum in Eq. (3.10). Using gEPA leads to an improved agreement with the STAR spectra in terms of the shape compared to the STARlight prediction (see Fig. 3.22). The corresponding values for $\sqrt{\langle p_T^2 \rangle}$ in the model and the data are compatible in the 60–80% centrality class.

In addition, it is found that the model predicts a stronger broadening for more central collisions. The corresponding calculations match the ATLAS dimuon data within uncertainties (see Fig. 3.23, left).

Apart from the impact parameter dependence also variations of the photon-fusion production yield with the azimuthal angle are studied in [77]. It is found that production should be increased for dielectron pair momentum directions perpendicular to the event plane, which is the opposite trend as for elliptic flow effects in the medium (see Fig. 3.4 and Fig. 3.23, right).

In [78] interactions of the leptons with the medium are proposed as an alternative explanation of the broadening in the STAR and ATLAS data. It is shown that the dimuon data by ATLAS could eventually be described using the QED analogue of jet-quenching, i.e. electromagnetic interactions with the medium. In addition, observables to distinguish this effect from potential signatures of the magnetic field

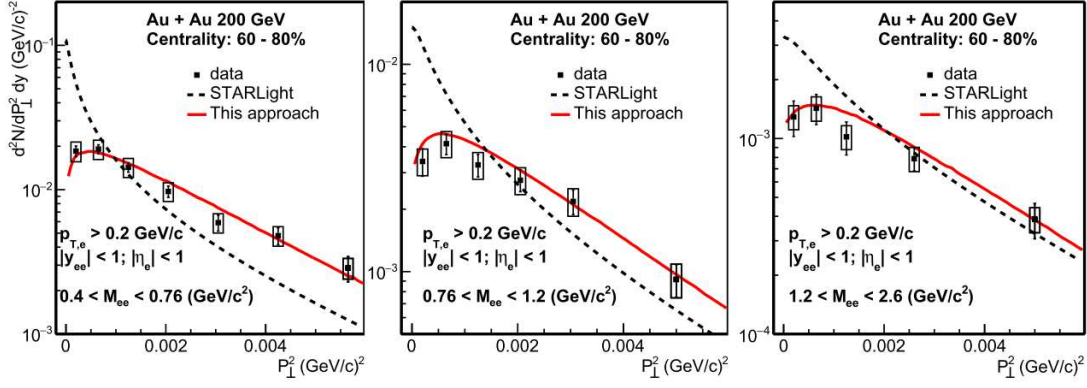


Figure 3.22.: Squared transverse momentum spectra for three mass intervals compared to the corresponding data by STAR [77].

are discussed. This magnetic field is perpendicular to the reaction plane and would deflect the leptons according to the Lorentz law. Since event plane information is available in hadronic collisions the resulting effect could be addressed in azimuthal correlations of the dileptons with the event plane. Also dependencies of magnetic field effects on the collision centrality and the lepton rapidities are proposed for future studies.

The low- $p_{T,ee}$ excess measured by STAR is investigated from an entirely different perspective in [79]. Based on the PHSD model of dielectron production in the hot and dense medium, predictions for the low- $p_{T,ee}$ spectra by STAR are produced. Considered dielectron sources are hadron decays, partonic interactions and semi-leptonic decays of correlated heavy-flavour hadrons. The model incorporates in-medium modifications with respect to pp collisions and describes the $p_{T,ee}$ -integrated dielectron spectra in HICs fairly well. However, they fail at reproducing the observed low- $p_{T,ee}$ excess.

In summary, there seems to be a consensus that the various discussed low- p_T enhancements in hadronic collisions can be attributed to photon-induced processes. However, discrepancies in the shape of measured spectra indicate that the models, which were successfully employed in UPCs, have to be modified. Theoretical approaches to such modifications are based on collision geometry, medium interactions or magnetic fields. The wide range of considered scenarios calls for further experimental data. Since all of them predict effects that depend on the direction with respect to the event plane, this thesis includes a preliminary study of low- $p_{T,ee}$ dielectron production in dependence of the direction relative to the event plane (see Section 5.10).

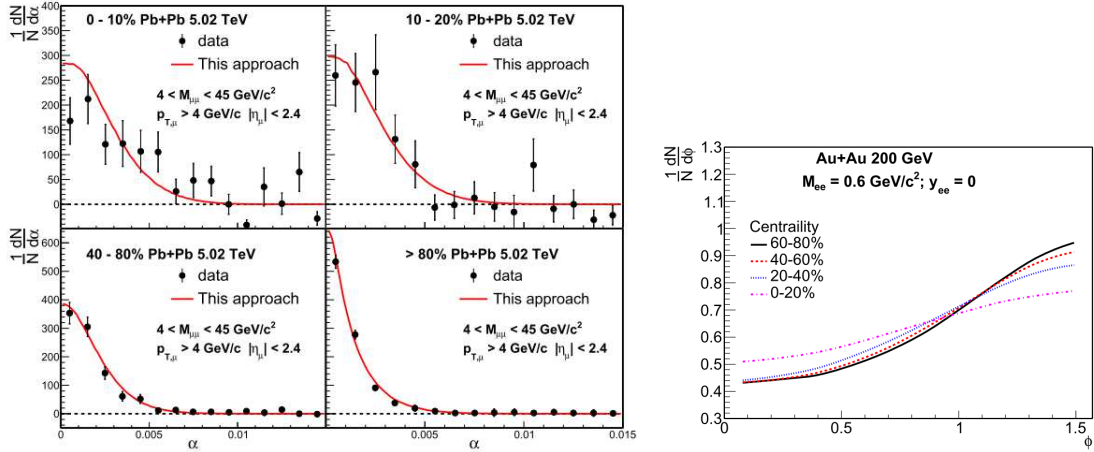


Figure 3.23.: Left: Dimuon acoplanarity distributions based on the gEPA approach compared to corresponding data by ATLAS [77]. Right: Dependence of dielectron production on the azimuthal angle (ϕ) between the dielectron momentum vector and the event plane for different centralities [77].

3.4. Magnetic monopoles

This chapter discusses selected theoretical aspects of magnetic monopoles and the present status of corresponding searches. It shall outline the motivation for the development of a search strategy for such particles in HICs in ALICE (see Chapter 6).

3.4.1. Theoretical perspective

Already in 1269 Petrus Peregrinus of Maricourt found in experiments that magnets always have two opposing poles, i.e. they are dipoles [80]. Besides coining the term “polus” to describe them, he found that breaking a dipole magnet apart to create isolated poles, i.e. monopoles, is not possible. When broken apart, both pieces of the magnet have their own magnetic south and north poles and form a dipole again.

Almost 600 year later, in 1864, this finding was mathematically reformulated as one of the Maxwell equations. These equations are fundamental to our understanding of classical electrodynamics until today. They provide a unified treatment of electric and magnetic phenomena. In the absence of electric or magnetic charges the

equations are invariant under an exchange of the electric (\vec{E}) and magnetic field (\vec{B}) according to: $\vec{E} \rightarrow \vec{B}$ and $\vec{B} \rightarrow -\vec{E}$ [80]. This symmetry is broken as soon as charges are considered. Electric charges of a given sign can be isolated, thus they exist in the form of monopoles. These monopoles act as sources and sinks (depending on the sign of their charge) for the field lines associated to \vec{E} . Based on the found absence of magnetic monopoles the equation for sources and sinks of \vec{B} is not related to a magnetic charge density, but set to zero. This statement is expressed in the Maxwell equations as:

$$\nabla \cdot \vec{B} = 0. \quad (3.12)$$

This equation reflects an experimental finding and is not mandated by deeper theoretical concepts. In fact, the Maxwell equations can be modified without any structural changes to describe magnetic monopoles and their currents. This would extend the symmetry between \vec{E} and \vec{B} to cases with electric and magnetic charges [81].

In the framework of Quantum Mechanics (QM) the \vec{E} and \vec{B} fields are no longer the fundamental entities in electromagnetism. This is necessitated for instance by the Aharonov–Bohm effect [82], which demonstrates that the vector potential \vec{A} can have observable effects even in the absence of \vec{E} and \vec{B} fields [83]. Instead of the \vec{E} and \vec{B} fields, the scalar potential Φ and the vector potential \vec{A} are introduced. The latter is related to \vec{B} via:

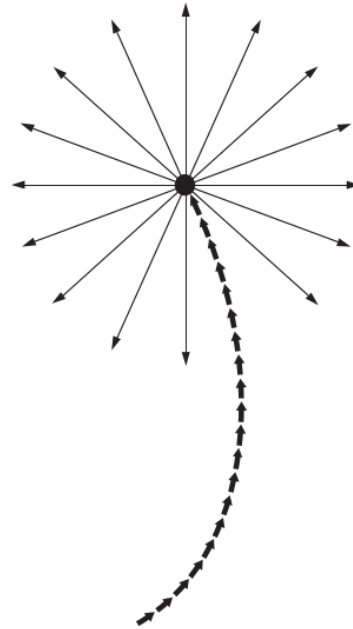
$$\vec{B} = \nabla \times \vec{A}. \quad (3.13)$$

The requirement to express \vec{B} in terms of \vec{A} implies Eq. (3.12). This is a consequence of the identity $\nabla \cdot (\nabla \times \vec{V}) = 0$, which holds for any vector field \vec{V} . Thus, it seems that QM forbids the existence of magnetic monopoles. In 1931 Dirac found that QM and magnetic monopoles can be reconciled [84]. He proposed a vector potential \vec{A}_M of a magnetic monopole that yields the following \vec{B} field [83]:

$$\vec{B} = \frac{g}{r^2} \hat{r} + 4\pi g \delta(x) \delta(y) \theta(-z) \hat{z}, \quad (3.14)$$

where r is the distance to the monopole at the origin, \hat{r} the unit vector pointing to observation point, g the monopole charge, x , y and z are the Cartesian coordinates of the observation point and \hat{z} the unit vector along the z-axis. The first term on the right hand side describes the \vec{B} field of a magnetic charge, which is analogous to the field of an electric point charge. The second term corresponds to an infinitely dense and narrow B-field flux tube along the negative z-axis. This object is typically referred to as a Dirac string. The Dirac string represents a

singular field component, which appears to be hardly reconcilable with physical expectations. Figure 3.24 shows a schematical depiction of this field.



Line of dipoles

Figure 3.24.: Geometry of the magnetic field of a magnetic monopole as proposed by Dirac [83].

To evade quantum mechanical inconsistencies associated to the Dirac string, Dirac imposed that the string is located wherever there are no electric charges (a criterion called the Dirac veto) and that the location of the string has no experimental effects. The Dirac veto alone would not suffice to make the string unobservable, since different string locations correspond to different vector potentials. Conversely, changing the location with respect to the string would result in different observed vector potentials. This could be detected, for instance, via the Aharonov–Bohm effect, and thus the string would still be indirectly detectable. It can be shown that this is not possible if the magnetic charge of the monopole is allowed to take only certain quantised values. This result is known as the Dirac charge quantisation. Several different derivations are outlined and discussed in [83]. The conclusion is that magnetic monopoles can be consistently accommodated in QM under the restriction of the Dirac charge quantisation:

$$qg = \frac{n\hbar c}{2}, \quad (3.15)$$

where q denotes an electric charge, g denotes a magnetic charge, n an integer, and \hbar the reduced Planck's constant. Identifying q with the elementary electric charge e allows the derivation of the values of the elementary magnetic charge g_{D} [83]:

$$g_{\text{D}} = \frac{\hbar c}{2e} = \frac{137}{2}e = 68.5e. \quad (3.16)$$

Thus, magnetic monopoles of unit magnetic charge would experience a electromagnetic interaction in a much stronger way than particles of electric unit charge. As the corresponding magnetic fine structure constant is $\alpha g_{\text{D}}^2/e^2 \approx 34 \gg 1$ perturbative calculations are in general not applicable for magnetic monopoles [83, 85]. Another striking implication of Eq. (3.15) is that the mere existence of a single magnetic monopole in the Universe enforces electric charges to be quantised. In fact, when discovering the charge quantisation condition Dirac was not motivated by the search for magnetic monopoles, but rather by the question why electric charges are quantised. Nevertheless, finding the connection between electric charge quantisation and magnetic monopoles left him optimistic about their existence: "... one would be surprised if Nature had made no use of it." [84].

The concept of a magnetic monopole also arises in the context of Grand Unified Theory (GUT), i.e. a theory that provides a unified description of the strong and electroweak forces. In such theories magnetic monopoles are a required component. These monopoles would have expected masses on the GUT scale, which is $\approx 10^{16} \text{ GeV}/c^2$ [80].

Nevertheless, monopoles could also appear in so far unknown physics at much lower mass scales. Magnetic monopoles of masses on the order of several TeV/c^2 are, for instance, possible in a modified electroweak sector of the Standard Model, which would be compatible with the present experimental data [86]. This demonstrates that on theoretical grounds magnetic monopoles, that are producible at colliders like the LHC, cannot be ruled out [87].

As long as no monopoles are found in collider experiments, the negative search results are interpreted as upper bounds on the production cross section as a function of mass (see Fig. 3.25). These limits should, however, not be taken at face value since they are based on toy models. They rather serve as a comparison of the sensitivity of different analyses [88]. Deriving mass limits for monopoles requires the calculation of the monopole production cross section as a function of the monopoles mass. As mentioned above, due to the strong electromagnetic coupling of monopoles the corresponding calculations are currently not possible [85]. Re-

cently, however, it was argued that these problems do not arise for the production of non-relativistic monopoles anti-monopole pairs ($M\bar{M}$) via the Drell-Yan process ($q\bar{q} \rightarrow \gamma^*/Z \rightarrow M\bar{M}$) and photon-fusion. As a consequence, the derivation of valid monopole mass bounds is considered possible under certain circumstances [89]. The validity of this line of argumentation is, however, substantially criticised in [90]. Another finding in [89] is that, at any monopole mass, photon-photon fusion should be the dominant production mechanism compared to Drell-Yan in pp collisions at the LHC. As pointed out in Section 3.3, coherent photo-photon processes are enhanced by a factor $Z^4 \approx 4.5 \cdot 10^7$ in Pb–Pb collisions. In [91] it is argued, however, that based on the EPA approach (see Section 3.3), HICs appear less suitable than pp collisions for searches of monopole production in photon-fusion at the LHC.

The main motivation for monopole searches in HICs is based on a model of monopole production in strong magnetic fields [92, 93]. The proposed mechanism is Schwinger production, which, as mentioned in Section 3.3, describes the production of dielectrons by sufficiently strong electric fields. Likewise, pairs of a magnetic monopole and its anti-particle could be produced by the enormous magnetic field in a HIC. Under the assumption of a constant magnetic field and a point-like magnetic monopole, the critical field strength B_{crit} for Schwinger production of monopoles with mass m_M is [92]:

$$B_{\text{crit}} = 4\pi \frac{m_M^2}{g^3}. \quad (3.17)$$

Thus, the large value of the magnetic unit charge demanded by the Dirac charge quantisation reduces the field strength required for Schwinger production of a magnetic monopole with unit charge. This approximation is based on the assumption of a constant magnetic field, which is expected to underestimate the actual monopole production cross section. The corresponding mass limit obtained from monopole searches in fixed-target Pb collisions at SPS [94] is on the order of 10 GeV/c^2 [85, 93].

At the LHC higher masses are achievable since the B fields in HICs rise linearly with the center-of-mass collision energy [85]. For Pb–Pb collisions at the LHC corresponding expectations yield masses on the order of 100 GeV/c^2 [85]. Currently exact calculations of monopole production in Pb–Pb collisions at the LHC are not possible as computationally expensive effects related to time dependence of the B field are relevant. Nevertheless, the underlying model of Schwinger production does in principle allow the derivation of mass limits, since it does not have the problem of large coupling, which hampers perturbative calculations. Effects of the QGP are neglected at the LHC, as the B field should decay on a time scale of 10^{-3}

fm/c, while the formation time of the QGP is estimated to be 0.2–0.6 fm/c [92]. Therefore, finite temperature effects are not taken into account. The estimated mass limit of 100 GeV/c² is expected to be a lower bound. As discussed in [85], effects of the time dependence of the B field in HICs should enhance the monopole production substantially and could lead to higher mass limits. Future work shall allow replacing the currently available estimates for monopole mass limits with more rigorous calculations that include the effect of B field dynamics [85, 92]. As long as these problems are not overcome, only estimations on the theoretically reachable masses can be given and thus strict mass limits cannot yet be derived. In view of these theory developments, HICs can be considered as a promising way to search for magnetic monopoles [92].

3.4.2. Search techniques

The properties of magnetic monopoles are barely constrained from theory, and therefore corresponding searches cover a large parameter space. Apart from the Dirac charge quantisation the mass, spin and charge number (i.e. the number of elementary charges) can be regarded as unconstrained. An important exception is the life time. The arguments for electric charge conservation can be applied analogously to magnetic charges. Consequently, magnetic charges should be produced in pairs of stable particles and antiparticles.

There are various different ways of detecting magnetic monopoles. A widely used search technique is based on induction. Just as an electric current induces a circular magnetic field, a magnetic current would induce a circular electric field. Thus, if a magnetic monopole would pass through a superconducting coil it would induce a persistent current [87].

Owed to their strong electromagnetic coupling, monopoles interact intensely with the material they traverse via ionisation. The stopping power, i.e. the energy loss per path length interval $-dE/dx$, of magnetic charges is described by the Ahlen equation, which corresponds to a Bethe-Bloch equation for magnetic charges [95, 96]:

$$-\frac{dE}{dx} = K \frac{Z}{A} g^2 \left[\ln \left(\frac{2m_e c^2 \beta^2 \gamma^2}{I} \right) + \frac{K(|g|)}{2} - \frac{1}{2} - B(|g|) \right], \quad (3.18)$$

where $K = 0.307 \text{ MeV g}^{-1} \text{ cm}^2$ is a constant, Z the atomic number, A the mass number and I the mean excitation energy in the traversed material. The magnetic charge q_m is expressed in terms of the electric elementary charge as $q_m = gec$, with the magnetic charge number g . The terms $B(|g|)$ and $K(|g|)$ represent correction factors and β is defined via the particle's velocity v as v/c and $\gamma = (1 - \beta^2)^{-1/2}$. This equation is expected to be applicable as long as $\beta > 0.1$ [96]. The crucial

difference between the Bethe-Bloch equation (Eq. (4.2)) and Eq. (3.18) is their dependence on β . While $-dE/dx$ reaches a maximum for electrically charged particles as $\beta \rightarrow 0$, it drops for stopping magnetically charged particles. For monopoles $-dE/dx$ would be constantly high as long as they are relativistic (see Fig. 6.2). For both types of charges $-dE/dx$ scales roughly with the square of the corresponding charges. Due to the Dirac charge quantisation this means that $-dE/dx$ is on the order $68.5^2 \approx 4700$ times higher for a unit magnetic charge than for a unit electric charge. Thus, magnetic monopoles would appear as highly ionising particles in $-dE/dx$ sensitive detectors. A corresponding search strategy with ALICE's TPC (see Chapter 4) is presented in Chapter 6.

A complementary strategy for monopole searches at colliders is based on their trajectory [96]. To determine the inverse curvature and thus the transverse momentum of charged particles, magnetic fields are generated in the volume of particle detectors. Due to the Lorentz force electrically charged particles are deflected in a direction perpendicular to their momentum and to the magnetic field of the detector. Tracks of magnetically charged particles would be accelerated along the magnetic field and could therefore be identified rather unambiguously by their curvature along the magnetic field. Commonly applied track finding algorithms may not identify these tracks as they are built on the assumption of no magnetic charges. However, in case an event with a monopole track candidate is found, dedicated track reconstruction could be used to study the curvature along the magnetic field of the corresponding track.

3.4.3. Overview of experimental searches

Searches in astrophysics primarily aim at monopoles which were produced during the Big Bang. These searches found no evidence for monopoles in the cosmos but cannot rule out their existence. In the framework of the widely favoured theory of the inflationary Big Bang, monopole densities could be diluted to undetectably small densities irrespectively of their initial density [80]. As a result it is not possible to derive stringent mass limits from the observed absence of monopoles in the cosmos. Therefore, these searches are not detailed here. See [80, 87] for an overview.

Another strategy is to search for monopoles that are produced at particle colliders. As discussed in Section 3.4.1, the strong coupling of monopoles prohibits perturbative calculations of the production cross section. Consequently, searches at colliders so far cannot be interpreted as limits in the context of realistic models. A recent summary of cross section limits, which are based on simplified assump-

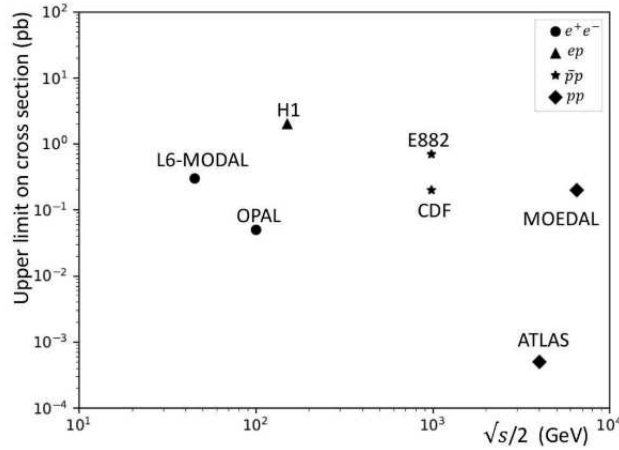


Figure 3.25.: Summary of monopole production cross section limits obtained in monopole searches at colliders. These limits cannot be interpreted as real cross section limits, as they are not derived with realistic monopole production models [87].

tions, is shown in Fig. 3.25.

Typically these models assume Drell-Yan or photon-fusion production kinematics for several different monopole masses, charges and spins. The cross sections are only calculated in the leading order for both production mechanisms. At the LHC corresponding searches were carried out by the MoEDAL [97–100] and ATLAS [88, 101, 102] collaborations in pp collisions.

The MoEDAL detector, which is located next to the LHCb experiment at the LHC, uses passive detectors for monopole searches. Stacks of plastic slices constitute the so-called Nuclear Track Detector (NTD). Highly ionising particles like monopoles would leave tracks in this detector that can be made visible by chemical etching. The ionisation threshold of the NTD is high enough that particles of unit electric charge cannot produce such tracks. In addition, MoEDAL uses a stack of 740 kg of Aluminium as a Magnetic Monopole Trapper (MMT). Monopoles are expected to be bound to the exceptionally strong magnetic dipole moment of the Aluminium nuclei. After data taking, the MMT is cut into 2400 pieces which are scanned using the superconducting coils of a Superconducting Quantum Interference Device (SQUID). If a MMT piece containing a magnetic monopole would be passed through the coil, a persistent current would indicate the magnetic charge. The monopole searches by ATLAS use the Transition Radiation Tracker (TRT) and the Electromagnetic Calorimeter (EMCAL). The search strategy is based on the requirement of a cluster of hits in the TRT, which has a high fraction of detector hits with large charge deposition. This requirement aims at the high stopping power of a monopole. In addition, it is required that there is an EMCAL signal in

the region close to the TRT cluster. Typical monopole masses addressed in these searches are above $200 \text{ GeV}/c^2$. Such particles would not induce a shower in the EMCAL and lead to a very narrow distribution of the energy deposition compared to electrons. Therefore, ATLAS demands an energy deposition with this characteristics in each EMCAL layer. With these two criteria a background free signal region is defined which is used for the search [88].

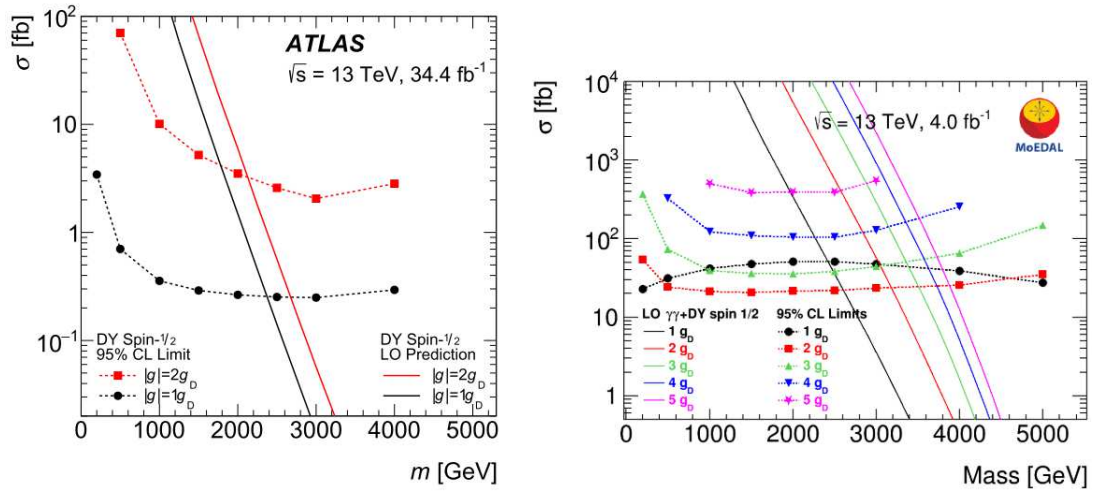


Figure 3.26.: Limits on monopole production cross sections as reported by ATLAS [88] (left) and MoEDAL [100] (right) for spin 1/2 monopoles.

Figure 3.26 shows the mass dependent monopole production cross section limits by ATLAS [88] and MoEDAL [100] for the case of a spin 1/2 monopole in models of Drell-Yan and photon-fusion (only MoEDAL) production in pp collisions. The limits are shown for various different monopole charges and masses. Solid lines indicate the expectations for the cross section based on leading order calculations. Due to the strong electromagnetic coupling these calculations can, however, not be expected to yield realistic results. Consequently, it is stated that these limits should be used for a comparison of the sensitivity of analyses and not as actual limits [87, 88]. As stated in Section 3.4.2, this shortcoming could be overcome by searches in HICs, which, owed to the Schwinger production model, could in principle be used to place general mass exclusion limits on magnetic monopoles. A corresponding search strategy is described in Chapter 6.

4. The ALICE detector

The ALICE (“A Large Ion Collider Experiment”) collaboration operates one of the four large detectors at the LHC [103]. It is optimised for the study of strongly interacting matter at extreme temperatures and pressures in collisions of Pb ions at center-of-mass energies in the TeV regime. The energy scales associated to the strong interaction phenomena of interest in these studies are on the order of hundreds of MeV. Therefore, the ALICE detector is designed to allow tracking (i.e. track reconstruction) of particles down to approximately 150 MeV/ c in p_T . Since central HICs can produce several thousands of particles, high granularity of the detector is a further central design objective.

The ALICE detector (see Fig. 4.1) consists of 19 main components. The most relevant part of the detector to this analysis is surrounded by the so-called L3 magnet (10), which produces a magnetic field of 0.5 T along the beam axis. Collision vertex determination, tracking and Particle Identification (PID) are the primary tasks of these co-called central-barrel detectors (1-9, 16). Their coverage in pseudorapidity is $|\eta| \lesssim 0.9$.

A dedicated group of components including an absorber, a dipole magnet and detectors (11-15) is located in the forward direction ($2.5 < \eta < 4$) for muon detection. Forward detectors (2,17,18), which are located close to the beam pipe, are used for timing and determination of the collision centrality and the spectator event plane (see Section 3.1). Finally, ACORDE is located on top of the L3 magnet and is used to study cosmic rays.

The V0, Inner Tracking System (ITS, 1), Time Projection Chamber (TPC, 3) and Time Of Flight (TOF, 5) detectors are discussed in more detail in the following sections as they are the most important detectors for the dielectron analysis and in case of the TPC also for the search of highly-charged particles.

The Inner Tracking System (ITS) is the inner-most detector of ALICE. It consists of six nested cylinders around the beam axis (see top right panel in Fig. 4.1) [103]. The radii of the cylinders range from 3.9 cm to 42.8 cm. The first two cylinders hold Silicon Pixel Detectors (SPD), which can cope with high densities of charged particles and allow fast readout. The two middle layers are Silicon Drift Detectors (SDD) and the outermost layers are Silicon Strip Detectors (SSD). The SDD and SSD provide information on the particle’s energy loss per path length

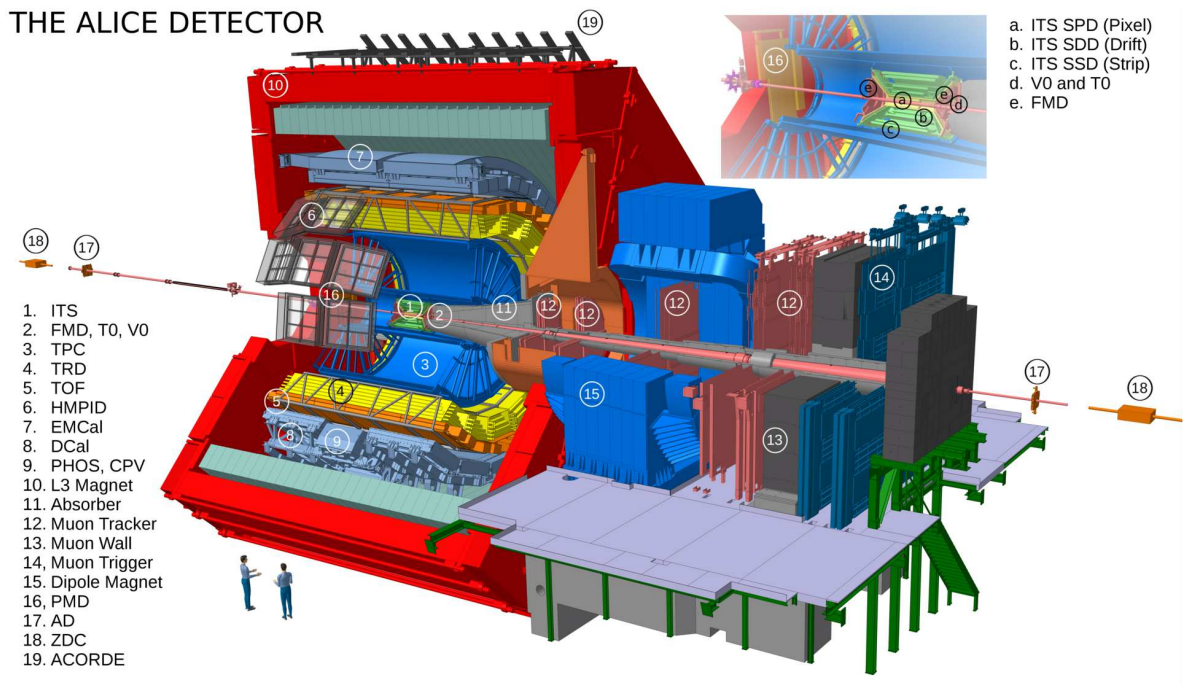


Figure 4.1.: Schematic view of the ALICE detector [104].

$(-dE/dx)$, which is used for PID (see Section 4.1) [30]. The material budget of the ITS corresponds to only 1.1% radiation lengths. This allows tracking of low- p_T particles in subsequent detectors and reduces the amount of dielectrons produced in photon-conversion processes in the ITS material. A key task for the ITS is the localisation of the primary interaction vertex and the identification of secondary vertices. These are vertices of tracks that originate not from the collision vertex but from weak decays of other particles. The resolution for secondary vertex determination is below $100 \mu\text{m}$ for particles with $p_T > 1 \text{ GeV}/c$. This capability plays a central role in this analysis, as it also allows the identification of electron tracks from photon-conversion processes (see Fig. 5.5).

Encompassing the ITS, the Time Projection Chamber (TPC) is 5 m long and covers the radial distance range of 85 - 247 cm [105]. It is essential for tracking and PID. For a charged traversing particle it provides information on the x, y and z coordinates and $-dE/dx$ at up to 159 track points. The volume of the TPC was filled with an Ar-CO₂ mixture during the 2015 Pb-Pb run at the LHC. Charged particles traversing the TPC are ionised. A uniform electric field parallel to the beam axis is produced by high-voltage electrodes at the center and by a field cage (see Fig. 6.3). Electrons produced in the ionisation are accelerated by this field towards the end caps, where their charge signal is amplified and de-

tected in read-out pads, which consist of multi-wire proportional chambers. To achieve fine enough granularity for high track densities, the TPC is equipped with 557568 read-out pads. The radial and azimuthal position of a read-out pad allows deducing the corresponding coordinate of the location of the ionisation which produced the measured charge. The z coordinate is inferred from the drift time, i.e. how long it takes the charge to arrive at the read-out pad and the drift velocity ($\approx 2.7\text{cm}/\mu\text{sec}$). The amount of measured charge in a signal pulse is used to determine $-dE/dx$ of the ionising particle.

The Time-Of-Flight (TOF) detector is located at a radial distance of 3.7 m from the interaction point. It is composed of Multigap Resistive Plate Chambers, which achieve a time resolution of 80 ps for pions at 1 GeV/ c in Pb–Pb collisions [30]. The key element of these detectors are 250 μm wide gas filled gaps which are set under high voltage, such that ionisation of the gas triggers an avalanche process, i.e. the charges are quickly amplified in the electric field. Pick-up electrodes detect this charge generation with high time resolution and indicate the passage of an ionising particle. The event collision time for the TOF measurement is inferred from TOF data or by data from the T0 detectors [106]. The T0 detectors are Cherenkov radiators and use Photo Multiplier Tubes for signal amplification. They are located close to the primary interaction vertex in the forward direction (see top right panel in Fig. 4.1). In Pb–Pb collisions a time resolution of 25 ps is achieved [30]. The TOF information associated to a track can provide valuable information for PID (see Section 4.1). A minimum transverse momentum (p_T) of ≈ 0.4 GeV/ c is required such that a charged particle can reach the TOF detector in the magnetic field.

The V0 detector (2 in Fig. 4.1) provides a measurement of the charged particle multiplicity, which is used for the determination of the collision centrality (see Fig. 3.3). It consists of two arrays of scintillators that form discs around the beam pipes. They are located on both sides of the interaction point at a distance of 330 cm and 90 cm. Its signal is also used to trigger the read-out of other detectors for a given event. Events in the data set for this analysis were required to have coinciding signals in the V0 detectors on both sides of the interaction point. This discriminates events which correspond to collisions of the beam particles with residual gas in the beam pipe [30].

4.1. Particle identification

In this analysis the species of charged particles is identified using input from the ITS, TPC and TOF detectors. The species of a charged particle can be determined

via its charge sign and rest mass. The charge sign can be inferred rather simply from the direction of a track's curvature in the magnetic field. The rest mass, in contrast, requires more information than the trajectory in the spatial coordinates. Assuming unit charge, which is the case for the overwhelming majority of charged particles produced in a collision, one can use the track curvature to determine the track momentum p . The momentum and rest mass m_0 are related via

$$\frac{p}{m_0} = \beta\gamma. \quad (4.1)$$

Thus, in addition to p , also β (which implies knowledge of γ) needs to be determined for PID.

The ITS and TPC allow a measurement of β via the energy loss of a charged particle in the detector material. Particles with $0.1 < \beta\gamma < 1000$ deposit their kinetic energy primarily via ionisation. According to the Bethe-Bloch equation the stopping power, $-dE/dx$, for such particles can be calculated via [96]:

$$-\frac{dE}{dx} = K \frac{Z}{A} \frac{Z_{\text{Proj}}^2}{\beta^2} \left[\ln \left(\frac{2m_e c^2 \beta^2 \gamma^2}{I} \right) - \beta^2 \right], \quad (4.2)$$

where $K = 0.307 \text{ MeV g}^{-1} \text{ cm}^2$ is a constant, Z the atomic number, A the mass number, I the mean excitation energy of the traversed material, and Z_{Proj} the electric charge of the projectile. An important feature of Eq. (4.2) is that the stopping power does not depend on the particle's mass but its $\beta\gamma$ value.

Consequently, particles with different masses and the same p have different $\beta\gamma$ values and thus different stopping power. In the ITS and TPC the $-dE/dx$ values measured for a given track are compared to the expected values for various particle species at a given p (see Fig. 4.2). For the dielectron analysis the identification of electrons is of primary interest. Figure 4.2 (right) illustrates how the stopping power measurement in the TPC allows the separation of electrons from other species over a wide momentum range. While the TPC offers a better stopping power resolution than the ITS (Fig. 4.2, left), it cannot separate electrons from kaons at around $0.5 \text{ GeV}/c$ and protons at around $1 \text{ GeV}/c$, since at these momenta these particle species have the same $-dE/dx$ values. Comparing the two panels in Fig. 4.2 shows that in the ITS these crossings are not visible. The reason for this difference is that for electrons the rise of the stopping power at large $\beta\gamma$ is less suppressed in gas (TPC) than in silicon (ITS), due to the lower electron density in the former (see section on "Density effect" in [87] for details).

The ambiguity of $-dE/dx$ based PID in the crossing regions can be resolved by exploiting a complementary strategy to determine β and thus the particle's species. A particle's velocity v , and equivalently its β , can be inferred via $v = \Delta t / \Delta l$, where Δt is the time interval it takes the particle to cover the distance Δl . The

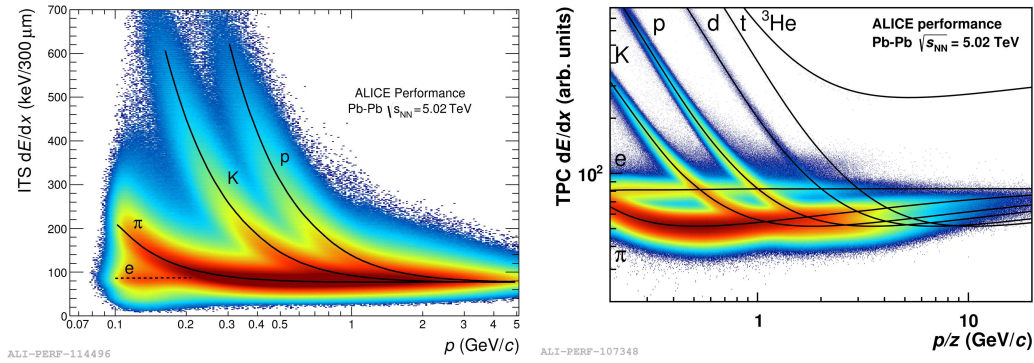


Figure 4.2.: Energy loss measurements in the ITS (left) and TPC (right) compared to expected values for various species (black lines) as a function of the momentum p [107].

time interval Δt is obtained from data of the TOF detector for each individual track. The covered distance Δl is determined via the trajectory and the detector geometry. As Fig. 4.3 shows, these measurements allow the discrimination of kaons and protons in the regions where their stopping powers in the TPC coincide with the ones for electrons (around $0.5\ \text{GeV}/c$ for kaons and around $1\ \text{GeV}/c$ for protons).

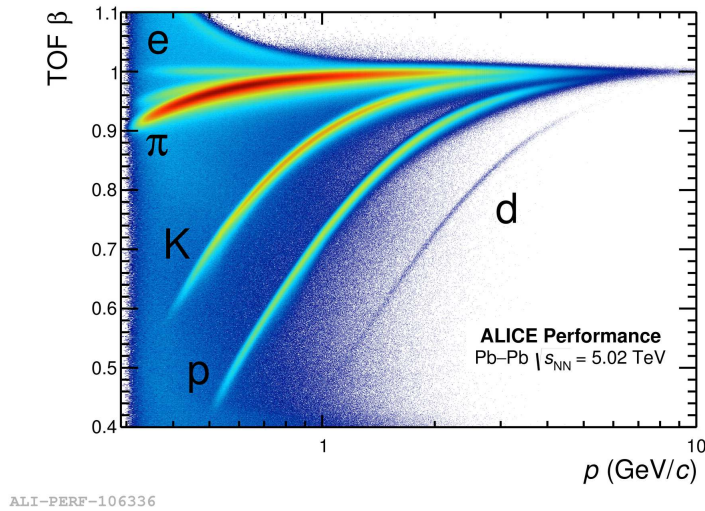


Figure 4.3.: The distribution of measured β values in the TOF detector for various species [108].

The values of the observables $-dE/dx$ and β in the ITS, TPC and TOF are converted to a quantity that expresses by how many standard deviations the measured value differs from the value expected for a certain particle species at a given momentum. This quantity is defined for a given species S and detector Det via:

$$n\sigma_{Det}^S = \frac{O_{Det}^{Meas} - O_{Det}^{Exp,S}}{\sigma_{Det}^S}, \quad (4.3)$$

where $O_{Det}^{Meas/Exp}$ is the measured/expected value for the observable O , which is either $-dE/dx$ or the TOF β . The difference between the measured and expected values is normalised with the resolution of the observable σ_{Det} (see [109] for more details). The calibration of the detectors is done by the ALICE Data Preparation Group and should result in $n\sigma$ distributions that are unit Gaussians for a given species, pseudorapidity and p . For this analysis an additional calibration of the ITS and TPC is used that aims specifically at electron tracks. For this purpose a clean sample of electrons is selected from the data by exploiting the correlation between electron and positron tracks coming from the photon-conversion processes $\gamma \rightarrow e^+e^-$ (see [110] for details). The resulting $n\sigma$ distributions for the tracks used in this analysis are shown in Fig. 5.6.

5. Analysis of dielectrons

The analysis of dielectrons encompasses several data selection steps. The input for the analysis is the calibrated, reconstructed and quality controlled data set of the Pb–Pb run at the LHC in 2015 at $\sqrt{s_{\text{NN}}} = 5.02$ TeV. Tracks passing the event and track selection are used for the dielectron analysis (see Fig. 5.1).

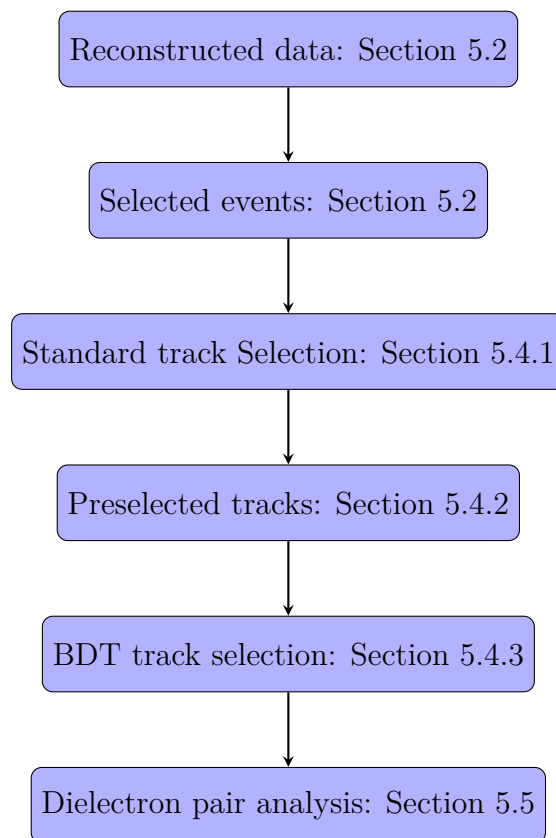


Figure 5.1.: The dielectron analysis chain.

5.1. Monte Carlo simulations

Throughout the analysis multiple data selection criteria are applied (see Fig. 5.1). They are necessary to assure that the analysis is not affected by fake tracks (i.e. tracks that are based on detector hits associated to multiple particles or detector noise), contamination from other particle species or events which represent more than one Pb–Pb collision (so-called pile-up events). In each of these steps the fraction of undesired data (so-called background) is reduced. Additionally, even without any selection cuts the probability for any given electron and positron to be reconstructed as a corresponding track is smaller than unity (this quantity is called reconstruction efficiency). The results of the analyses are compared to theory calculations, which do no account for these efficiencies, but assume perfect signal reconstruction efficiency and background rejection. Therefore, the measured results (so-called raw spectra) have to be corrected for the finite signal efficiencies. To estimate these efficiencies Monte Carlo (MC) simulations are used. In these simulations particles are generated according to expectations for a given physics process. These particles are then propagated through a virtual model of the detector. Based on the simulated detector hits the reconstruction is carried out and the same data selection as in the analysis on real data is applied. Knowing the amount of signal that was originally generated and the amount of signal that was reconstructed and passed the selection criteria, allows the determination of the signal efficiency (see Section 5.5.2). The resulting corrected spectra can then be compared quantitatively to theory expectations.

For the data set used in this analysis a MC data set was produced to estimate the signal efficiencies for dielectrons. In the simulation particles are produced by the event generator HIJING [111]. It generates events, i.e. a set of particles and their initial momenta, according to probability density functions that represent the expectations based on a QCD based-model, PYTHIA [112], and measured branching ratios. HIJING treats a HIC as a superposition of the corresponding nucleon-nucleon collisions. It does not account for effects on dielectrons or their sources, which are attributed to the produced medium or electromagnetic interactions.

Once the MC generator provides the particles of an event, they are propagated through the detector by GEANT3 [113]. Interactions of the particles with the detector material and the magnetic field of the detector as well as the production and decay of secondary particles are simulated in this step. Of particular importance is the interaction with sensitive detector material. These are the parts of the detector which produce a signal when enough energy is deposited in their volume. Together with models of the signal generation in the detectors, these simulations can be used to reproduce the detector response to a HIC. For each individual data

taking period dedicated MC simulations are carried out with the corresponding detector configurations and operation conditions. From this point onwards, in general, the same data processing and reconstruction algorithms as on real data are applied. Since generator information on the true particle species, origin and momentum is kept, the resulting reconstructed event can be used to calculate the reconstruction efficiencies of objects like single tracks or, as in this analysis, for dielectrons. In addition, the comparison of the generated and reconstructed track observables allows an estimation of the resolution of reconstructed track observables like the transverse momentum p_T .

Since dielectrons are produced rather rarely the MC data set was generated with an artificial enhancement of dielectron sources. In addition to the dielectron sources generated by HIJING, the following dielectron sources were injected in each event:

- J/ψ and light-flavour mesons: $\pi^0, \eta, \eta', \rho, \omega, \phi$, and J/ψ flat in p_T and pseudorapidity $|\eta| < 1.2$ with forced decays into dielectrons
- one of the following three heavy-flavour sources in ratios of 1:1:3:
 - $c\bar{c} \rightarrow$ dielectrons via forced semi-leptonic decays, an event is accepted only if dielectrons from c decays are in $|\eta| < 1.2$
 - $b\bar{b} \rightarrow$ dielectrons via forced semi-leptonic decays, an event is accepted only if dielectrons from b decays are in $|\eta| < 1.2$
 - $b\bar{b}$ events without forced semi-leptonic decays, an event is accepted if at least one electron comes from b or $b \rightarrow c \rightarrow e$ and is in $|\eta| < 1.2$.

5.2. Dataset and event selection

The analysed data set was recorded in the Pb–Pb run of the LHC in 2015. This data taking period is subdivided into so-called runs, which represent sub-periods, in which all detector, data acquisition and beam configurations are kept constant. The ALICE Data Preparation Group performs calibration, reconstruction and Quality Assurance (QA) on the recorded runs and provides lists of runs which are eligible for different types of analyses. In the present analysis the central-barrel detectors (see Chapter 4) play a crucial role, therefore only runs with a positive QA outcome for these detectors are selected. The corresponding run list for this

requirement contains 97 runs.

This analysis uses events that were recorded with minimum bias triggers, i.e. an event is selected if there is a coincidence of signals in the V0A and V0C detectors (see Chapter 4). Events that are related to interaction of the Pb beams with residual gas in the vacuum beam pipe, are rejected offline by using V0 and ZDC (see Chapter 4) timing information.

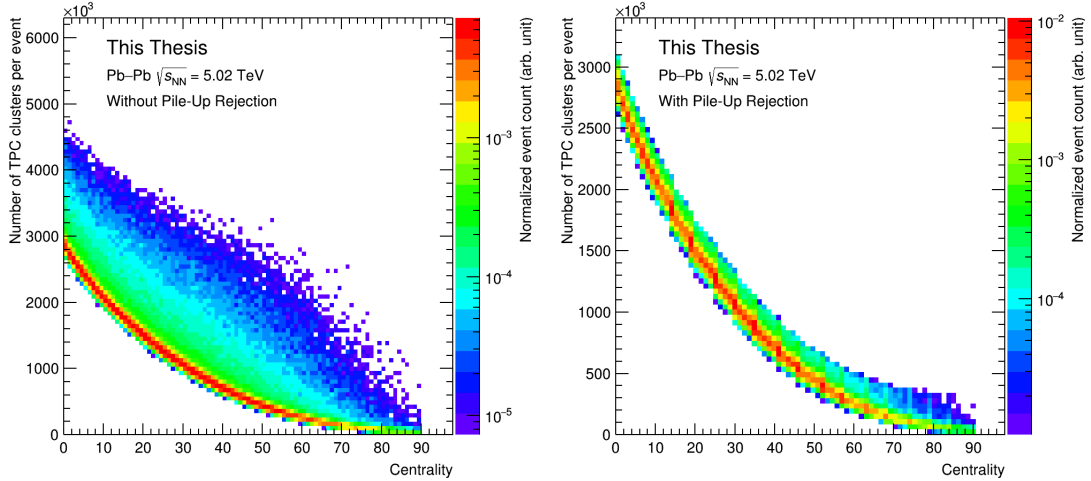


Figure 5.2.: The distribution of events in the plane of number of TPC clusters (y-axis) and centrality (x-axis). Left: without pile-up rejection. Right: with pile-up rejection.

The events are required to have an associated collision vertex, which is the estimated position of the HIC in the coordinate system of the detector. The next selection criterion is based on z_{Vertex} , which is the displacement of the event vertex along the z-axis (i.e. along the beam direction) with respect to the nominal interaction point. To ensure that all the events have approximately the same effective detector acceptance in pseudorapidity, a selection of $|z_{\text{Vertex}}| < 10$ cm is applied. Events are also selected in terms of their centrality (see Section 3.1). The centrality range is specified for each shown analysis result. The centrality assigned to an event is estimated from the V0M centrality estimator, which is based on the sum of the signal amplitudes in V0A and V0C (see Section 3.1). Closely related to this cut is the rejection of so-called Out-of-Bunch Pile-up (OBP). These are events in which collisions associated to the primary bunches of beam particles and neighbouring bunches occur within the read-out time window of the detectors. This issue is particularly relevant for detectors with long read-out times like the TPC. The centrality attributed to a given event does typically not change due to OBP,

since the V0 detectors have a time window that is too narrow. If there is no OBP there is a rather narrow distribution of the number of clusters¹ in the TPC per event in a given centrality bin. However, due to its longer time window, the TPC may record clusters associated to tracks from OBP. Therefore, the distribution of TPC clusters per event in a given centrality range receives a tail along the positive direction due to OBP. Figure 5.2 shows the distribution of TPC clusters per event (y-axis) versus centrality (x-axis). The pile-up rejection cut removes events that are above a polynomial function of the centrality, which was adjusted by hand to reject the tail associated to OBP. The effect of this cut can be seen by comparing the distributions before the pile-up rejection cut (Fig. 5.2, left) and afterwards (Fig. 5.2, right). This cut is applied only to data and not to MC, since OBP is not simulated.

These event selection cuts lead to the following number of events in data and MC:

0–40%	Events
Data	31 M
MC	618 k
70–90%	Events
Data	15 M
MC	348 k

Table 5.1.: Number of accepted events.

5.3. Signal and background definitions

In this analysis signal dielectrons are pairs of unlike charge sign e^+e^- tracks which were produced as a pair at the primary interaction vertex (Fig. 5.3, top) or from correlated open heavy-flavour hadron decays (Fig. 5.3, bottom). The former are dielectrons from hadron decays (“h” in Fig. 5.3) or prompt dielectrons that are either produced directly at the collision (e.g. Drell-Yan production or photon-photon fusion) or in the subsequently created hot medium (e.g. virtual thermal photons). In each of these cases both tracks of the dielectron have the same mother particle. Dielectrons from photon-conversion processes in the material surrounding the primary interaction vertex (indicated as “ γ ” in Fig. 5.3) are defined as background. In addition, all dielectrons that originate from different microscopic processes are

¹This is a group of detector hits (so-called digits) which is associated to one track.

considered as so-called combinatorial background.

Figure 5.4 shows simulated invariant mass spectra coming from HIJING. Dielectrons which have the same mother particle and are not photon-conversions are shown in cyan. The corresponding spectrum does not have a realistic shape, since only the π^0 and η meson are included as dielectron sources in HIJING (a more realistic spectrum is shown in Fig. 5.13 and Fig. 5.14). The remaining mesons are added via the aforementioned injections (not shown).

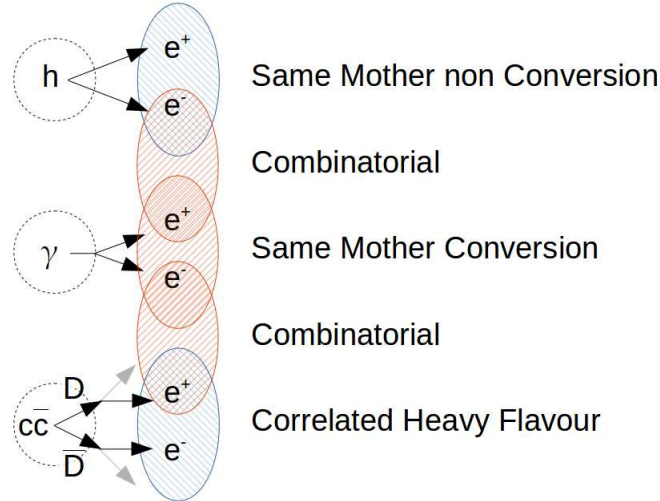


Figure 5.3.: Signal (blue) and background (red) definition of dielectrons.

In 0–40% centrality (Fig. 5.4, left) the main background source are combinatorial dielectrons with one or both tracks from a photon-conversion (magenta in Fig. 5.4). It exceeds the signal (green), which is composed of the same mother non-conversion pairs (cyan) and dielectrons from correlated heavy-flavour (HF, black) hadron decays, by up to more than two orders of magnitude. In 70–90% centrality (Fig. 5.4, right) the impact of this background source is less severe but the associated yield is still comparable to the signal. Pairs of electron tracks coming from the same photon-conversion process are shown in red. Since they originate from real photons their reconstructed invariant mass is typically close to zero and therefore not relevant in this analysis (the minimum mass studied is $0.5 \text{ GeV}/c^2$).

Although the signal and background contributions in this simulated data set are not realistic, it is evident that conversion electrons represent a major challenge to dielectron analyses. Electron tracks from photon-conversions give rise to considerable combinatorial background over the whole mass spectrum. Therefore, they are treated by dedicated track selection cuts as discussed in the next section.

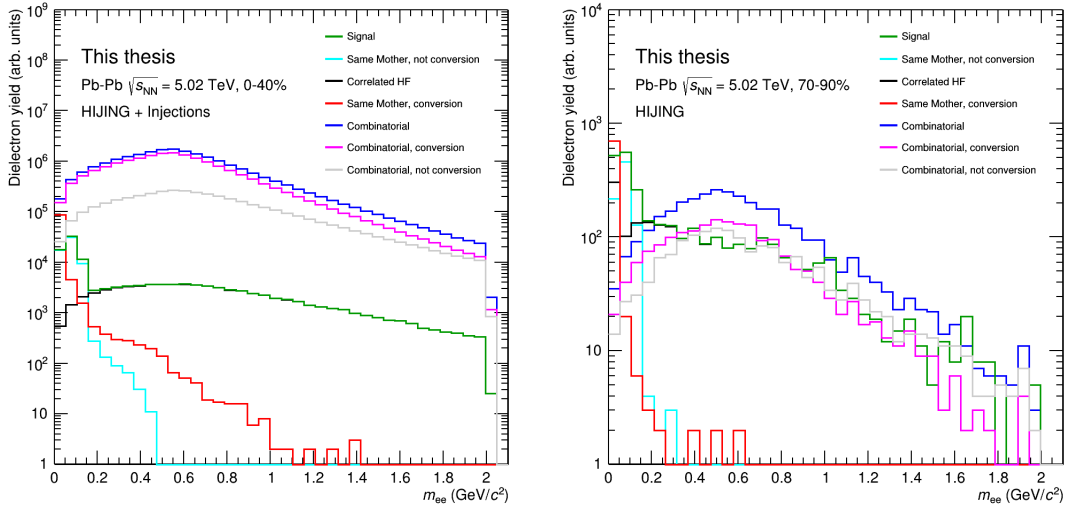


Figure 5.4.: Mass spectra of individual dielectron sources simulated with HIJING in 0–40% (left) and 70–90% centrality (right). Preselection cut 0 is applied (see Table 5.2).

5.4. Track selection

In the following the cuts which are used for track selection are detailed. These cuts are grouped according to their purpose in the analysis.

5.4.1. Standard selection cuts

The first group of cuts aims at a pure selection of high quality tracks. This means that the tracks are very likely to be associated to a real particle and the extracted kinematic parameters represent a good approximation of the real ones. These cuts are applied in each of the shown dielectron spectra of this analysis, unless stated differently. Geometry and the material budget of the detector define the pseudorapidity (η_e) and transverse momentum ($p_{T,e}$) range, in which electron candidate tracks pass the detector components necessary for reliable tracking. The tracking procedure aims at inferring track parameters like η_e and $p_{T,e}$ from groups of detector hits, so-called clusters. These clusters are connected under constraints derived from the assumption that they lie on a single particle trajectory. This process starts in the outer pad rows of the TPC, where track finding proceeds towards the inner rows. In this step TPC tracks are created. These tracks are

then propagated towards the outer layer of the ITS, where they serve as input for track finding towards the inner ITS layers. Afterwards, these tracks are propagated outwards and inwards once more using a Kalman filter [114]. In this process the kinematic observables and track quality, i.e. how well the track fits the hypothesis that its clusters belong to the same particle trajectory, are determined (see [30] for details).

The choice of the selection cuts is not optimised in this analysis as it is based on the experience of numerous preceding analyses. The signal efficiency associated to these cuts is close to unity. The selection criteria are listed in the following:

- $p_{T,e}$ within $[0.2, 8.0]$ GeV/ c ,
- η_e within $[-0.8, 0.8]$,
- DCA_{xy} within $[-1.0, 1.0]$ cm,
- DCA_z within $[-3.0, 3.0]$ cm,
- ITS tracking,
- TPC tracking,
- rejection of kink daughters,
- successful refit of the TPC and ITS track.

The Distance of Closest Approach in the xy -plane and along the z -axis (DCA_{xy} and DCA_z) are the distance between the primary vertex and the track-point closest to primary vertex (see Fig. 5.5, left). Tracks from photon-conversion processes have an increased DCA_{xy} as their production point is displaced with respect to the primary vertex. Figure 5.5 (right) shows the simulated DCA_{xy} distribution of photon-conversion tracks in red. The applied cut of $|DCA_{xy}| < 1$ cm does not cut significantly into the DCA_{xy} distributions of the light- (LF, defined in Section 3.2.1) and heavy-flavour (HF, defined in Section 3.2.2) signal electrons. However, this cut still accepts a significant amount of photon-conversion electrons. Also the cut on DCA_z has a signal efficiency close to unity.

Requirements are also placed on ITS tracking parameters. Tracks need to have a cluster associated in the first layer of the SPD, which is the inner most silicon tracking detector. This effectively rejects photon-conversions in the subsequent ITS layers or late weak decays after the SPD. In addition, tracks must have associated clusters in at least three of the six ITS layers. The overall quality of the track is restricted by the criterion $\chi_{ITS}^2/n_{Cl}^{ITS} < 15$, where χ_{ITS}^2 measures the

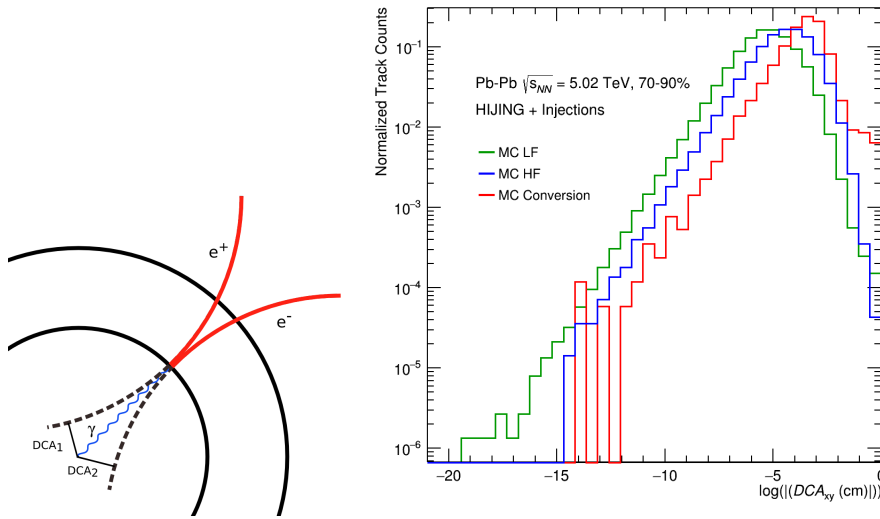


Figure 5.5.: Left: Schematic explanation of the Distance of Closest Approach (DCA) for a conversion of a photon (γ) into a dielectron. Right: Distribution of DCA_{xy} in MC (HIJING + injected sources) for various different electron sources. Electrons from light-flavour (LF) meson decays are shown in green, from heavy-flavour (HF) hadron decays in blue and from photon-conversions in red.

deviation between the cluster locations in the ITS layers and the points where the associated reconstructed track penetrates the layer. The average deviation per cluster is calculated by dividing with the total number of ITS clusters $n_{\text{Cls}}^{\text{ITS}}$ belonging to the track. Placing an upper limit on this quantity reduces the number of photon-conversion and fake tracks.

An analogous cut is placed on the TPC tracking quality. Here the criterion is $\chi_{\text{TPC}}^2/n_{\text{Cls}}^{\text{TPC}} < 8$. As a track passes through the TPC a cluster can be associated to the track in each pad row (see Chapter 4 and Fig. 6.3). However, due to dead zones the maximum number of findable clusters, which is based on the track kinematics, can be lower than the number of actually crossed rows. Conversely, the number of actually crossed pad rows can be smaller than the number of findable clusters. This would, for example, be the case if a track's kinematics at the innermost pad row would allow it to cross all pad rows, i.e. it has 159 findable clusters, but in the middle of the chamber the track is lost due to interactions with the gas. Then only half the number of pad rows were actually crossed while there are 159 theoretically findable clusters. Tracks are required to have a ratio of findable clusters over crossed rows of at least 80 % and at maximum 105%. In addition, there needs to be an associated cluster to the track in at least 100 of the 159 possible pad rows.

If the particle associated to a track undergoes a decay while traversing the detector (e.g. $K^\pm \rightarrow \mu^\pm + \nu$) the trajectory of the track abruptly changes. This is called a kink and the subsequent part of a track is called the kink daughter (in the previous example this is the μ^\pm). Tracks that are identified as candidates for kink daughters are rejected from the analysis.

Finally, the last inwards pointing refit in the TPC and the ITS with the Kalman filter is required to be successful for each track (see [30] for more details on track reconstruction).

5.4.2. Preselection cuts

The second group of cuts are the preselection cuts. These cuts are not kept fixed in this analysis like the standard cuts, but are studied in different variants and compared in terms of performance (see Section 5.8.2). In addition, the different variants of this cut group are used for the estimation of the systematic uncertainty. The variables used for the preselection cuts and the corresponding ranges are shown in Table 5.2. The cuts described in the last two rows are only used for a cross-check of the PID selection (Section 5.11.1) and not for the actual analysis. The range of variables for these cuts is obtained by a random selection of predefined values. The cuts will be referred to by the preselection cut number in the first column. The second and third row show the selected ranges for the TPC cluster number (TPC cl.) and the crossed rows in the TPC (TPC cr. rows). In the remaining columns variables for PID are shown. As pointed out in Section 4.1, the ITS, TPC and TOF detectors provide PID information in terms of $n\sigma$ values (see Eq. (4.3)). For $n\sigma_{\text{TPC}}^e$ and $n\sigma_{\text{ITS}}^e$ (see Eq. (4.3)) the tracks are required to have values within the specified intervals. Conversely, tracks are rejected if their $n\sigma_{\text{TPC}}^\pi$ falls into the range specified in the fifth column, which shall reject tracks from π^\pm . The analysis includes tracks below the minimum p_T acceptance threshold of the TOF. Therefore, a cut on $n\sigma_{\text{TOF}}^e$ is only applied if a TOF hit is associated to the track.

Figure 5.6 shows the distribution of $n\sigma_{\text{TPC}}^e$, $n\sigma_{\text{ITS}}^e$, and $n\sigma_{\text{TOF}}^e$ of positively charged tracks for the preselection cut 0 and MVA cut 5 (see Section 5.4.3). The column on the left hand side shows the distributions as a function of η_e . As expected these distributions are centered around zero at the y-axis ($n\sigma$) and flat along the x-axis (η_e). The column on the right hand side of Fig. 5.6 shows the distributions as a function of $p_{T,e}$. After recalibration electrons are distributed around zero in $n\sigma$ in each $p_{T,e}$ slice. There is an expected indication of contamination in the negative $n\sigma_{\text{TPC}}^e$ region at $p_{T,e} < 1 \text{ GeV}/c$. The concern of an impact of PID contamination

Cut Nr.	TPC cl.	TPC cr. rows	$n\sigma_{\text{TPC}}^e$	$n\sigma_{\text{TPC}}^\pi$ excl.	$n\sigma_{\text{ITS}}^e$	$n\sigma_{\text{TOF}}^e$ if avail.
0	[100, 160]	[100, 160]	[-2.0, 3.0]	[-100, 4.5]	[-3.5, 0.5]	[-3.0, 3.0]
11	[80, 160]	[80, 160]	[-2.0, 3.5]	[-100, 3.5]	[-3.5, 0.5]	[-2.5, 3.0]
12	[80, 160]	[80, 160]	[-1.0, 3.5]	[-100, 3.5]	[-3.5, 1.0]	[-2.5, 3.0]
13	[100, 160]	[100, 160]	[-2.0, 3.0]	[-100, 3.5]	[-3.0, 1.0]	[-3.0, 2.5]
14	[80, 160]	[80, 160]	[-1.5, 3.0]	[-100, 4.5]	[-3.0, 1.0]	[-2.5, 3.0]
15	[80, 160]	[100, 160]	[-2.0, 3.0]	[-100, 4.5]	[-3.0, 1.5]	[-3.0, 3.0]
16	[100, 160]	[100, 160]	[-2.0, 3.0]	[-100, 4.5]	[-3.5, 0.5]	[-3.0, 3.0]
17	[80, 160]	[80, 160]	[-2.0, 3.0]	[-100, 3.5]	[-3.5, 0.5]	[-2.5, 3.0]
18	[100, 160]	[100, 160]	[-2.0, 3.5]	[-100, 3.5]	[-3.5, 0.5]	[-3.0, 3.0]
19	[100, 160]	[100, 160]	[-2.0, 3.0]	[-100, 4.5]	[-3.5, 1.0]	[-2.5, 3.0]
20	[100, 160]	[100, 160]	[-2.0, 3.0]	[-100, 4.5]	[-3.0, 1.0]	[-3.0, 2.5]
-98	[100, 160]	[100, 160]	[-2.0, 3.5]	[-100, 4.5]	[-3.5, 1.5]	[-3.0, 3.0]
-99	[100, 160]	[100, 160]	[-1.0, 2.5]	[-100, 3.5]	[-3.0, 0.5]	[-2.0, 2.5]

Table 5.2.: Definition of preselection cuts.

on this analysis is addressed in Section 5.11.1.

The following table reports the number of tracks that pass the preselection track cut 0.

0–40%	Tracks
Data	212 M
MC	3 M
70–90%	Tracks
Data	1.6 M
MC	0.8 M

Table 5.3.: Number of accepted tracks with preselection cut 0.

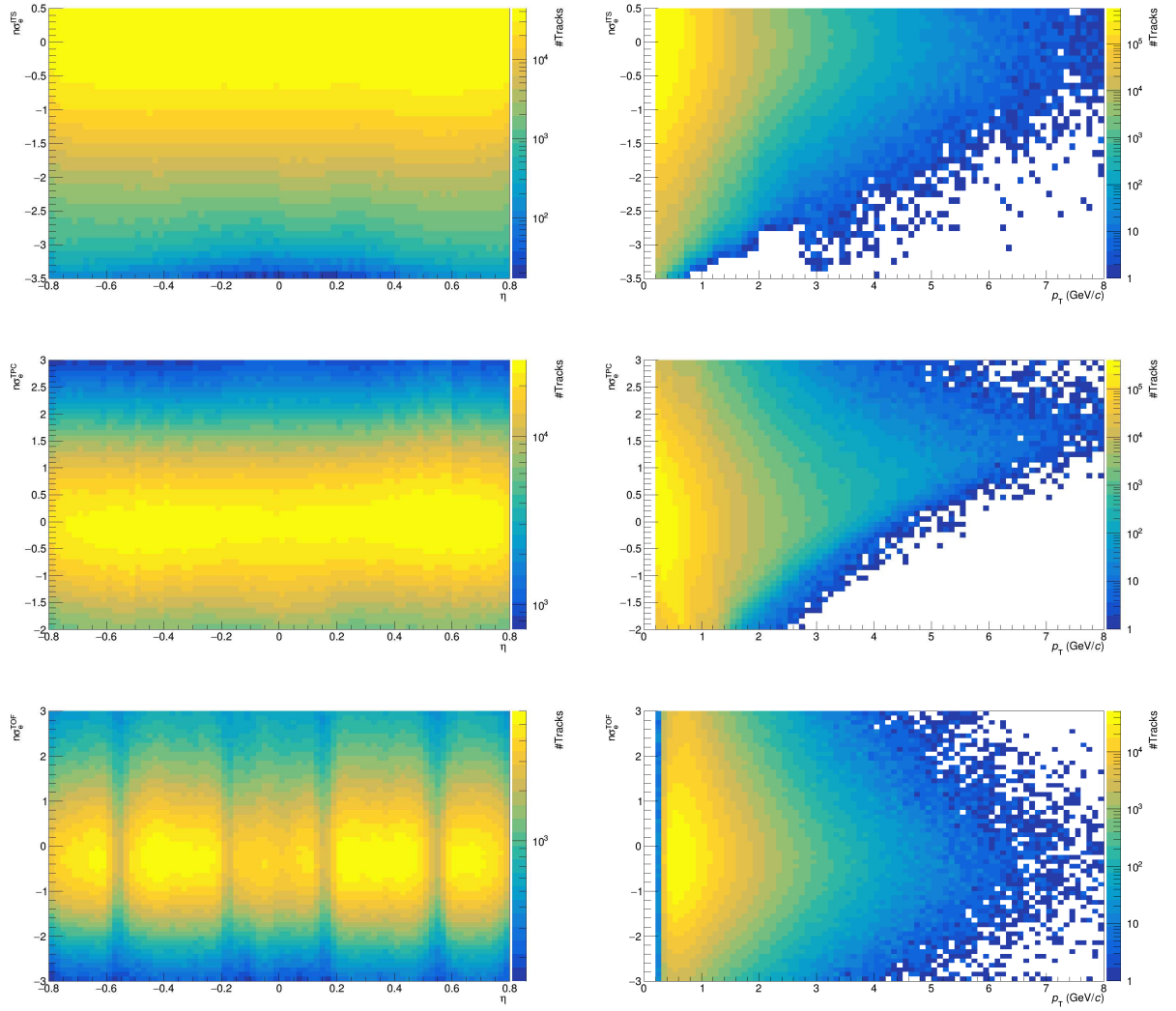


Figure 5.6.: Distribution of electron PID variables $n\sigma_{\text{ITS}}^e$ (top row), $n\sigma_{\text{TPC}}^e$ (middle row) and $n\sigma_{\text{TOF}}^e$ (bottom row) of positively charged tracks in η_e (left column) and $p_{T,e}$ (right column) for preselection 0 and MVA 5 in 0–40% centrality Pb–Pb collisions at $\sqrt{s_{\text{NN}}} = 5.02$ TeV.

5.4.3. BDT based photon-conversion rejection

To reduce the large background from combinatorial dielectrons with a photon-conversion track (see Fig. 5.4) it would be desirable if conversion tracks could

be rejected by the track cuts. Due to their displaced production vertex conversion tracks can be distinguished from other tracks by track quality parameters. Since track quality parameters are often correlated to track kinematics, kinematic variables are also considered useful in the identification of conversions. Thus, to achieve optimal conversion rejection the classification has to be based on multiple track variables.

Learning to identify conversion tracks based on track observables is equivalent to finding the ideal decision boundary between conversion and non-conversion regions in a high dimensional space spanned by these variables. Multivariate classification problems like this are commonly approached using machine learning algorithms. These so-called classifiers have free parameters that can be tuned to a specific classification problem. This process is called supervised learning. In simplified terms, the classifier is asked to provide its decision for a data sample for which the ground truth is known. In the present case a data sample is a track represented by the input variable vector x and the ground truth of its class y_0 , which is either 1 for signal or -1 for background. Afterwards, the classifier adapts its parameters in a way that should improve the quality of its predictions. In the problem of conversion rejection the MC simulation provides examples of tracks together with the ground truth of their origin, i.e. whether the track comes from a photon-conversion.

The learning procedure is carried out using a randomly selected subset of the MC data set, which is called the training data set. Afterwards, the classification performance is evaluated again on a further randomly selected subset of the MC data set, the test data set. This allows the detection of overtraining, which occurs when the classifier achieves better performance on the training data set than on the test data set. A reason for this may be that the classifier adapts its decision boundary to statistical fluctuations in the training data set. On the test data set such adaptations do in general not improve the performance since they do not generalise to statistically independent data sets. Therefore, this data set is useful to detect overtraining. For a more detailed discussion of this and related machine learning concepts see [115].

Tracks passing the preselection cut 0 serve as training and test data set. The choice of the preselection track cut is not expected to lead to different characteristics of conversion and non-conversion tracks. Therefore, a classifier trained on the data obtained with one specific preselection cut can be applied to data sets obtained with different preselection cuts. The target classes are tracks from a conversion process (background tracks) and the remaining tracks from hadron decays (signal). The following input variables are used by the classifier:

- number of ITS layers with associated hits
- ITS shared 1-6: if a track's ITS cluster in one of the six ITS layers is shared

with a different track

- fraction of shared ITS clusters
- $\log(|DCA_{xy}|)$ (DCA_{xy} in cm)
- $\log(|DCA_z|)$ (DCA_z in cm)
- χ_{Gl}^2/n_{Cls}^{Gl}
- χ_{ITS}^2
- has SPD First Hit: if there is a cluster in the first SPD layer
- η_e
- $p_{T,e}$ (GeV/ c)
- centrality.

Here χ_{Gl}^2/n_{Cls}^{Gl} denotes the normalised χ^2 deviation between the reconstructed track and the associated clusters for global tracks, i.e. tracks which are obtained by tracking in the ITS and TPC. The DCA and χ^2 variables are explained in Section 5.4.1. The MC data set is used with all its aforementioned injections (see Section 5.1). Thus, it does not represent a dielectron data set with a realistic fraction of the individual signal and background components. However, the typical characteristics of signal and background is not affected by these injections. The distinguishing characteristics between conversion and non-conversion tracks is related to the detector material and the reconstruction, both of which are the same for standard and injected tracks. Therefore, to minimise statistical fluctuations, the injected dielectron signal sources are also used for training.

A Boosted Decision Tree (BDT) with gradient boosting in TMVA [116] serves as the classifier algorithm and shall be conceptually explained in the following. In very simple terms, decision tree classifiers consecutively split the data set in a way that produces data subsets, so-called nodes, of high signal and background purity. Each time a split is performed, the classifier tries to find the ideal variable and corresponding cut value for the next split. The resulting two nodes are then split again with the same goal. This algorithm proceeds until a stopping criterion is reached. One possibility is that the predefined maximum number of splits was reached. Alternatively, the algorithm may stop earlier if the number of remaining samples in a node becomes smaller than the minimal amount of data per node, or if the purity cannot be improved any further. The learned splitting criteria are stored and define the decision boundary.

Once a decision tree is fully grown, the trained tree T_0 can make a prediction $T_0(x)$ for track represented by the input variables x . For this the node to which this sample belongs is identified by passing it through the tree. The prediction

for a given node is the average of the target values, y_0 (1 for signal and -1 for background), for the data samples that ended up in this node during training. Next a new tree is grown. This tree is trained to predict the residual difference between the prediction of the previous tree $T_0(x)$ and its target, the real class label y_0 . This process is repeated, i.e. the k -th tree is trained to approximate the residual error of the previous tree T_{k-1} with respect to its target y_{k-1} :

$$T_k(x) \rightarrow y_{k-1} - T_{k-1}(x), \quad (5.1)$$

until a predefined number of trees is trained. At this point the training phase is finished. Now the classifier can be used to predict the class of a given data sample. To do so, the node corresponding to the data sample is determined in each tree. The predictions $T_k(x)$ returned by the trees are summed up and the resulting number, often called the Multivariate Analysis (MVA) output, between $[-1, 1]$ serves as a prediction for the class of track. The larger (smaller) the MVA output for a track the more it appears to have signal (background) characteristics to the classifier.

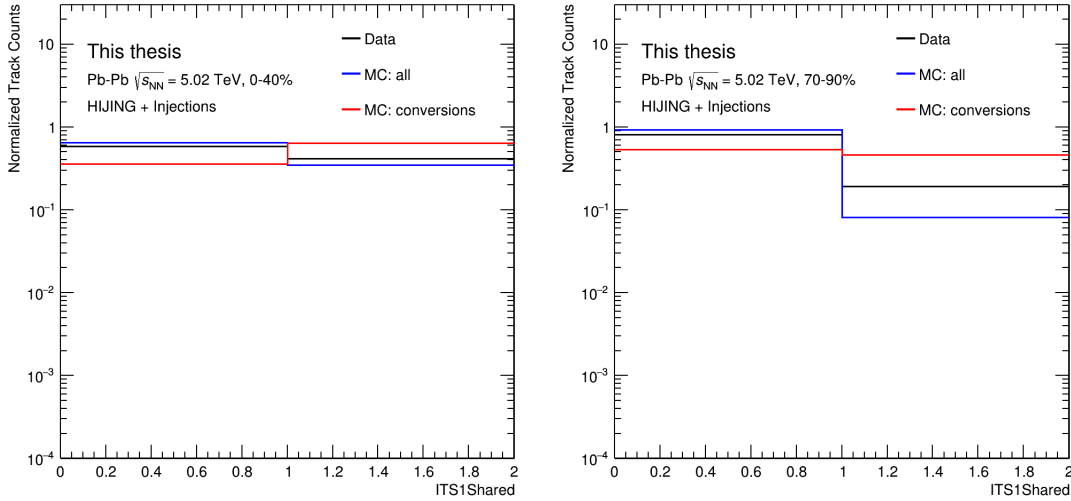


Figure 5.7.: Distribution of the shared ITS cluster variable for the first ITS layer. A value of 1 (0) indicates that the cluster in this ITS layer is (not) shared with another track. The distribution is shown for data and MC in both centrality classes.

Separate classifiers are trained for the two different centrality classes 0–40% and 70–90%. This is necessary as the ideal decision boundary is expected to depend on the track multiplicity in the event. For example, the shared ITS cluster variables, which encode whether the cluster in a given ITS layer is shared, are more

often true for clusters of conversion tracks than for non-conversion tracks. This is because the production vertex for both conversion tracks is located close to or inside the ITS layers (see Fig. 5.5). In addition, there is a dependence on the event centrality. In central collisions the chance for a randomly selected track to have a shared cluster with an uncorrelated track is higher than in peripheral collisions (see blue and black lines in Fig. 5.7) because there is a higher track density. Training the classifier on the whole 0–90% centrality range at once and including the centrality variable would in principle allow the classifier to learn such centrality dependences. However, since the data set is statistically dominated by the 0–40% centrality range (see Table 5.3) the characteristics of the 70–90% centrality class may not be learned properly. For this reason separate classifiers are trained for each centrality class.

The number of trees and the maximum depth are parameters that control the classifier’s capacity, i.e. its ability to learn complicated decision boundaries from the data. Having a large capacity, however, enhances the computation time required for training and makes the classifier more prone to overtraining. Figure 5.8 shows Receiver Operator Characteristics (ROC) curves for various choices of depth and tree numbers. The x-axis shows the signal efficiency, i.e. the fraction of signal tracks that pass an MVA cut, that is the selection criterion for a track to have an MVA output value larger than a given cut value. The background rejection, i.e. the fraction of background tracks that are rejected by this MVA cut, is shown on the y-axis. These quantities describe the classification performance achievable with a given classifier and MVA cut. Depending on the choice for the cut value on the MVA output in $[-1, 1]$, the signal efficiency is varied in $[0, 1]$. The curves in Fig. 5.8 indicate the background rejection corresponding to a selected signal efficiency. The better the classifier, the higher its background rejection for a given signal efficiency is. In Fig. 5.8 several BDTs are compared for different choices of parameters on the training data set in 0–40% and 70–90%. The performance saturates as larger BDTs are used, i.e. increasing the tree depth (first number after “BDTG” in the legend) and the number of trees (second number) beyond a certain point does not lead to improved performance. Only the very simple trees with maximum depth 5 and a single tree (black) show notably worse performance. In both centrality classes the classifiers with a maximum depth of 15 and 400 trees are used for the analyses.

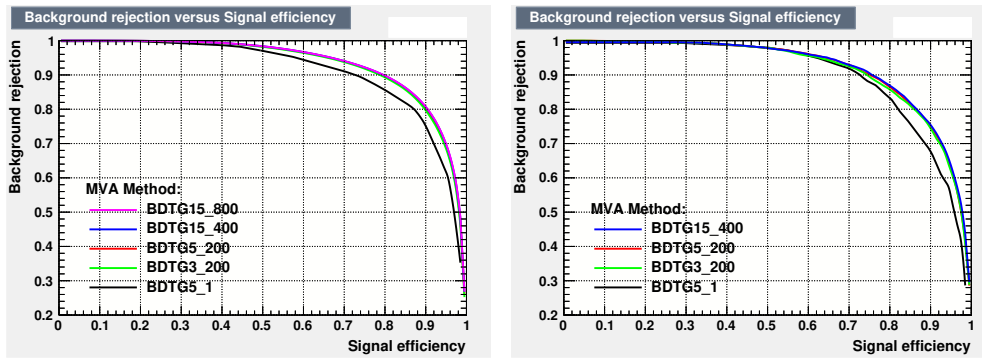


Figure 5.8.: ROC curves for Boosted Decision Trees with Gradient boosting (BDTGs) on the data sets for 0–40% centrality (left) and 70–90% (right) [116]. The first number after “BDTG” indicates the maximum tree depth and the second the number of trees.

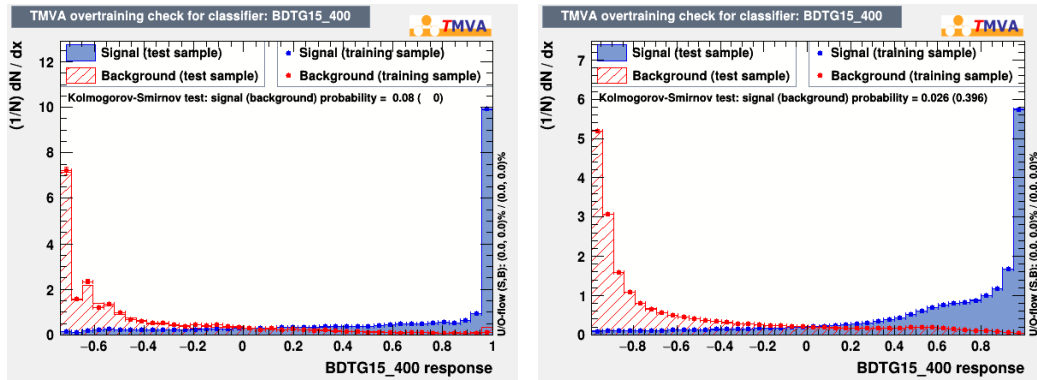


Figure 5.9.: MVA output distributions for signal (blue) and background (red) tracks in the training (dots) and test (shaded) data set for BDTs trained on the 0–40% centrality (left) and 70–90% centrality (right) data sets.

As Fig. 5.9 shows, the classifier output distributions on the training and test data sets exhibit no significant difference and thus do not indicate overtraining.

Once the classifiers are trained on the MC data sets, they are applied to real data tracks, returning an MVA output value on which a cut is placed to reject conversions tracks.

To illustrate the effect of the MVA cut on the MC data set and the real data set, Fig. 5.10 shows the distribution of tracks in the $p_{T,e}$ -divided transverse DCA and $p_{T,e}$ plane in the centrality class of 70–90%. Dividing DCA_{xy} by $p_{T,e}$ improves

the visibility of the effect of the MVA cut. In the MC data set the signal (top left) distribution is broader along both axes than the background distribution (top right). The total MC data set without any cut (middle left) is almost identical to the signal distribution, except for the top left region of the distribution, i.e. at low $p_{T,e}$ and large $p_{T,e}$ -divided DCA_{xy} . Here the conversion component becomes visible. For the analysis a typical MVA cut is placed at -0.2. As the middle right panel in Fig. 5.10 shows, this cut primarily rejects tracks in the region which is dominated by conversion tracks. The bottom panels compare the distributions of tracks in the real data set before (left) and after (right) the MVA cut. These distributions are different from the MC data set (compare to middle left and middle right panel) due to the artificial enhancement of signal tracks. Nevertheless, the background component presumably associated to conversion tracks is visible in the top left region of the bottom left panel. In this region the MVA cut has the strongest effect (see bottom right panel in Fig. 5.10).

To study the impact of the selected MVA cut, 10 cut values ranging from -1 to 0.8 in steps of 0.2 in the MVA output are enumerated by the integer $i \in [0..10]$. For example MVA 4 corresponds to the MVA cut value $-1 + 4 \cdot 0.2 = -0.2$.

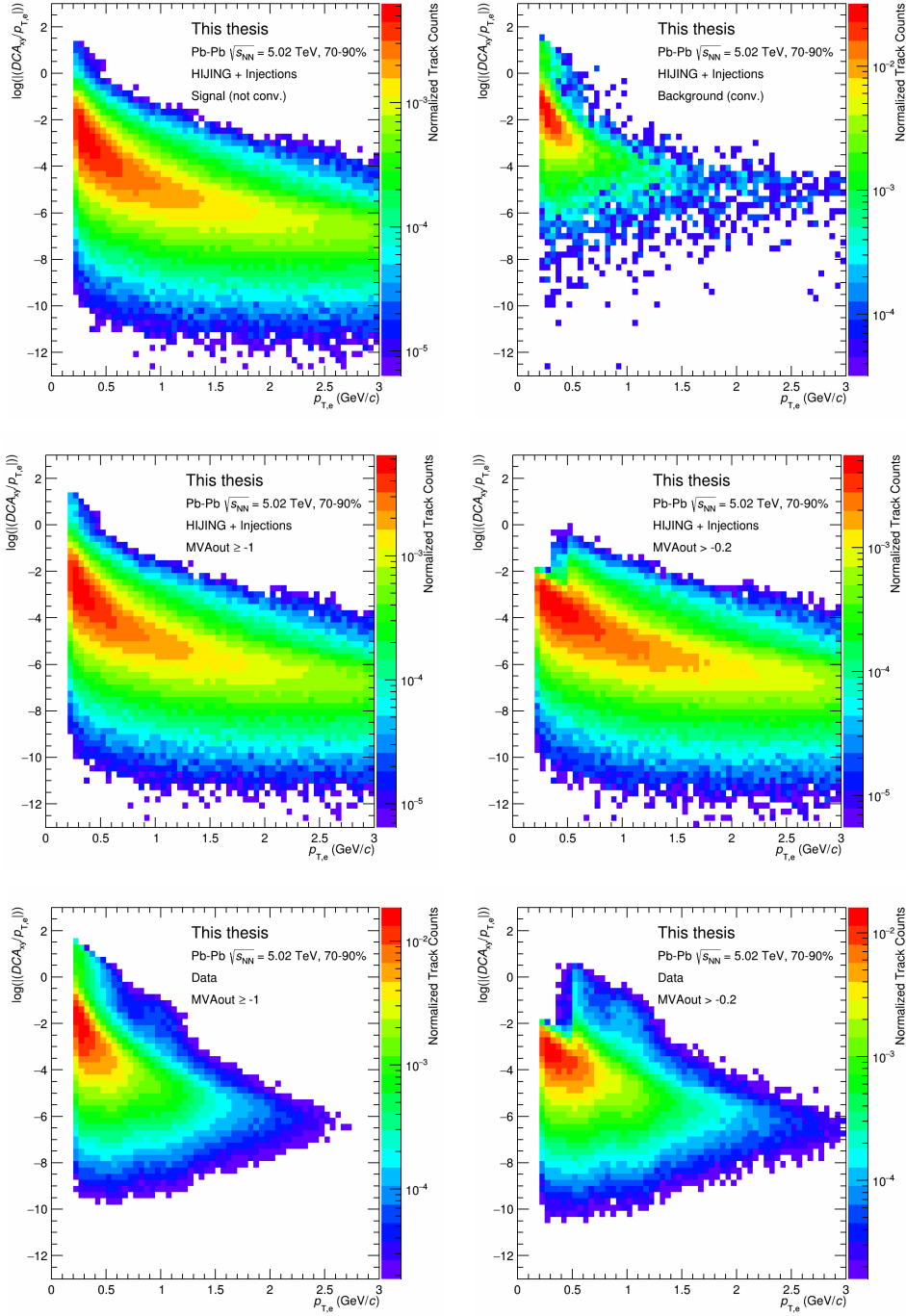


Figure 5.10.: Distributions of tracks in the $p_{T,e}$ -divided transverse DCA and $p_{T,e}$ plane. The top row shows the simulated signal (left) and background (right) tracks. The bottom row shows all simulated tracks (left) and tracks after an MVA cut at 0.2 (right). The corresponding distributions for real data are shown in the bottom row. Preselection cut 0 is used for these plots.

5.5. Pair analysis

The following section describes the analysis steps for extracting dielectron $p_{T,ee}$ spectra. The analysis is carried out for the centrality range 0–40% and 70–90% and the mass ranges $0.5 - 2.7 \text{ GeV}/c^2$ and $1.1 - 2.7 \text{ GeV}/c^2$. It focuses primarily on $p_{T,ee} < 1 \text{ GeV}/c$, where dielectron photo-production is expected to be most significant. Aspects that are specific to one centrality class individually are addressed in the corresponding dedicated sections (Section 5.8 for 70–90% and Section 5.9 for 0–40%).

In the analysis of e^+e^- pairs the goal is to infer distributions like m_{ee} and $p_{T,ee}$, which can be related to a variety of physics questions, as outlined in Section 3.2 and Section 3.3. Unless stated otherwise, data processing steps described in the following are performed in two-dimensional histograms of dielectrons in m_{ee} and $p_{T,ee}$ with the following binning:

$$m_{ee} \text{ (GeV}/c^2) = \{0.0, 0.1, 0.4, 0.5, 0.6, 0.7, 1.1, 1.5, 2.0, 2.7, 3.1, 5.0\},$$

$$p_{T,ee} \text{ (GeV}/c) = \{0.0, 0.025, 0.05, 0.075, 0.1, 0.125, 0.15, 0.2, 0.3, 0.4, 0.5, 0.6, 1,$$

steps of $0.5 \text{ GeV}/c$ up to $8.0 \text{ GeV}/c\}$.

The pair variables m_{ee} and $p_{T,ee}$ are only meaningful in the analysis context if the two tracks of the pair are correlated due to their common microscopic production process. Thus, for combinatorial background these quantities do not allow drawing conclusions on the origin of the pair.

To calculate the pair observables tracks of unlike charge sign (i.e. electrons and positrons), which are associated to the same event, are paired to dielectrons. This set of dielectrons (US) encompasses all unlike-sign signal and background dielectrons shown in Fig. 5.3. For an individual dielectron it is not possible to exclude the possibility that it is combinatorial. Nevertheless, the distribution of the combinatorial background can be estimated and statistically subtracted from US . This method is referred to as the like-sign subtraction method [18, 117]. An estimation of the combinatorial background is obtained by the like-sign (LS) dielectrons which are obtained from two positrons (LS_{++}) or electrons (LS_{--}) in the same event. Figure 5.3 illustrates an example for this concept. It shows three correlated dielectrons. One pair of electron and positron tracks originates from the same hadron decay (Same Mother non Conversion), one is produced in the same photon-conversion process (Same Mother Conversion), and one pair which results from the decay of correlated heavy-flavour hadrons (Correlated Heavy-Flavour). All other possible pairs of unlike-sign dielectrons are combinatorial. A combinatorial unlike-sign pair can, for example, be constructed with the electron of the hadron decay (“h” in Fig. 5.3) and the positron of the conversion. A further com-

binatorial unlike-sign pair can be constructed from these processes by inverting the charge signs. Similarly, two like-sign pairs can be constructed from these processes. In this way a like-sign pair can be constructed for each combinatorial unlike-sign pair². This is, however, not possible for the correlated unlike-sign pairs in Fig. 5.3. For these pairs no corresponding like-sign pair can be formed. Therefore, the total number of pairs and their correlation (which can be assumed to be none in this idealised example) is the same for like-signs pairs and combinatorial unlike-sign pairs.

Most, but not all, like-sign pairs are truly uncorrelated. Processes that produce correlated like-sign pairs are, for instance, double Dalitz decays of the neutral pions: $\pi^0 \rightarrow \gamma^* + \gamma^* \rightarrow e^+e^- + e^+e^-$. Similarly, correlated like-sign pairs are produced in decays of hadrons in correlated jets. These correlations of like-sign pairs are present for combinatorial unlike-sign pairs as well. Consequently, when subtracting the distribution of LS in some observable like $p_{T,ee}$, these correlations are also removed from the corresponding distribution of US . The remaining correlations in the US distributions are ideally related to one of the signal processes in Fig. 5.3. This assumption is tested in Section 5.11.3.

In conclusion, LS can be used to statistically subtract the combinatorial component of US to extract the unlike-sign signal US_{Sig} :

$$US_{\text{Sig}} = US - R \cdot LS, \quad (5.2)$$

where R is a correction factor that accounts for the different geometrical acceptance for like-sign and unlike-sign pairs. In this analysis the definition of LS depends on the number of LS_{++} and LS_{--} pairs in the event:

$$\begin{aligned}
 &\text{if } LS_{++} > 0 \text{ and } LS_{--} > 0 : LS = 2 \cdot \sqrt{LS_{++} \cdot LS_{--}}, \\
 &\text{else : } LS = LS_{++} + LS_{--}.
 \end{aligned} \quad (5.3)$$

The geometric mean (first line) is more robust with respect to asymmetries in the number of electrons and positrons than the arithmetic mean (second line). It is, however, problematic in cases where either LS_{++} or LS_{--} are zero, as it would yield zero as the estimation of the combinatorial background. To mitigate this problem, in these cases the arithmetic sum of LS_{++} and LS_{--} is used instead. Cross-checks using either the arithmetic, geometric or the combination of both methods show that the in the present analysis these differences are negligible.

Inhomogeneities in the detector acceptance, like e.g. dead zones, affect electron and positron tracks differently since these tracks have opposite curvature due to

²A more detailed mathematical analysis of the like-sign subtraction method is provided in [18].

the magnetic field of the detector. This effect is only caused by the acceptance and is not related to correlations due to microscopic processes in the event. For this reason it can be estimated using entirely uncorrelated pairs which are obtained by the method of event-mixing. Here tracks of two different events are paired and form the event-mixed unlike-sign pairs US_{mix} and event-mixed like-sign pairs LS_{mix} . The latter is defined again according to Eq. (5.3). Using these event-mixed pairs the R-factor is defined as:

$$R = \frac{US_{\text{mix}}}{LS_{\text{mix}}}. \quad (5.4)$$

Apart from microscopic correlations, there can be global event features that lead to spurious correlations between tracks. These can be related to the event centrality ($cent$) and the position of vertex along the z -axis (z_{Vertex}). To reproduce these global event correlations correctly pairs are divided in pools of different event classes. Events are only mixed if the two events (denoted by the subscripts 1 and 2) fulfill these criteria:

- $z_{\text{Vertex},1}$ and $z_{\text{Vertex},2}$ in the same interval in $[-10,-5,0,5,10]$ cm
- $cent_1$ and $cent_2$ in the same interval in $[0,5,10,20,30,50,80]$ centrality per-centiles.

Figure 5.11 shows the R-factor dependence on m_{ee} in various $p_{T,ee}$ regions for both centrality classes. For the peripheral centrality range 70–90% the deviation of the R-factor from unity is not statistically significant and thus the R-factor is not applied in this centrality range. In 0–40% centrality the R-factor deviates significantly from unity and has an impact on the result (see Fig. 5.29). Therefore, the R-factor is applied in the range of 0–40% centrality.

5.5.1. Benchmark for BDT based conversion rejection

To assess the performance of the machine learning based conversion rejection, a comparison to an analysis with conventional conversion rejection is carried out. So far conversions were rejected by selection cuts on the track variables. A typical set of cuts to achieve this is:

- number of ITS clusters: $n_{\text{Cls}}^{\text{ITS}} > 4$

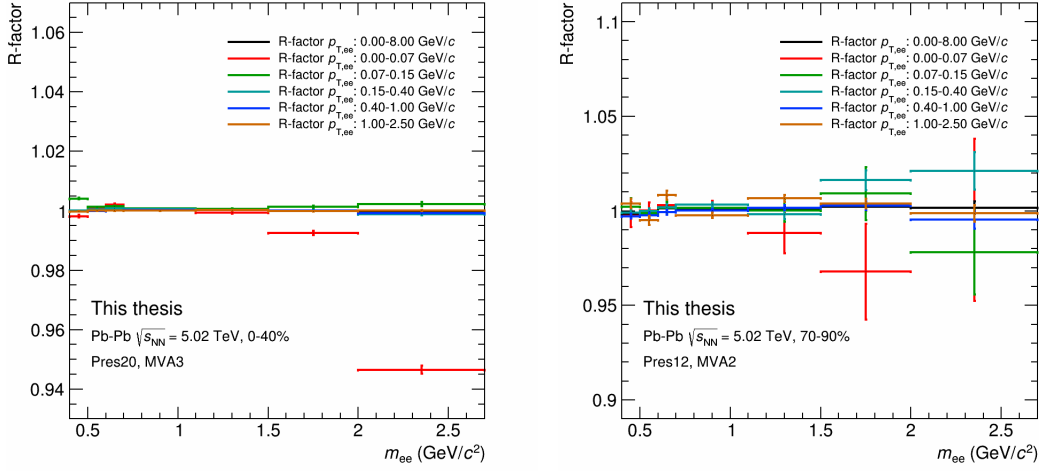


Figure 5.11.: The R-factor dependence on m_{ee} for various $p_{T,ee}$ regions in 0–40% (left) and 70–90% centrality (right).

- $\chi_{ITS}^2/n_{Cls}^{ITS} < 5$
- $\chi_{TPC}^2/n_{Cls}^{TPC} < 4$
- no shared ITS cluster or exactly one shared ITS cluster which is not in the first ITS layer
- a hit in the first ITS layer.

Instead of these cuts the machine learning based conversion rejection is used in the multivariate analysis. In this comparison a different classifier to the one discussed in Section 5.4.3 is used. In this study a neural-network (see [115]) is used as classifier. It is trained using the TensorFlow library [118] to reject conversion tracks as described in Section 5.4.3. In addition to efficient conversion track identification, the similarity between the MVA output distribution in MC and real data is used as an objective during training. This was implemented using the methods described in [119, 120] and should prevent the classifier from learning characteristics of conversions that are not present in real data. Such issues could arise from imperfections in the MC simulation. This method can also avoid systematic uncertainties, that can result from such discrepancies in the MC data and real data [121]. After this study it was found that this rather involved training procedure does not lead to a benefit in this analysis, since the dominant uncertainties are not systematic but statistical. Therefore, the neural network was subsequently

replaced by the BDTs described in Section 5.4.3, which is easier to implement in the ROOT analysis framework [122], that is used in the analysis of ALICE data. The BDTs achieve the same conversion classification performance as the neural network used in this comparison.

All other cuts for event and track selection in both analyses are identical with the event cuts in Section 5.2, the standard track cut in Section 5.4.1 and the preselection cut 0 (see Section 5.4.2). For the cut on the ratio of findable clusters over crossed rows in the TPC the range [0.95,1.05] is used instead of [0.8,1.05]. This is a minor difference that plays no role for this comparison.

The comparison between the cut-based conversion rejection and the MVA-based one (see Section 5.4.3) is carried out in the centrality range of 0–90%. Choosing a large centrality range enhances the available amount of data for the comparison. The figure of merit in this comparison is the statistical significance z of the signal, which is defined by:

$$z = \frac{US_{Sig}}{\sigma_{Sig}}, \quad (5.5)$$

$$\sigma_{Sig} = \sqrt{US + R^2 \cdot LS}, \quad (5.6)$$

where σ_{Sig} is the statistical uncertainty of the signal. The statistical uncertainty of R is taken to be zero, as practically infinite amounts of data from event mixing can be generated. An advantage of using σ_{Sig} as a figure of merit is that it is data driven, i.e. it does not rely on a simulation. Values of z are compared in $p_{T,ee}$ -integrated mass spectra. No efficiency correction is applied to the results. Figure 5.12 shows the comparison of the statistical significance z for the machine learning (MVA) based approach and the conventional cut-based approach for two mass ranges. In the lower mass range (left) the MVA approach yields an enhancement of 10–50%. At higher masses (right) the MVA approach results in marginally, but consistently higher z than the cut-based conversion rejection. In the m_{ee} -bin around 2 GeV/ c^2 the cut-based analysis yields a negative signal due to over-subtraction, i.e. a negative bin content in US_{Sig} caused by statistical fluctuations in the like-sign subtraction.

5.5.2. Efficiency correction

As pointed out in Section 5.1 the raw (i.e. before efficiency correction) unlike-sign dielectron signal US_{Sig} cannot be compared directly to theory calculations or other experimental results due to the rejection of signal dielectrons when applying the analysis specific selection cuts. To compensate for this, the raw signal yield is cor-

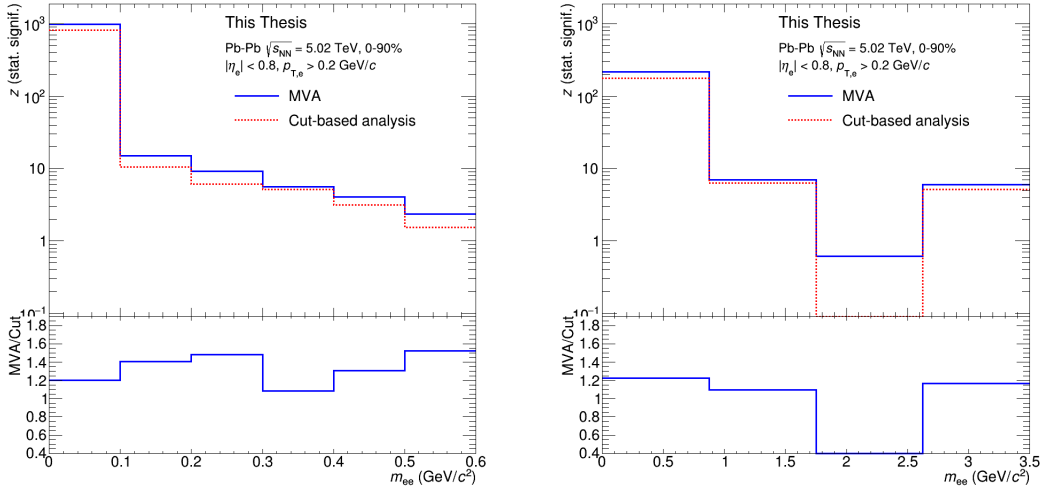


Figure 5.12.: Comparisons of the statistical significance z of the uncorrected signal for machine learning based conversion rejection (MVA) and the cut-based analysis in two different mass ranges.

rected using the estimated efficiency of the signal. The efficiency can be estimated from MC simulations, which provide information on the total number of generated signal dielectrons and reconstructed signal dielectrons, i.e. signal dielectrons which pass all selection cuts.

In this analysis the efficiency of the MVA cut is treated separately from the efficiencies of the other cut selections. This allows studies of possible source dependences of this efficiency. The underlying reason for this could be that heavy-flavour decays take place at slightly displaced vertices (D mesons: $c\tau \approx 150 \mu\text{m}$, B mesons: $c\tau \approx 470 \mu\text{m}$) and thus are reconstructed with DCA_{xy} values that are between the typical values for dielectrons from light-flavour decays and photon-conversions (see Fig. 5.5). Consequently, the efficiency of dielectrons in the analysis could depend on the relative fraction of light- and heavy-flavour dielectrons, which is not known a priori. To study if these issues are present in this analysis the MVA efficiency is studied for various dielectron sources separately on the MC data.

The signal dielectron efficiency for the data selection steps shown in Fig. 5.1 is split into two efficiencies, one for all steps before the BDT track selection (ϵ_{Elec}), and a separate one for the BDT track selection (ϵ_{MVA}). The efficiencies are defined

by:

$$\begin{aligned}
\epsilon_{\text{Elec}} &= \frac{US_{\text{Sig}}^{\text{preMVA}}}{US_{\text{Sig}}^{\text{Gen}}}, \\
\epsilon_{\text{MVA}} &= \frac{US_{\text{Sig}}^{\text{Rec}}}{US_{\text{Sig}}^{\text{preMVA}}}, \\
\epsilon_{\text{Tot}} &= \epsilon_{\text{Elec}} \cdot \epsilon_{\text{MVA}},
\end{aligned} \tag{5.7}$$

where $US_{\text{Sig}}^{\text{Gen}}$ denotes the number of generated signal dielectrons, $US_{\text{Sig}}^{\text{preMVA}}$ the number of signal dielectrons that are reconstructed and pass all cuts before the MVA cut, $US_{\text{Sig}}^{\text{Rec}}$ the number of signal dielectrons after the MVA cut, and ϵ_{Tot} the combined total efficiency. In the MC data set the originally generated track kinematic variables $p_{\text{T},e}$, η_e and φ_e are modified to account for detector and reconstruction effects. This is necessary since the kinematics of the reconstructed track does not, in general, represent the one of the originally generated track. Reasons for this are bremsstrahlung, multiple-Coulomb scattering and finite detector resolution. In general, the measured values are distributed around the real value with a width that represents the resolution. These effects can be studied and parametrised on MC data. This allows a transformation of the generated kinematic variables into the measurable ones, i.e. the values of the variables which would typically be measured for a certain generated particle. This procedure is called smearing. It is also applied when comparing results to theory expectations, which also need to take these effects into account (see Section 5.6 and Section 5.7 for details).

Since there is less MC data available for the MVA correction, a coarser binning is used for the MVA efficiency histograms in the high- $p_{\text{T},ee}$ region (for ϵ_{Elec} the binning defined in Section 5.5 is used):

$$\begin{aligned}
m_{ee} \text{ (GeV}/c^2\text{)} &= \{0.0, 0.1, 0.4, 0.5, 0.6, 0.7, 1.1, 1.5, 2.0, 2.7, 3.1, 4.0, 5.0\}, \\
p_{\text{T},ee} \text{ (GeV}/c\text{)} &= \{0.0, 0.05, 0.1, 0.15, 0.3, 0.5, 1, 5.0, 8.0\}.
\end{aligned}$$

5.6. Hadronic cocktail

The corrected results of dielectron analyses are typically compared to expectations based on known hadronic sources of dielectrons. The comparison is carried out between measured and expected dielectrons in the acceptance of the central-barrel detectors of ALICE (see Fig. 4.1): $|\eta_e| < 0.8$ and $p_{\text{T},e} > 0.2$ GeV/ c . The expect-

tations are based on measurements and models of dielectron sources. They do not account for effects like, e.g. thermal radiation, photo-production or modified meson spectra. Therefore, the cocktail can be regarded as the expectation in the scenario where these effects are absent.

The following mesons containing light-flavour (LF) quarks (u,d,s) are considered as dielectron sources: $\pi^0, \eta, \eta', \omega, \rho^0, \phi$. The p_T distribution of generated particles for all mesons except the η are based on a parametrisation of π^\pm spectra measured by ALICE in Pb–Pb collisions at $\sqrt{s_{NN}} = 5.02$ TeV [123]. Based on these measurements, the p_T spectra of the other mesons can be inferred using the assumption of m_T -scaling. It states that for hadrons produced in pp collisions the spectra of transverse mass $m_T = \sqrt{m_0^2 + (p_T/c)^2}$ exhibit a shape universality [2]. This allows approximation of the shape of the p_T spectra for the aforementioned group of mesons using measurements of p_T spectra of π^\pm [2, 117]. Based on measurements of ρ^0 (so far an unpublished ALICE measurement), ω [124] and ϕ [125] production, the corresponding relative abundances with respect to pions are extracted. Since these measurements do not cover the low- p_T regions relevant in this analysis, they cannot provide input for the shape of the spectra in that region directly, but require the aforementioned extrapolations using m_T -scaling. The abundance of the η' is taken from PYTHIA 6 [112] simulations as no suitable measurements are available. Their shape is determined as well via m_T -scaling. The spectrum of the η meson is taken from measured K^\pm/π^\pm ratios [123]. The underlying assumption is that the K^\pm/π^\pm and η/π^\pm ratios are similar, since the K^\pm and η mesons have similar masses and the same quantum numbers in terms of angular momentum J and parity P . The K^\pm/π^\pm ratios are used together with the aforementioned parametrisation of the π^\pm spectrum to calculate the expected η spectrum.

The LF mesons are produced according to the abundances and p_T distributions described above and with a uniform distribution in the rapidity range of $|y| < 1.2$. The decay of the mesons is handled by the EXODUS [126] particle decayer. This allows incorporating experimental input on decay kinematics. For Dalitz decays the mass spectrum is based on the Kroll-Wada equation [45]. In addition, electromagnetic form factors according to measurements by the NA60 collaboration are used [127]. These measurements also provide the line shape of the ρ meson mass spectrum which is used in the cocktail. The two-body decays of the ω and ϕ mesons are simulated according to the Gounaris-Sakurai equation [128].

The following decay channels are considered in the LF cocktail, with branching ratios to dielectrons according to the Particle Data Group [87]:

- $\pi^0 \rightarrow e^+e^-\gamma$
- $\eta \rightarrow e^+e^-\gamma$

- $\rho^0 \rightarrow e^+e^-$
- $\omega \rightarrow e^+e^-$ and $\omega \rightarrow e^+e^-\pi^0$
- $\eta' \rightarrow e^+e^-\gamma$ and $\eta' \rightarrow e^+e^-\omega$
- $\phi \rightarrow e^+e^-$, $\phi \rightarrow e^+e^-\pi^0$ and $\phi \rightarrow e^+e^-\eta$.

As pointed out in Section 5.3 heavy-flavour (HF) quark (c, \bar{c}, b, \bar{b}) production also contributes to the dielectron signal. These contributions are estimated with binary scaled $c\bar{c}$ and $b\bar{b}$ production cross sections ($\sigma_{c\bar{c}, b\bar{b}}$) that were derived in analyses of pp collisions. The binary scaling factor N_{coll} accounts for the average number of binary nucleon-nucleon collisions in a HIC of a certain centrality. This number is obtained from Glauber MC simulations (see Section 3.1). The rapidity-differential charm production cross section is obtained by extrapolating an ALICE measurement in pp collisions at $\sqrt{s} = 7$ TeV [129] to $\sqrt{s} = 5.02$ TeV. For this the measurement result $d\sigma_{c\bar{c}}/dy|_{y=0} = 0.954 \pm 0.119$ mb is scaled by a factor 0.83, which is obtained via “fixed-order + next-to-leading log” (FONLL) calculations [130]. Similarly, the measured beauty production cross section is obtained from an extrapolation of LHCb measurements in pp collisions at $\sqrt{s} = 7$ TeV [131] to $\sqrt{s} = 5.02$ TeV. This corresponds to scaling the measured value of $\sigma_{b\bar{b}} = 0.204^{+0.035}_{-0.034}$ mb with the FONLL factor 0.71.

Particle	BR	m_{Γ}	N_{coll}	Cross section	Fit	Parametrisation
π^0	2.98	0	0	0	0	8
η	5.8	-15, +6	0	0	0	8
η'	6.38	20	0	0	0	8
ω	1.92	20	0	0	0	8
ρ^0	1.11	20	0	0	0	8
ϕ	1.02	30	0	0	0	8
J/ψ	0.54	0	0	0	30	0
c, \bar{c}	24	0	1/2.6	12.5	0	0
b, \bar{b}	10	0	1/2.6	16.7	0	0

Table 5.4.: Relative systematic uncertainties for the hadronic cocktail in percent values.

Production kinematics, hadronisation and subsequent hadron decays are simulated using the PYTHIA 6 event generator (Perugia 2011 tune) [112]. The heavy-flavour quarks are produced in a rapidity range of $|y| < 1.2$. To enhance the computational efficiency of the simulation at least one $c\bar{c}$ pair is required per simulated event. After hadronisation this pair is forced to decay semi-leptonically into a cor-

related dielectron pair. The simulated dielectron yield from $c\bar{c}$ pairs is then scaled with the measured branching ratio of $c \rightarrow e^+ = 0.096 \pm 0.004$ according to [87]. The cocktail contribution from $b\bar{b}$ is simulated without enforcing the decay to an electron final-state. This avoids complicated book keeping of the large number of possible decay chains of beauty hadrons into electron final states.

The final contribution to the cocktail is from J/ψ decays. Here a preliminary result by ALICE serves as input for a fit of the p_T spectrum [132].

The produced electron and positron tracks corresponding to all discussed sources are modified as described in Section 5.5.2 to mimic detector effects. Finally, the spectra in $p_{T,ee}$ and m_{ee} are extracted with the single track requirements $p_{T,e} > 0.2$ GeV/ c and $|\eta_e| < 0.8$.

Systematic uncertainties are assigned to the hadronic cocktail according to Table 5.4. For the LF mesons the uncertainties are coming from literature values of the branching ratios (BR) and the m_T -scaling factors (except for π^0) and uncertainties in the input parametrisations of p_T spectra of π^\pm [110]. The parametrisation uncertainty is obtained by variations of the fitting procedure for the π^\pm spectrum, which underlies the LF mesons. As mentioned above, the η contribution is not obtained from m_T -scaling but from the measured K^\pm spectrum. The associated uncertainty is obtained by the deviation between the K^\pm spectrum and the η spectrum from m_T -scaling. The deviations of these spectra allow the estimation of the m_T -scaling uncertainty of the η meson in Table 5.4. The uncertainty of the fit of the J/ψ spectrum is estimated to be 30%. Uncertainties for the HF contributions are given by the uncertainties associated to the branching ratios, the binary collision scaling factor N_{coll} and the heavy-quark production cross sections. An uncertainty for the FONLL scaling factors is to be included in the future, but is expected to be small compared to the aforementioned uncertainties [110].

Figure 5.13 and Fig. 5.14 show the m_{ee} and $p_{T,ee}$ spectra of the cocktails for 0–40% and 70–90% centrality. The $p_{T,ee}$ spectra (right) are shown in the m_{ee} interval of 0.5 – 2.7 GeV/ c^2 , which represents one of the ranges studied in this analysis. This mass range is dominated by HF contributions but LF contributions are non-negligible. In 1.1 – 2.7 GeV/ c^2 the LF contributions can be practically neglected.

5.7. Model calculations

In addition to the cocktail, the data are compared to models of photo-production and thermal radiation. The latter is provided by Rapp et al. [133]. It describes thermal dielectron emission of the fireball with a realistic space-time evolution in

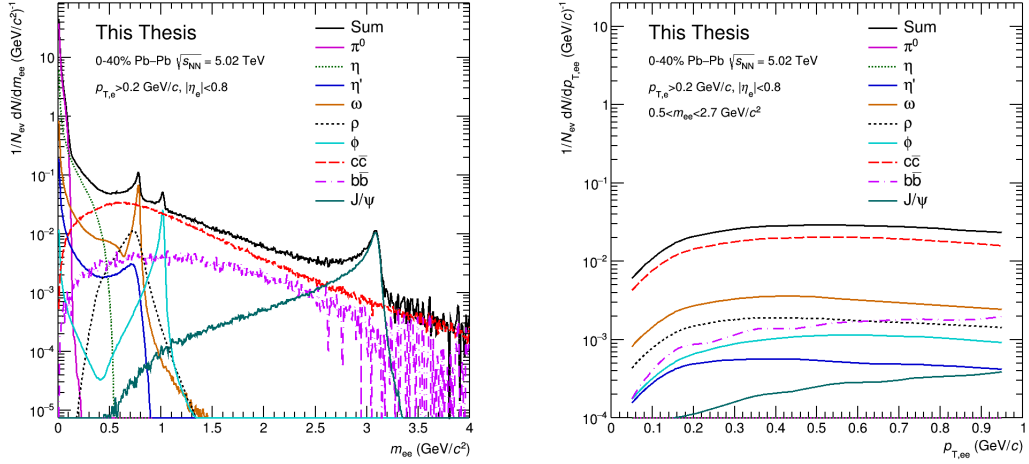


Figure 5.13.: Spectra in m_{ee} and $p_{T,ee}$ of the hadronic cocktail in 0–40% centrality. The $p_{T,ee}$ spectrum (right) is shown in the m_{ee} interval of 0.5 – 2.7 GeV/c^2 .

the QGP and hadron gas phase. The equation of state incorporates a cross-over transition at $T_c = 170$ MeV and a hadro-chemical freeze-out at $T_{\text{chem}} = 160$ MeV. Klusek-Gawenda et al. provide photo-production calculations for the mass range of 1.1 – 2.7 GeV/c^2 [134]. These calculations are based on EPA and a Woods-Saxon nuclear form factor as discussed in Section 3.3.2.

Two additional photo-production calculations are provided by Zhangbu et al. [135]. For one calculation they use the gEPA approach, which is described in Section 3.3.2. The second calculation is a full leading order QED calculation [135]. For the models of photo-production and thermal radiation detector effects and the resolution are not implemented, as these calculations were carried out by the authors of the corresponding models, which do not have access to the ALICE simulation framework. This short coming will be overcome in future studies. For the time being, the impact of the detector effects and reconstruction resolution is estimated. In contrast to the thermal radiation spectra (see Fig. 5.24), the photo-production spectra show a sharp peak at low- $p_{T,ee}$ and are thus particularly sensitive to the $p_{T,ee}$ resolution. To estimate the effective $p_{T,ee}$ resolution a STARlight [136] MC production is used. It contains the reconstructed track information of simulated photo-produced dielectrons after their passage through the detector and reconstruction. In addition, the information of the generated dielectron kinematics is available. This MC simulation only contains dielectrons for $m_{ee} > 1.5$ GeV/c^2 . However, low- $p_{T,ee}$ dielectrons are most sensitive to the $p_{T,ee}$ resolution. At low- $p_{T,ee}$ lower masses imply lower $p_{T,ee}$, which results in a better

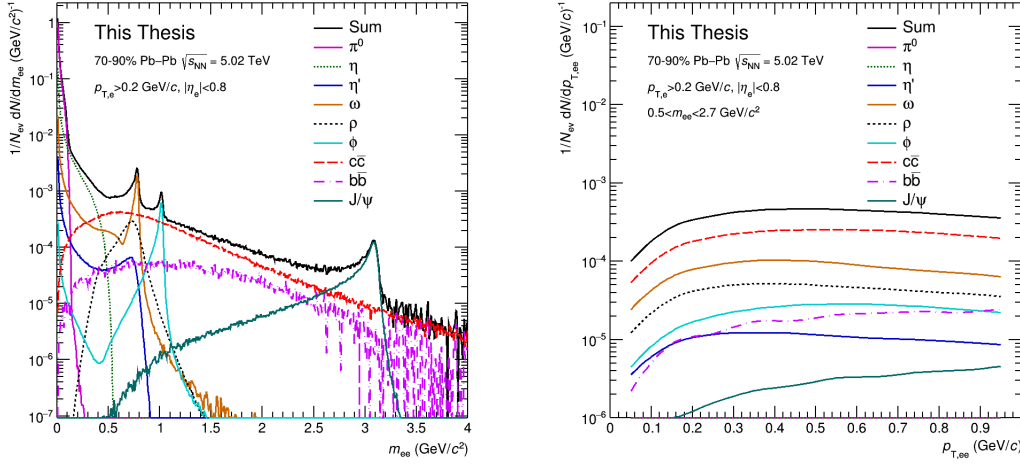


Figure 5.14.: Spectra in m_{ee} and $p_{T,ee}$ of the hadronic cocktail in 70–90% centrality. The $p_{T,ee}$ spectrum (right) is shown in the m_{ee} interval of 0.5 – 2.7 GeV/c^2 .

$p_{T,e}$ resolution. This can be seen in Fig. 5.15 (left), which shows the mean relative discrepancy between the originally generated value $p_{T,e}^{\text{gen}}$ and the reconstructed value $p_{T,e}^{\text{rec}}$. The resolution is drastically improving for $p_{T,e}^{\text{gen}} < 1 \text{ GeV}/c$. The lack of dielectrons at $m_{ee} < 1.5 \text{ GeV}/c^2$ is expected to result in a higher average $p_{T,e}$. As a consequence, it is expected that the $p_{T,ee}$ resolution is better than estimated from this simulation.

The generated ($p_{T,ee}^{\text{gen}}$) and reconstructed ($p_{T,ee}^{\text{rec}}$) $p_{T,ee}$ values for photo-produced dielectrons in STARlight with preselection 0 track cuts is shown in Fig. 5.15 (right). Using this information, the distribution of $p_{T,ee}^{\text{rec}}$ values ($P(p_{T,ee}^{\text{rec}} | p_{T,ee}^{\text{gen}})$) is obtained in the slices along the y-axis at a given $p_{T,ee}^{\text{gen}}$ value. The resolution effects can be estimated by smearing the $p_{T,ee}^{\text{gen}}$ values provided in the model calculations according to the corresponding $P(p_{T,ee}^{\text{rec}} | p_{T,ee}^{\text{gen}})$. For each $p_{T,ee}^{\text{gen}}$ -bin in the model calculations the number of entries $n(p_{T,ee}^{\text{gen}})$ is determined. Then $n(p_{T,ee}^{\text{gen}})$ samples are drawn according to $P(p_{T,ee}^{\text{rec}} | p_{T,ee}^{\text{gen}})$ using the rejection sampling technique. The resulting smeared $p_{T,ee}$ values ($p_{T,ee}^{\text{sme}}$) are filled into a histogram. This procedure is carried out for the $p_{T,ee}^{\text{gen}}$ range of 0 – 0.15 GeV/c , which produces the complete spectrum of smeared values $p_{T,ee}^{\text{sme}}$. For higher $p_{T,ee}^{\text{gen}}$ values no entries in the smearing matrix Fig. 5.15 (right) are available. Since this range covers essentially the full support of the $p_{T,ee}^{\text{gen}}$ distributions (see Fig. 5.16, right), this limitation is not problematic. It was checked that a reduced range of 0 – 0.1 GeV/c would already yield practically identical results.

A conceptual shortcoming of this smearing procedure is that it is applied to the

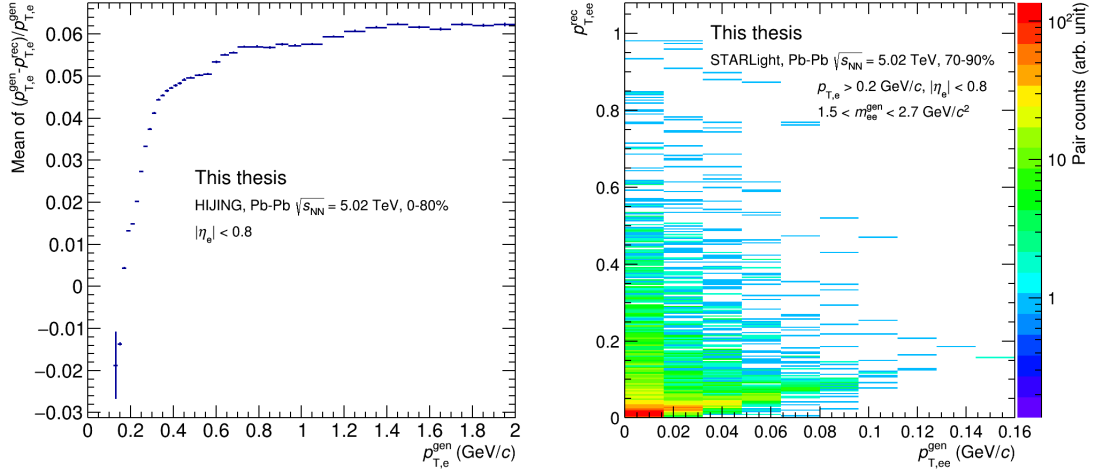


Figure 5.15.: Left: The mean of the relative discrepancy between the originally generated $p_{T,e}^{\text{gen}}$ and the reconstructed $p_{T,e}^{\text{rec}}$ from a MC simulation of electron tracks. Right: The relative discrepancy between the originally generated ($p_{T,ee}^{\text{gen}}$) and the reconstructed ($p_{T,ee}^{\text{rec}}$) $p_{T,ee}$ against $p_{T,ee}^{\text{gen}}$ in a MC simulation of dielectron photo-production using the STARlight event generator.

generated $p_{T,ee}$ after cuts on the single track η_e and $p_{T,e}$ were applied. The correct way would be, however, to apply first the smearing on the track level and to apply then the track cuts. Providing the smearing matrices to theorists, so that they can be used in the model calculations, is foreseen in future. The procedure applied here should nevertheless allow an approximation of the real resolution effects.

Figure 5.16 (left) shows a test of this smearing procedure. Smearing the originally generated STARlight spectrum (blue) results in a smeared spectrum (green) that reproduces the reconstructed spectrum (red) rather well. The smearing procedure is applied to the aforementioned model calculations of photo-production (see Fig. 5.16, right). As a result, the peaks are less sharp and the tails towards large $p_{T,ee}$ are more pronounced. The maximum value of the spectra are reduced by a factor ~ 3 for the model by Kłusek-Gawenda et al., by a factor ~ 2 for the QED calculation and a factor ~ 1.5 for the gEPA calculation.

In the mass range of $0.5 - 2.7$ GeV/c² a model calculation of photonuclear ρ and ϕ production is also included [137]. It accounts for the dielectron yield from the decays into e^+e^- of these mesons. As the corresponding yield is negligible in comparison to other contributions (see Fig. 5.24, bottom) no smearing is applied to this spectrum.

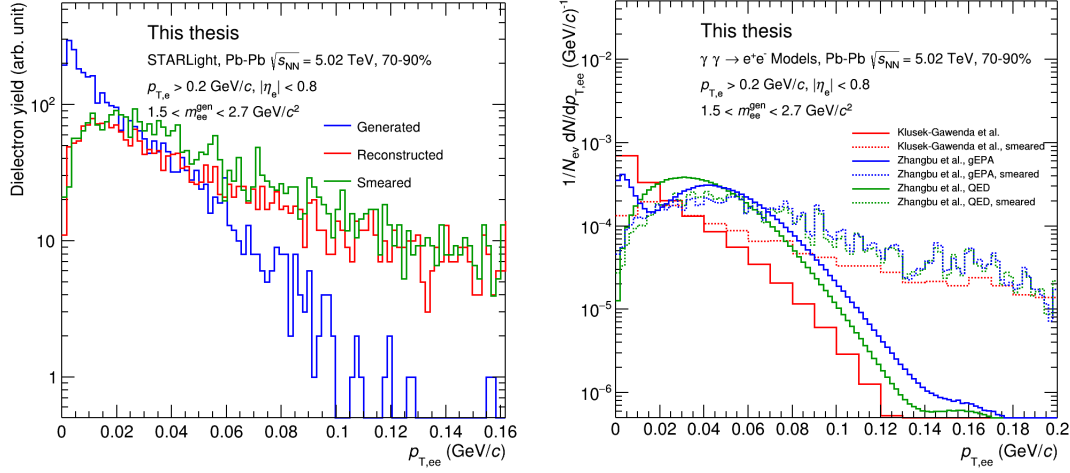


Figure 5.16.: Left: Comparison of the generated (blue), reconstructed (red) and smeared (green) photo-production spectrum by STARlight. Right: Generated (solid) and smeared (dotted) model calculations.

5.8. Dielectron $p_{T,ee}$ spectra in 70–90% centrality

This section describes details of the dielectron analysis in 70–90% centrality for the mass ranges m_{ee} : 0.5 – 2.7 GeV/ c^2 and m_{ee} : 1.1 – 2.7 GeV/ c^2 .

5.8.1. Efficiency correction

The composition of the dielectron signal in terms of the possible physical sources is not known a priori. The signal efficiency may vary for different assumptions on the physical source of the dielectron signal and thus affect the analysis procedure. For example, the efficiency for dielectrons from photo-production could differ from the one for dielectrons from correlated open heavy-flavour hadron decays. Therefore, it has to be investigated if the efficiencies ϵ_{Elec} and ϵ_{MVA} differ significantly for different signal sources. For each option all unlike-sign pairs, i.e. also all combinatorial pairs, from the MC dielectron sources listed in Table 5.5 are used for the efficiency calculation. The abbreviations used for the MC signal sources are as follows. Hij denotes the HIJING event generator [111], which contains light- and heavy-flavour dielectron sources. Since it produces dielectrons in abundances that approximately reflect the realistic yields per event, the corresponding amount of

MC Source	Name
Hij+HF+LF+J/ ψ	ALL
HF	HF
LF+J/ ψ	LF-JPSI
Hij	HIJ
Hij+HF+LF+J/ ψ	RPHFCorr
STARlight	STAR

Table 5.5.: MC data sets for which efficiencies are compared.

data is very limited. LF-JPSI corresponds to the light-flavour and J/ ψ injections, and HF to the heavy-flavour injections (see Section 5.1). The efficiency corresponding to the name RPHFCorr is obtained using all of these sources, while excluding combinatorial pairs. Thus, here only the signal pairs according to Section 5.3 are considered. Finally, also the STARlight MC data set mentioned in Section 5.7 is used to determine efficiencies. It contains only electrons from photo-production. Here also combinatorial pairs are considered.

The efficiencies of the preselection and the MVA cut are studied separately. In Fig. 5.17 and Fig. 5.19 the preselection efficiencies (left) and the MVA efficiencies (right) are shown in projections on the $p_{T,ee}$ -axis. To calculate these efficiency histograms the unlike-sign pair histograms used to calculate them (see Eq. (5.7)) are projected on the $p_{T,ee}$ -axis. The cuts for which the efficiencies are shown are the ones that are selected by the final cut selection procedure described in Section 5.8.2. This is the preselection cut 20 and MVA cut 4 for the mass range $1.1 - 2.7 \text{ GeV}/c^2$ and preselection cut 12 and MVA cut 2 for the $0.5 - 2.7 \text{ GeV}/c^2$ mass range. For $p_{T,ee}$ above $0.2 \text{ GeV}/c$ STARlight (STAR in Fig. 5.19 and Fig. 5.17) is discarded since it has essentially no dielectron signal in this region (see Fig. 5.16) and also cannot be expected to yield realistic combinatorial pairs since it only contains electron tracks from photo-production. In addition, the STARlight simulation does not include dielectrons below the mass of $1.5 \text{ GeV}/c^2$.

No significant source dependence of the efficiencies is indicated in the mass range of $1.1 - 2.7 \text{ GeV}/c^2$ (see Fig. 5.17). Figure 5.19 shows that in the mass range of $0.5 - 2.7 \text{ GeV}/c^2$ the efficiency ϵ_{Elec} for preselection 12 (left) seems to be slightly higher for the LF sources and lower for HIJING. The discrepancy is statistically not highly significant and on the order of 1%. No systematic uncertainty is assigned to this discrepancy.

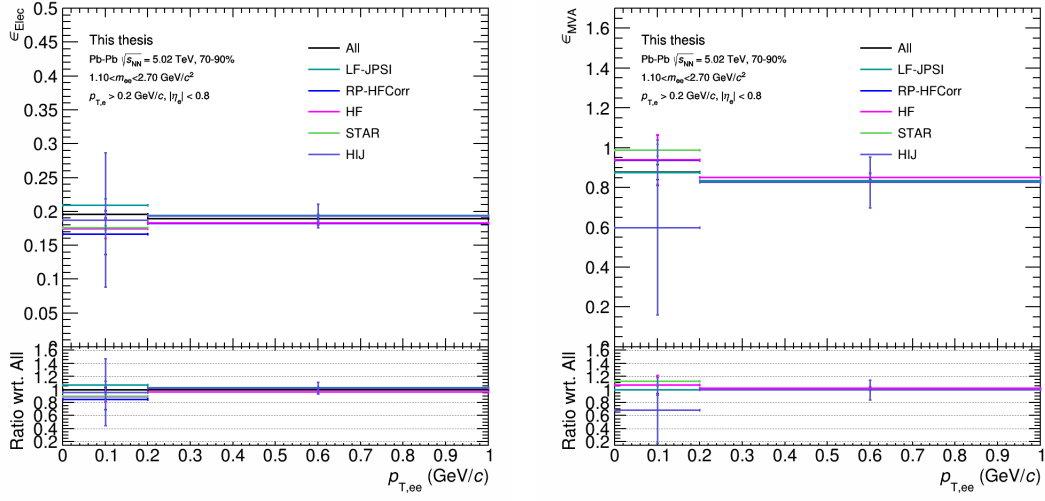


Figure 5.17.: Comparison of efficiencies for different dielectron sources in m_{ee} : 1.1 – 2.7 GeV/c². Left: Electron selection efficiency (ϵ_{Elec}) for different signal definitions with preselection cut 20 and MVA cut 0. Right: MVA efficiency (ϵ_{MVA}) for different signal definitions with preselection cut 20 and MVA cut 4.

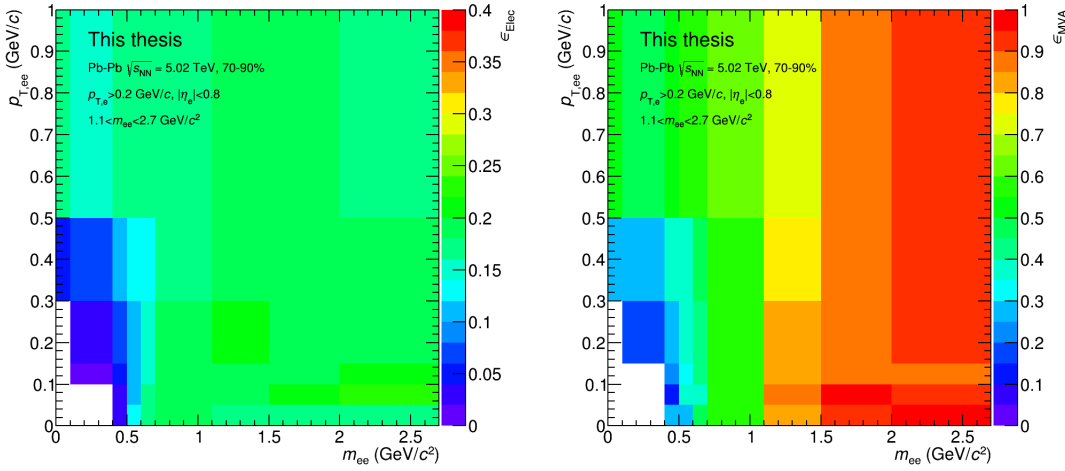


Figure 5.18.: Efficiency ϵ_{Elec} for preselection cut 20 (left) and ϵ_{MVA} for MVA cut 4 (right), which are the cuts used for the $p_{T,ee}$ spectrum in m_{ee} : 1.1 – 2.7 GeV/c².

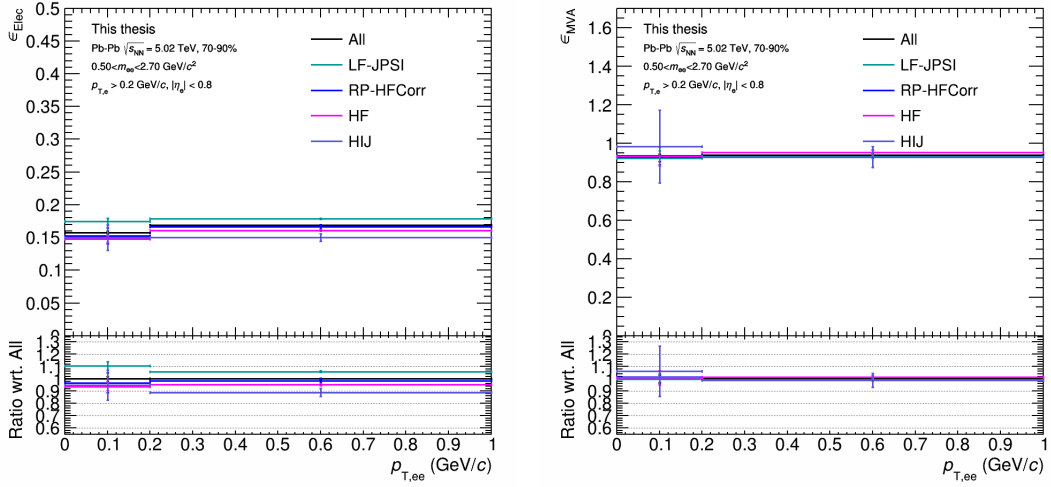


Figure 5.19.: Comparison of efficiencies for different dielectron sources in m_{ee} : $0.5 - 2.7 \text{ GeV}/c^2$. Left: Electron selection efficiency (ϵ_{Elec}) for different signal definitions with preselection cut 12 and MVA cut 0. Right: MVA efficiency (ϵ_{MVA}) for different signal definitions with preselection cut 12 and MVA cut 2.

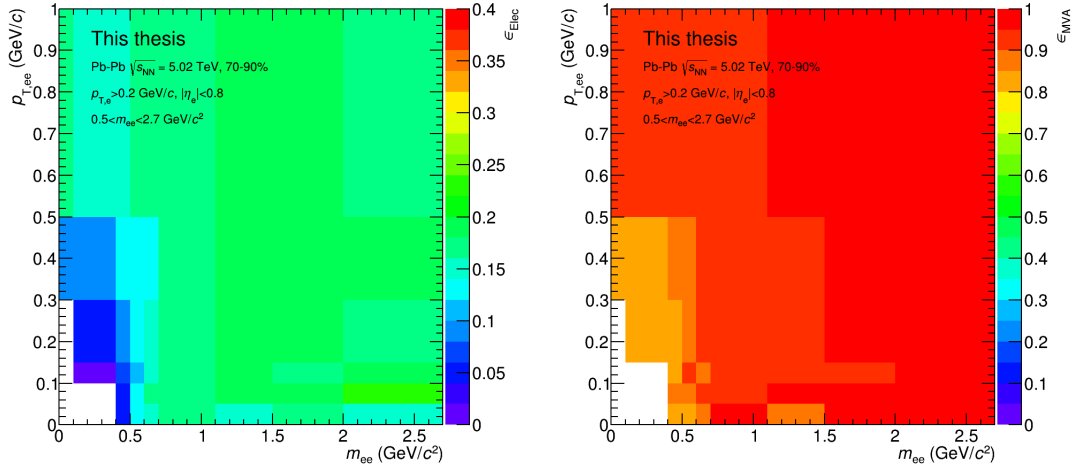


Figure 5.20.: Efficiency ϵ_{Elec} for preselection cut 12 (left) and ϵ_{MVA} for MVA cut 2 (right), which are the cuts used for the $p_{T,ee}$ spectrum in m_{ee} : $0.5 - 2.7 \text{ GeV}/c^2$.

In the analyses the efficiencies corresponding to ALL in Table 5.5 are used (black in Fig. 5.19 and Fig. 5.17). Figure 5.18 and Fig. 5.20 show for both mass ranges the efficiencies ϵ_{Elec} (left) and ϵ_{MVA} (right) in the m_{ee} - $p_{T,ee}$ plane. These efficiencies correspond to the cuts which are selected by the procedure described in Section 5.8.2 for the result.

5.8.2. Result selection and systematic cut uncertainty

An estimate of the systematic cut uncertainty is obtained by comparing the spectra resulting from varying preselection and MVA cuts. For this purpose all preselection and MVA cuts are combined, totalling 110 studied cuts (resulting from the eleven preselection cuts described in Table 5.2 and ten MVA cuts described in the end of Section 5.4.3). As not all 110 cuts are equally well suited for this analysis, only a subset is considered for the estimation of the systematic cut uncertainty. Whether a given cut is selected depends on the statistical significance of the corresponding corrected spectrum:

$$z_{\text{Corr}} = \frac{US_{\text{Sig}}^{\text{Corr}}}{\sigma_{\text{Stat}}} = \frac{1/\epsilon_{\text{Tot}} \cdot US_{\text{Sig}}}{\sigma_{\text{Stat}}}, \quad (5.8)$$

where US_{Sig} is defined in Eq. (5.2) and ϵ_{Tot} in Eq. (5.7). The statistical uncertainty of $US_{\text{Sig}}^{\text{Corr}}$ is denoted by σ_{Stat} and accounts for the statistical uncertainty of US , LS and ϵ_{Tot} .

To minimise statistical fluctuations z_{corr} is calculated in a single $p_{T,ee}$ -bin ranging from 0.2 – 1 GeV/ c for each cut. This interval is selected to exclude the $p_{T,ee}$ region dominated by photo-produced dielectrons ($p_{T,ee} \approx 0 - 0.2$ GeV/ c), which should avoid a biased cut selection with respect to a potential photo-production signal. A cut is selected for the estimation of the cut systematics if its z_{corr} is more than 0.8 standard deviations above the mean z_{corr} . The standard deviation and mean of z_{corr} are calculated using the z_{corr} values of all 110 cuts. The cut value at 0.8 standard deviations reflects a trade-off between a wide range of different considered cuts and the exclusion of unsuitable cuts.

The cut used for the final spectrum is the one with the smallest squared deviation from the z_{corr} weighted average result ($\langle US_{\text{Sig},i}^{\text{Corr}} \rangle_{z_{\text{corr}}}$) among all selected cuts in the $p_{T,ee}$ range 0-1 GeV/ c with the binning defined in Section 5.5:

$$\Delta^2 = \sum_{i \in \text{bins}[0,1]} (US_{\text{Sig},i}^{\text{Corr}} - \langle US_{\text{Sig},i}^{\text{Corr}} \rangle_{z_{\text{corr}}})^2. \quad (5.9)$$

The weighting with z_{corr} assigns a higher relevance to cuts that yield a more significant signal. In the analysis of 70–90% centrality and m_{ee} : 1.1 – 2.7 GeV/ c^2

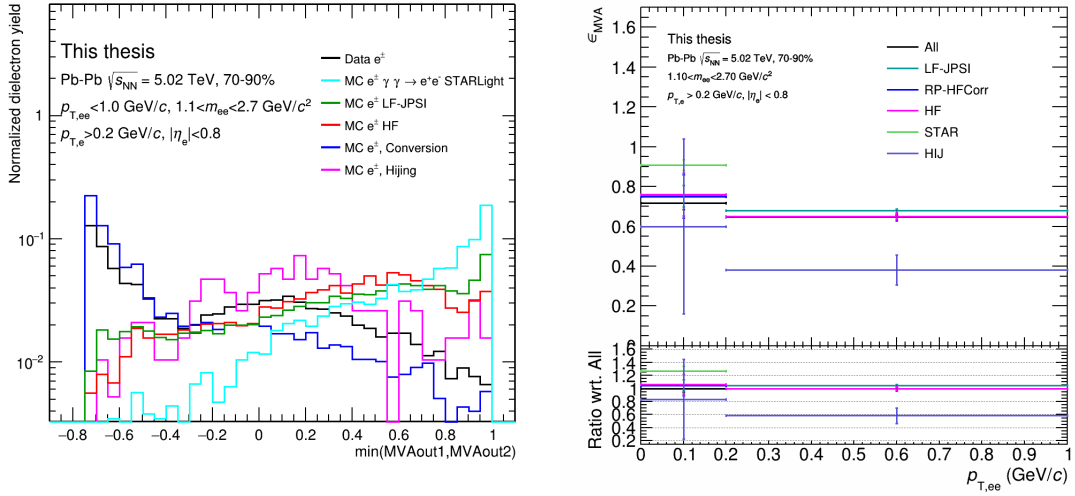


Figure 5.21.: Left: Distribution of the minimum of the MVA outputs of the two tracks associated to dielectrons for m_{ee} : $1.1 - 2.7 \text{ GeV}/c^2$, $p_{T,ee} < 1 \text{ GeV}/c$ and preselection cut 0. Only if the value of this quantity is above the MVA cut do the dielectrons pass the cut selection. Right: MVA efficiency ϵ_{MVA} for preselection cut 0 and MVA cut 6, corresponding to a cut on the MVA output at 0.2.

an additional criterion is applied for the selection of the final cut. It is found that strong MVA cuts lead to rather large estimated systematic uncertainties. The reason for this is that in the 70–90% centrality range MVA cuts above -0.2 mainly reject non-conversion signal dielectrons. This can be seen in the left panel of Fig. 5.21. An MVA cut above -0.2 affects the range where conversion dielectrons (blue) are not dominant, but where signal dielectrons (magenta and red) are expected. The distribution of the signal in this region differs for different signal sources. Therefore, cuts in this region would lead to a source dependence of the efficiency, as Fig. 5.21 (right) shows for the case of an MVA cut at 0.2. The origin of this source dependence has not been identified so far. However, an MVA cut at -0.2 already rejects a good fraction of conversions and keeps most of the signal (see Fig. 5.21, left)). Therefore, for the selection of the final cut only MVA cuts below 0 are considered. For the selection of the cuts which are used for the estimation of the systematic cut uncertainty (explained below) this requirement is not applied. This restriction is only applied in m_{ee} : $1.1 - 2.7$ as here MVA cut 6 (i.e a cut at MVA output 0.2) would otherwise be selected by the cut selection procedure. In m_{ee} : $0.5 - 2.7 \text{ GeV}/c^2$ this additional criterion is not necessary since here MVA cut 2 (i.e a cut at MVA output -0.8) is selected. A cross-check to test if this cut

selection procedure biases the result is described in Section 5.11.2. The finally selected cut in m_{ee} : $1.1 - 2.7 \text{ GeV}/c^2$ uses the preselection cut 20 and MVA cut 4. The corresponding spectrum is the solid green line in Fig. 5.22 (left). This figure shows the spectra corresponding to the cuts which are selected for the cut variation. The cuts are specified by the number of the preselection cut after “Pres” and the MVA cut number after “MVA”. In m_{ee} : $0.5 - 2.7 \text{ GeV}/c^2$ the preselection cut 12 and MVA cut 2 is selected (solid green line in Fig. 5.22, right). Figure 5.23 shows the impact of the MVA cut in both mass ranges on the raw yields US , LS and $US - LS$ (top panel), the raw signal over background ratio (middle panel) and the statistical significance of the corrected signal in a single $p_{T,ee}$ -bin of $0 - 1 \text{ GeV}/c$ (bottom panel). The latter shows that conversion rejection is crucial as it substantially increases the statistical significance of the corrected signal. Since the corrected signal is used for the statistical significance, the statistical uncertainty of the efficiency also enters the calculation. Thus, the eventual drawback of an MVA cut in terms of limited MC data and large corresponding statistical uncertainties in the efficiencies is included in this comparison.

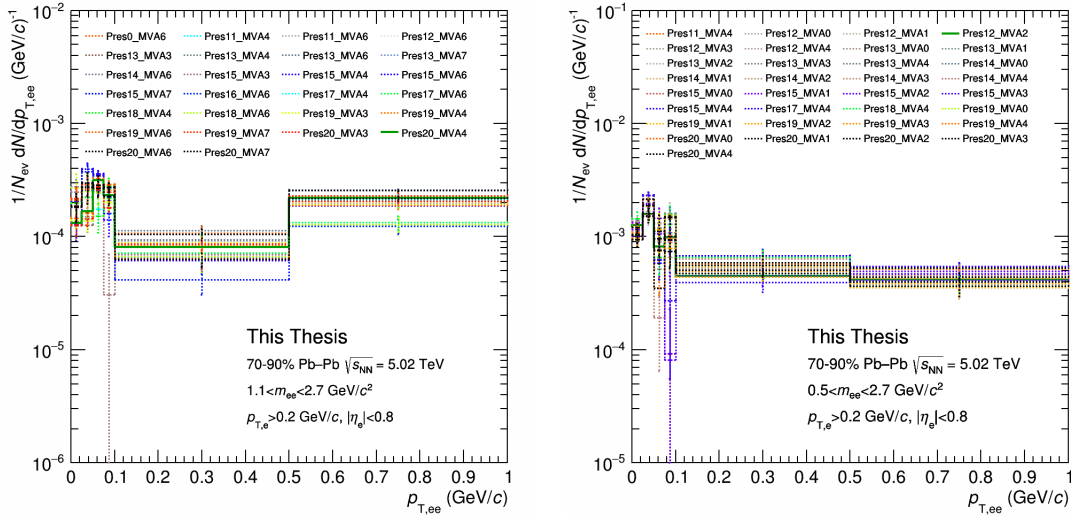


Figure 5.22.: The cuts which are selected for the estimation of the cut systematics in both mass ranges. The spectra shown in the solid green line are the ones which are chosen for the final result.

The relative systematic cut uncertainty (σ_c^{Rel}) is determined in the $p_{T,ee}$ -bin of $0 - 1 \text{ GeV}/c$. It is estimated using the z_{corr} -weighted mean absolute error between the corrected signal US_{Sig}^i of all cuts i satisfying the z_{corr} -based selection criterion

($i \in S$) and the unweighted average spectrum $\langle US_{\text{Sig}} \rangle$:

$$\sigma_c^{\text{Rel}} = \frac{\sum_{i \in S} |US_{\text{Sig}}^i - \langle US_{\text{Sig}} \rangle| z_{\text{Corr}}^i}{\sum_{i \in S} z_{\text{Corr}}^i} \frac{1}{\langle US_{\text{Sig}} \rangle}. \quad (5.10)$$

The resulting relative systematic cut uncertainty is then applied to the result in each individual $p_{T,ee}$ -bin.

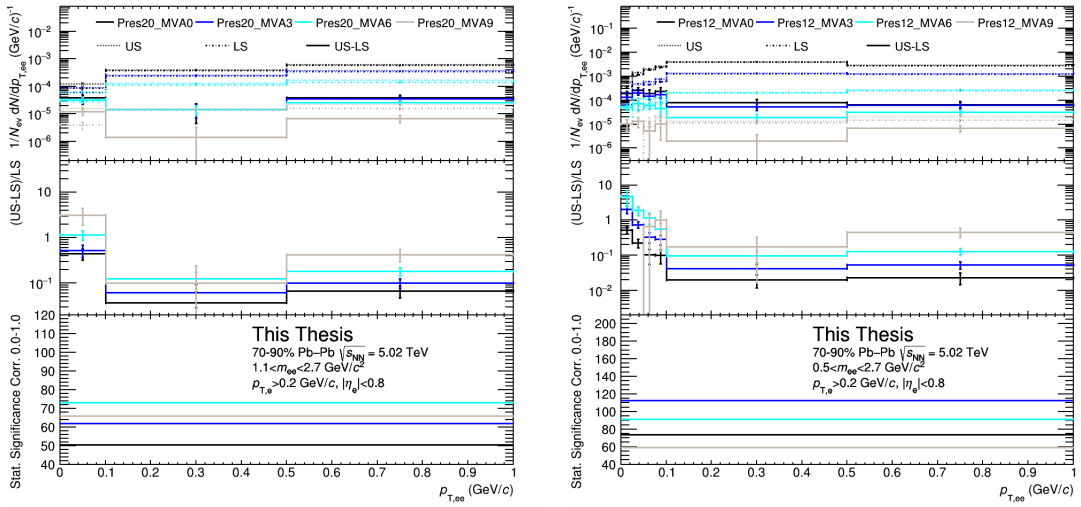
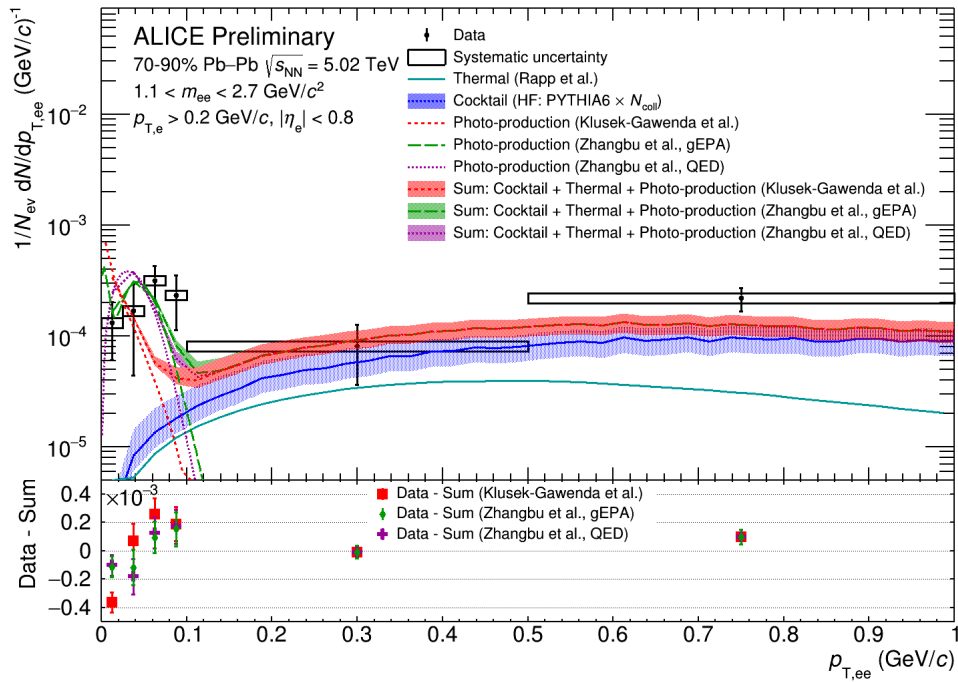


Figure 5.23.: Raw yields of US , LS and $US - LS$ (top panel), ratio of raw signal ($US - LS$) and raw background (LS) (middle panel) and statistical significance of the corrected signal in a single $p_{T,ee}$ -bin of 0 – 1 GeV/ c (bottom panel).

As pointed out in Section 5.8.1 no systematic uncertainty due to source dependence of the efficiency is assigned in both mass ranges. The relative systematic uncertainty associated to the preselection and MVA cut is based on the aforementioned cut variation. This uncertainty amounts to 10% in m_{ee} : 1.1 – 2.7 GeV/ c^2 . In m_{ee} : 0.5 – 2.7 GeV/ c^2 the relative systematic uncertainty obtained by the cut variation amounts to 6%. Statistical uncertainties of the data and the efficiencies are contained in the statistical uncertainties associated to the data.



ALICE-PPHE-126033

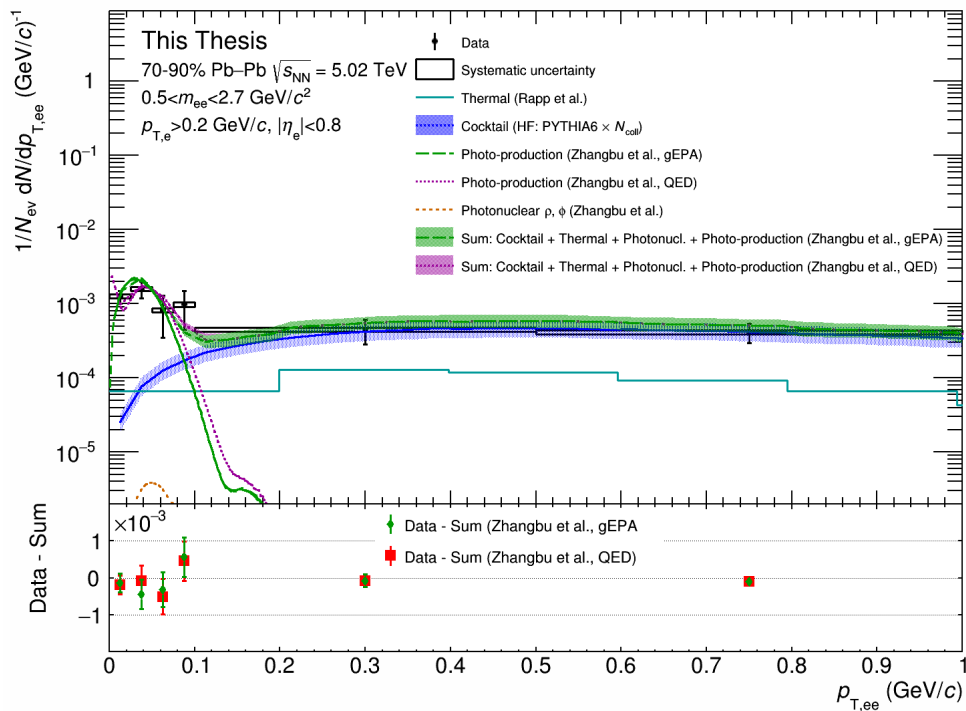


Figure 5.24.: Comparison of the $p_{T,ee}$ spectra in m_{ee} : 1.1 – 2.7 GeV/c² (top) [138] and m_{ee} : 0.5 – 2.7 GeV/c² (bottom) to the cocktail and model calculations. The lower panels show the difference between the measured data points and the sum of the expectations.

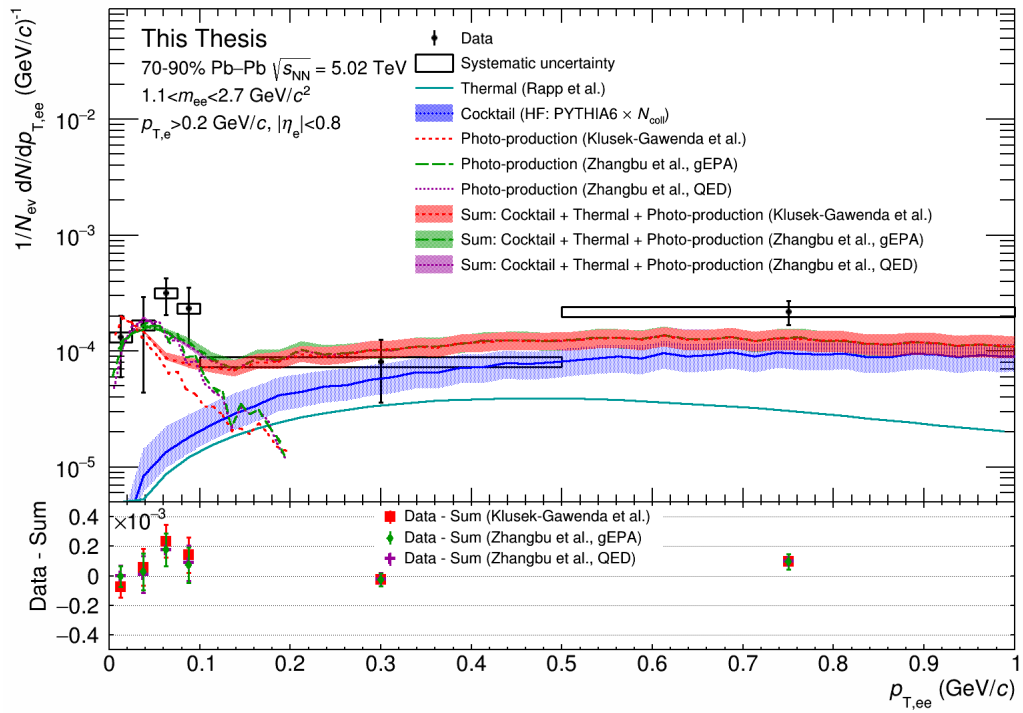


Figure 5.25.: Comparison of the $p_{T,ee}$ spectrum in m_{ee} : $1.1 - 2.7$ GeV/c² to smeared photo-production calculations. The lower panel shows the difference between the measured data points and the sum of the expectations.

5.8.3. Results

Figure 5.24 compares the $p_{T,ee}$ spectra in both mass ranges with the corresponding model calculations and the cocktail. In this comparison the model calculations are used in their unsmeared version, i.e. no resolution effects are applied. The systematic uncertainty is indicated by the error boxes and the statistical uncertainty by the error bars. The bottom panels show the difference between the data and the sum of a photo-production model, the hadronic cocktail and thermal radiation. Here the error bars represent only the statistical uncertainty.

To determine the significance of the excess with respect to the cocktail and thermal radiation, the data is rebinned such that the first bin ranges from 0 – 0.1 GeV/ c . This range contains the observed excess. In this bin the local significance of the excess is calculated by dividing the difference of the expectation (i.e. cocktail + thermal dielectrons) by the sum in quadrature of the statistical and systematic uncertainty of the data and the systematic uncertainty of the cocktail. The resulting significance of the excess in $p_{T,ee} < 0.1$ GeV/ c is 3.3σ in $m_{ee}: 1.1 - 2.7$ GeV/ c^2 and 4.8σ in $m_{ee}: 0.5 - 2.7$ GeV/ c^2 . No systematic uncertainty of the thermal dielectron contribution provided by R. Rapp is available and therefore it does not contribute to the overall uncertainty. As the thermal contribution is sub-dominant this shortcoming is expected to be of minor importance for the significance of the excess.

Thermal radiation calculations for $m_{ee}: 0.5 - 2.7$ GeV/ c^2 are currently only available in the coarse binning shown in Fig. 5.24 (bottom).

Figure 5.25 shows the results in $m_{ee}: 1.1 - 2.7$ GeV/ c^2 with the smeared photo-production models (see Section 5.7).

See Section 5.12 for a discussion of these results.

5.9. Dielectron $p_{T,ee}$ spectra in 0–40% centrality

The analysis in the centrality range 0–40% is widely analogous to the one in 70–90%. No additional restriction on the selection of the MVA cut as in the analysis of the 70–90% centrality range is necessary. However, as pointed out in Section 5.5, for the signal extraction in 0–40% the R-factor is applied.

As in the 70–90% centrality range, also in this centrality range a classifier is trained and used for conversion rejection (see Section 5.4.3). Figure 5.26 shows the efficiencies ϵ_{Elec} (left) and ϵ_{MVA} (right) of the finally selected cuts for various signal sources in the mass range of 1.1 – 2.7 GeV/ c^2 . Since the efficiencies for the injected LF sources (dark cyan) appear systematically higher, systematic uncertain-

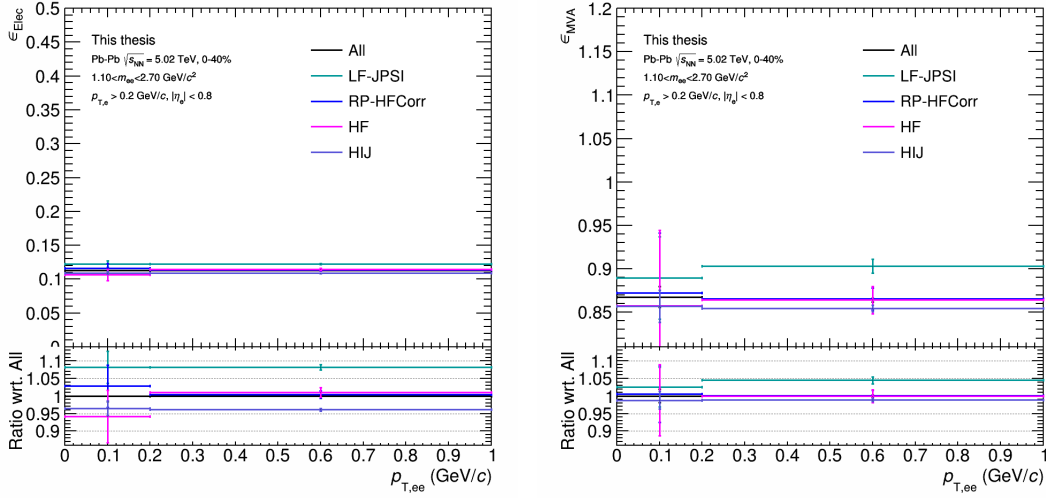


Figure 5.26.: Comparison of efficiencies for different dielectron sources in m_{ee} : 1.1 – 2.7 GeV/c^2 . Left: Electron selection efficiency (ϵ_{Elec}) for different signal definitions with preselection cut 17 and MVA cut 0. Right: MVA efficiencies (ϵ_{MVA}) with MVA cut 3.

ties are assigned to the efficiencies. For the purpose of uncertainty estimation, the $p_{T,ee}$ -averaged efficiencies are estimated to be $\epsilon_{\text{Elec}} \approx 0.11 \pm 0.005$ (sys.) and $\epsilon_{\text{MVA}} \approx 0.87 \pm 0.02$ (sys.). Using error propagation and Eq. (5.7) the total efficiency is estimated to be $\epsilon_{\text{Tot}} \approx 0.096 \pm 0.005$ (sys.). Thus, the relative uncertainty in ϵ_{Tot} is estimated to be $\approx 5\%$. This uncertainty is added in quadrature to the uncertainty of the cut variation, which is $\approx 7\%$. This value is the result of a cut variation, as described in Section 5.8.2. The resulting total estimated relative systematic uncertainty of $\approx 8\%$ is applied to each $p_{T,ee}$ -bin in the spectrum.

Fig. 5.27 shows that there are also discrepancies among the efficiencies for the mass range of 0.5 – 2.7 GeV/c^2 . The efficiencies are estimated to be $\epsilon_{\text{Elec}} \approx 0.13 \pm 0.03$ (sys.) and $\epsilon_{\text{MVA}} \approx 0.75 \pm 0.08$ (sys.) on average in both $p_{T,ee}$ bins. These uncertainties are propagated to the total efficiency according to Eq. (5.7), which yields $\epsilon_{\text{Tot}} \approx 0.0975 \pm 0.025$ (sys.). Thus, the relative uncertainty in ϵ_{Tot} is $\approx 25\%$. The estimation of the cut uncertainty is $\approx 7\%$. This uncertainty is added in quadrature to the uncertainty of the efficiency. The resulting total relative systematic uncertainty is estimated to be $\approx 26\%$.

The raw (i.e. uncorrected) US , LS , $US - LS$ (top panel), the raw signal to background ratio (middle panel), and the statistical significance of the corrected signal (bottom panel) are shown in Fig. 5.28. The signal over background ratio is roughly two orders of magnitude lower than in the 70–90% centrality range (see Fig. 5.23). The achievable relative gain in statistical significance of the corrected signal is

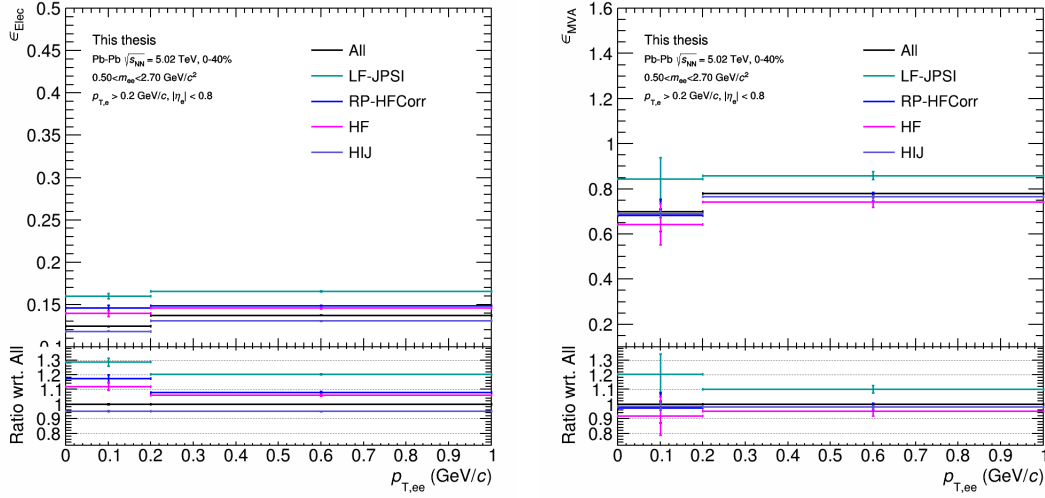


Figure 5.27.: Comparison of efficiencies for different dielectron sources in m_{ee} : 0.5 – 2.7 GeV/c². Left: Electron selection efficiency (ϵ_{Elec}) for different signal definitions with preselection cut 20 and MVA cut 0. Right: MVA efficiencies (ϵ_{MVA}) with MVA cut 3.

higher in the 0.5 – 2.7 GeV/c² mass range. This is expected as here the amount of combinatorial dielectrons in US and LS is the largest (top panel). The preselection cut 20 and MVA cut 3, which are selected for the final spectrum in this mass range, lead to a doubling in statistical significance compared to no conversion rejection, i.e. preselection cut 20 and MVA cut 0.

Due to the low signal over background ratio in this centrality range, the like-sign subtraction needs to be even more precise than in 70–90%. This requires application of the R-factor (see Eq. (5.2)) in the signal extraction. Depending on m_{ee} , the deviation of the R-factor from unity is on the order of 10^{-3} up to 10^{-2} for the cut selected in the 1.1 – 2.7 GeV/c² mass range (see Fig. 5.11, left). This is the same order of magnitude as the signal over background ratio in this mass range (middle panel in Fig. 5.28, left). Therefore, it is expected that the R-factor has a relevant impact on the result. The same reasoning holds for the mass range of 0.5 – 2.7 GeV/c². Consequently, the R-factor is applied in both mass ranges. Figure 5.29 shows that the effect of the R-factor is most pronounced in 0–40% centrality and here in particular for the mass range of 0.5 – 2.7 GeV/c² and at low $p_{T,ee}$. In this kinematic range the R-factor shows small deviations from unity (red and green in Fig. 5.11, left), which have a strong impact due to the low signal over background ratio in this m_{ee} region.

The error bars in Fig. 5.29 are the difference in quadrature of the statistical uncertainties of numerator and the denominator. This approximately accounts for the

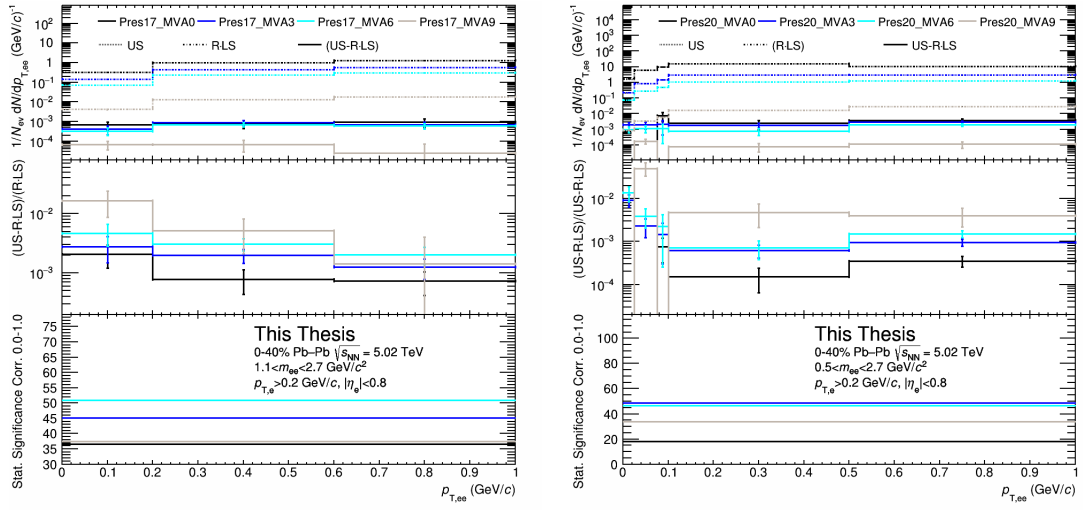


Figure 5.28.: Raw yields in m_{ee} : $1.1 - 2.7 \text{ GeV}/c^2$ (left) and m_{ee} : $0.5 - 2.7 \text{ GeV}/c^2$ (right) of US , LS and $US - R \cdot LS$ (top panel), ratio of raw signal ($US - R \cdot LS$) and raw background ($R \cdot LS$) (middle panel) and statistical significance of the corrected signal in a single $p_{T,ee}$ -bin of $0 - 1 \text{ GeV}/c$ (bottom panel).

fact that numerator and the denominator are statistically fully correlated except for the statistical uncertainty of the R-factor (see [139]).

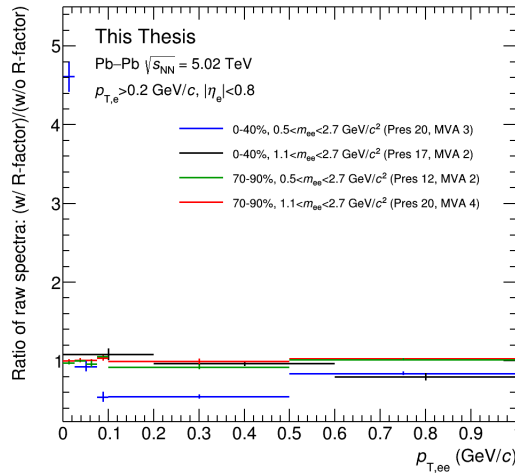


Figure 5.29.: Ratio of raw spectra of the signal with R-factor (i.e. $US - R \cdot LS$) with the spectrum of the signal without the R-factor (i.e. $US - LS$).

5.9.1. Results

Figure 5.30 shows the selected $p_{T,ee}$ spectra along with expectations. The corresponding cuts are preselection cut 17 and MVA cut 3 for m_{ee} : $1.1 - 2.7 \text{ GeV}/c^2$ and preselection cut 20 and MVA cut 3 for m_{ee} : $0.5 - 2.7 \text{ GeV}/c^2$. The error bars in the lower panel represent only the statistical uncertainty.

No significant excess with respect to the hadronic cocktail and thermal radiation is observed. See Section 5.12 for a discussion of these results.

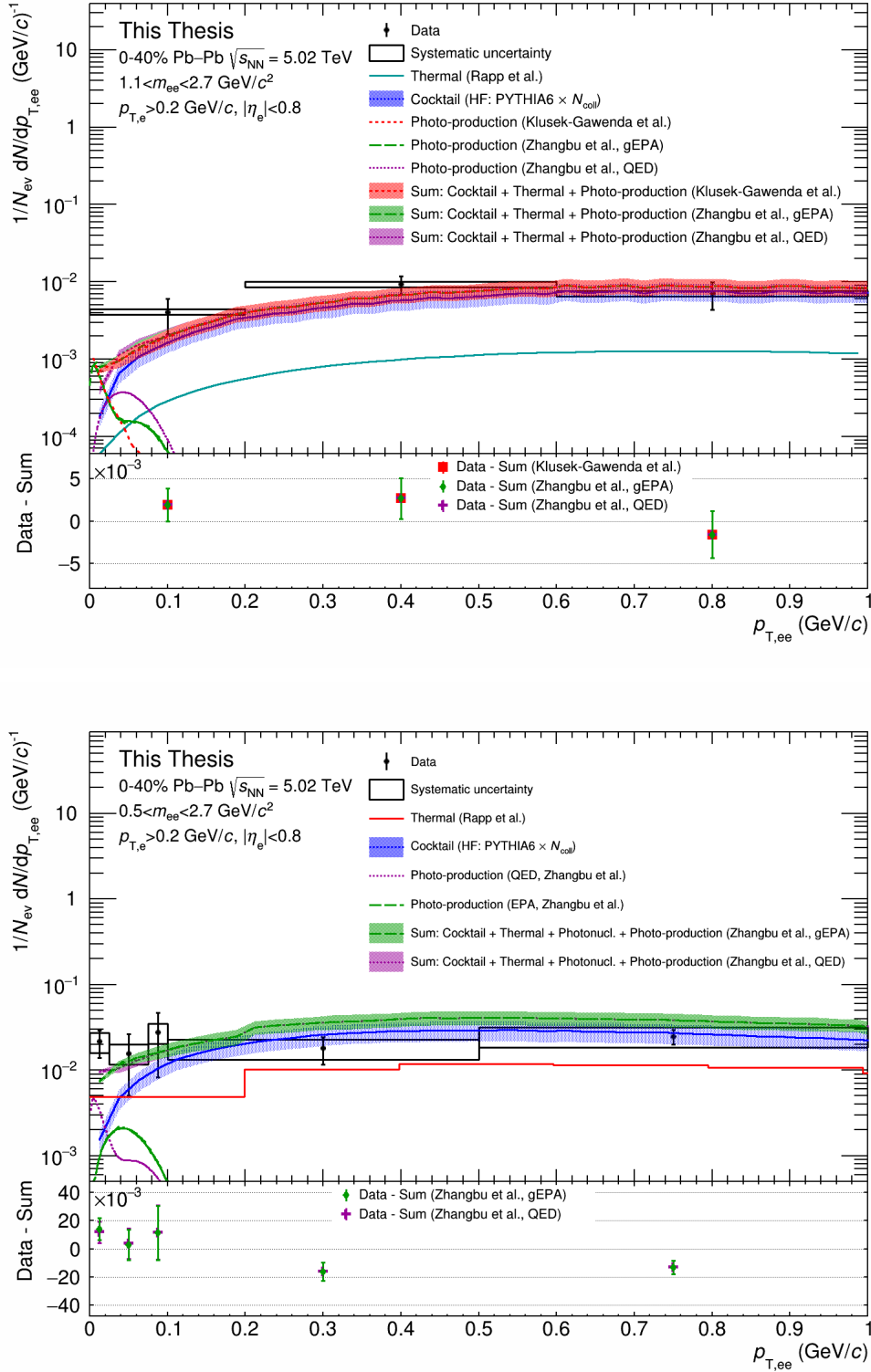


Figure 5.30.: Comparison of the $p_{T,ee}$ spectra in m_{ee} : 1.1 – 2.7 GeV/c² (top) and m_{ee} : 0.5–2.7 GeV/c² (bottom) to the cocktail and model calculations. The lower panels show the difference between the measured data points and the sum of the expectations.

5.10. Event plane differential spectra

There is motivation from theory to investigate low- $p_{T,ee}$ dielectron production in dependence of the orientation to the event plane. As discussed in Section 3.3.2, such dependencies are predicted by various recently proposed models of photo-production in HICs. The first, preliminary result of an analysis aiming at these dependencies is presented in the following.

The event planes are obtained using TPC tracks and the method described in Section 3.1. Since indications of photo-production are only observed in the centrality class of 70–90%, the study is restricted to this centrality interval. Both mass ranges of $0.5 - 2.7 \text{ GeV}/c^2$ and $1.1 - 2.7 \text{ GeV}/c^2$ are used. The cuts and efficiencies used to obtain the spectra are the same as in Fig. 5.24.

Two different kinds of event plane dependences are investigated. For one study the direction of the individual pair legs, i.e. the positron and electron track, is restricted to the quadrants that encompass either directions more parallel or perpendicular to the event plane. Effects like the rescattering of the leptons in the QGP could introduce differences in the corresponding spectra. A second analysis compares the spectra obtained for dielectrons, that have pair momentum vectors, i.e. the sum of the individual track momenta, in the aforementioned quadrants. These spectra could reveal effects that are predicted by the gEPA models (see Fig. 3.23, right). In either case, no quantitative predictions for the expected effect in the present analysis are available. However, any significant differences among the spectra corresponding to different directions with respect to event plane could provide first experimental hints for these effects.

For this analysis four sectors are defined that correspond to directions which encompass predominantly parallel (in event plane) or perpendicular (out of event plane) directions to the event plane. These directions are defined via the difference of the corresponding azimuthal angle (φ) with respect to azimuthal angle of event plane (Ψ). The following defines the intervals for the differentiated directions with respect to the event plane:

- In event plane: $|\varphi - \Psi| \in \left[0, \frac{\pi}{4}\right] \cup \left[\frac{3\pi}{4}, \pi\right]$,
- Out of event plane: $|\varphi - \Psi| \in \left[\frac{\pi}{4}, \frac{3\pi}{4}\right]$.

In the analysis which restricts the directions of the individual tracks the in and out of event plane spectra are obtained from tracks that are selected according to the azimuthal angle between the tracks and the event plane. The criterion for the tracks to be either in or out of event plane is applied to both tracks of a given dielectron. Figure 5.31 compares the corresponding spectra (green and red) to the

spectrum without any event plane dependent cuts (black, same as in Fig. 5.24). For $p_{T,ee} < 0.1$ GeV/ c there seems to be a tendency for more dielectrons in the event plane than out of the event plane, which is slightly more pronounced in the mass range of 1.1 – 2.7 GeV/ c^2 . Comparisons of the shape of the spectra are difficult due to the large statistical uncertainties.

For the analysis based on the pair momenta, it is the azimuthal angle between the pair momentum vector and the event plane that is restricted to in or out of event plane directions. Figure 5.32 shows the spectra corresponding to these selections (green and red), along with the event plane independent spectrum (black, same as in Fig. 5.24). No significant discrepancies are found between the compared spectra.

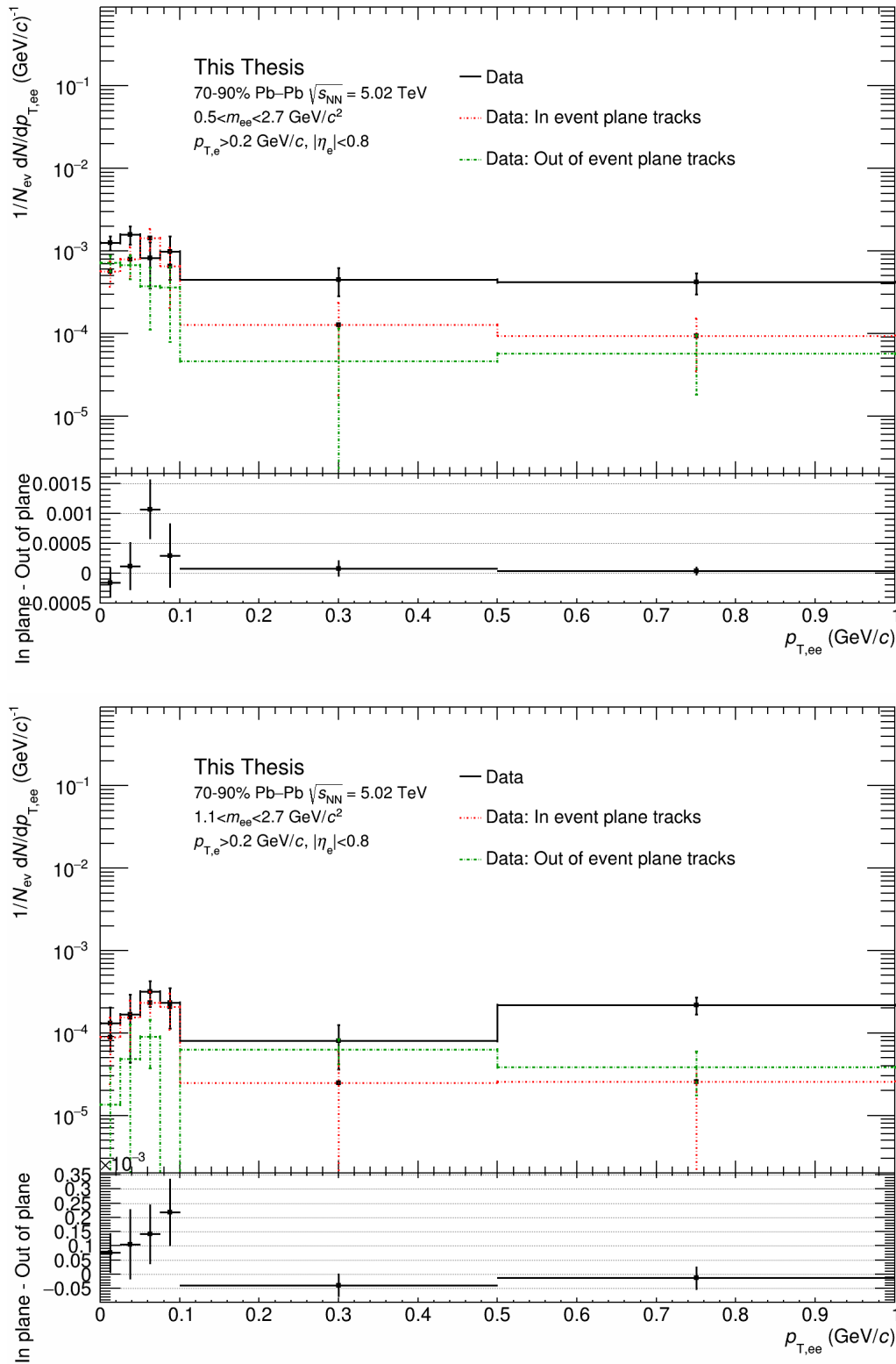


Figure 5.31.: Comparison of the spectrum without any event plane dependent selection (black) to the spectra for in (red) and out of (green) the event plane tracks in two mass intervals.

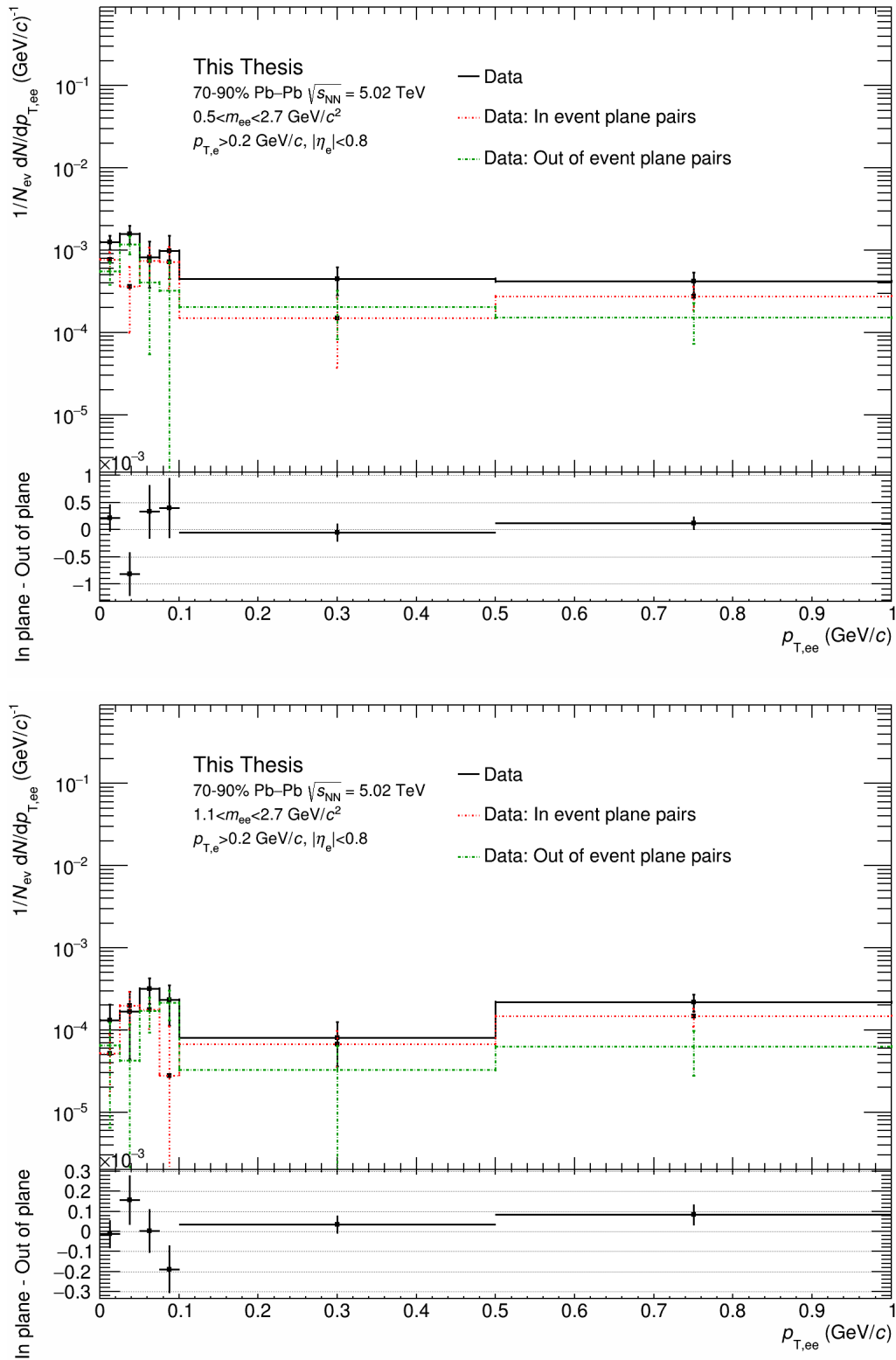


Figure 5.32.: Comparison of the spectrum without any event plane dependent selection (black) to the spectra for in (red) and out of (green) the event plane pairs in two mass intervals.

5.11. Cross-checks

This section describes cross-checks which are carried out in order to ensure that the result is reliable. The first concern which is addressed is the PID contamination. In addition, it is investigated if the cut selection procedure of Section 5.8.2 leads to spectra that are biased and if the like-sign subtraction method reproduces the expected signal in Monte Carlo simulations.

5.11.1. PID contamination

A possible concern in the dielectron analysis is that the spectrum is significantly influenced by non-electron contamination. This could for example come from π^\pm tracks. If unlike-sign pairs of these tracks are correlated, they may not be subtracted by the like-sign subtraction and may contribute to the final $p_{T,ee}$ spectrum. Such PID contamination should vary systematically if the PID cuts are tightened or loosened, i.e. if more or less contamination is accepted. The PID selection cuts which are used in the analysis (cuts between 0 and 20 in Table 5.2) are obtained from random combinations of loose and tight cuts on the individual PID variables ($n\sigma$ values). Therefore, none of them represents a specifically loose or tight PID selection.

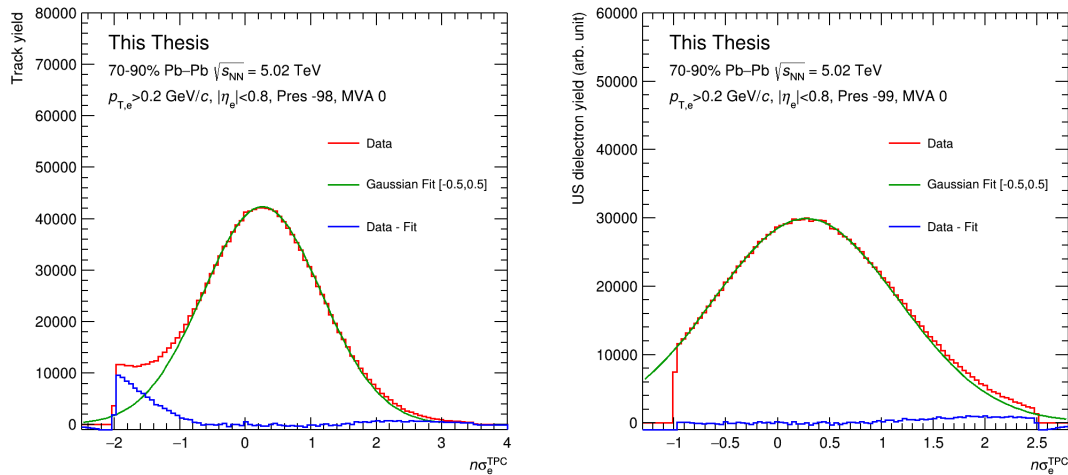


Figure 5.33.: Distribution of $n\sigma_e^{\text{TPC}}$ for a loose PID selection (left) and a tight one (right). The data (red) is shown along with a Gaussian fit (green) and the residual (blue).

To study if PID contamination contributes to the spectrum two dedicated PID cuts are defined. One combines the loosest cut selection in each PID variable (cut number -98 in Table 5.2) and another one the tightest PID selection (cut number -99). Figure 5.33 shows the distribution of $n\sigma_e^{\text{TPC}}$ of tracks selected with a loose PID selection (left) and a tight one (right). The data is fit with a Gaussian in the $n\sigma_e^{\text{TPC}}$ interval $[-0.5, 0.5]$. As the fit interval is expected to be dominated by electrons, these Gaussians distribution can be used as an approximation of the electron contribution to the $n\sigma_e^{\text{TPC}}$ distributions. Consequently, the residual between the data and the fit (blue) approximates the contribution from PID contamination. The fraction of contamination can be estimated as the ratio of the integral of the residual and the total data in the $n\sigma_e^{\text{TPC}}$ interval that is applied for the cuts. For the tight cut setting this ratio is 1.5% in the $n\sigma_e^{\text{TPC}}$ interval of $[-1, 2.5]$. With the loose PID cut the ratio is 6.6% in the $n\sigma_e^{\text{TPC}}$ interval of $[-2, 3.5]$. Therefore, it is expected that the relative contamination track fraction is more than $6.6/1.5 = 4.4$ times larger with the loose PID cuts compared to the tight ones.

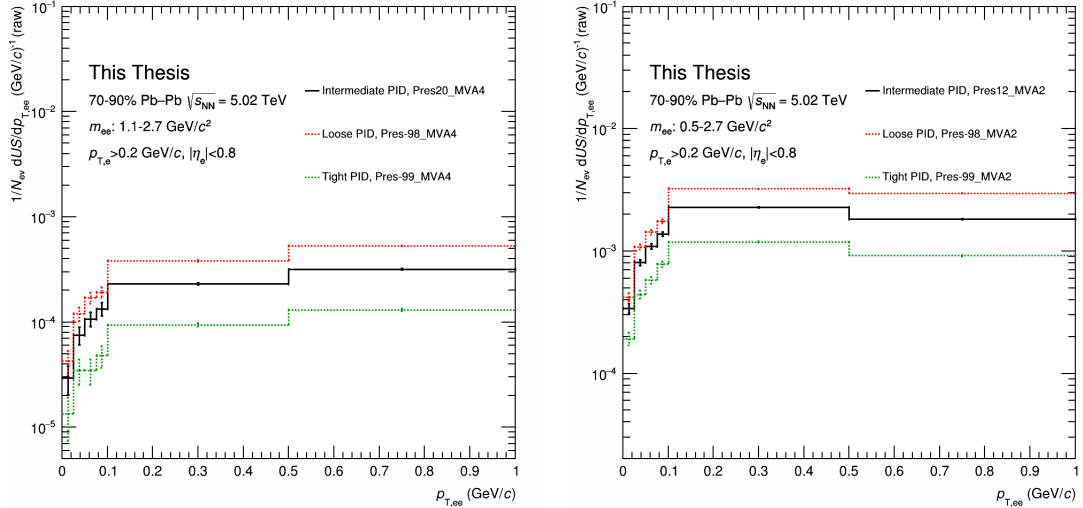


Figure 5.34.: Uncorrected (raw) $p_{T,ee}$ spectra of the US dielectrons (i.e. before like-sign subtraction) for the m_{ee} range of $1.1 - 2.7 \text{ GeV}/c^2$ (left) and $0.5 - 2.7 \text{ GeV}/c^2$ (right). The PID selection used for the final spectrum (black) is compare to the spectra with loose (red) and tight (green) PID cuts.

The raw yield (i.e. without efficiency correction) of unlike-sign dielectrons (US) for the preselection cuts used in the final $p_{T,ee}$ spectra and for the loose and tight PID cuts are shown in Fig. 5.34. The loose and tight PID cuts are combined with the same preselection and MVA cuts as used for the selected spectrum in the corresponding mass range. Therefore, the compared cuts differ only in terms of the

PID cuts. In the m_{ee} range of $1.1 - 2.7 \text{ GeV}/c^2$ the loose PID cut yields roughly four times more unlike-sign dielectrons than the tight PID cut. For the $0.5 - 2.7 \text{ GeV}/c^2$ m_{ee} range this factor is approximately three. The intermediate PID cuts, which are the ones used for the spectra in Fig. 5.24 and Fig. 5.30, fall in-between the loose and tight PID cuts.

To study if the spectra with loose and tight PID cuts lead to significantly different (corrected) $p_{T,ee}$ spectra, they are compared in Fig. 5.35. The data set of the tight PID cut is a subset of the intermediate PID cut, which in turn is a subset of the loose PID cut. Under these conditions the statistical uncertainties for the comparison of the data sets is obtained by subtraction in quadrature of the statistical uncertainties of the individual data sets [139]. Consequently, the expected statistical fluctuation for the comparison to the intermediate PID cuts is obtained by a subtraction in quadrature of the statistical uncertainties from the uncertainties of spectra with the loose and tight PID cuts. Figure 5.35 does not point to a systematic trend like, e.g. a higher spectrum with looser PID cuts.

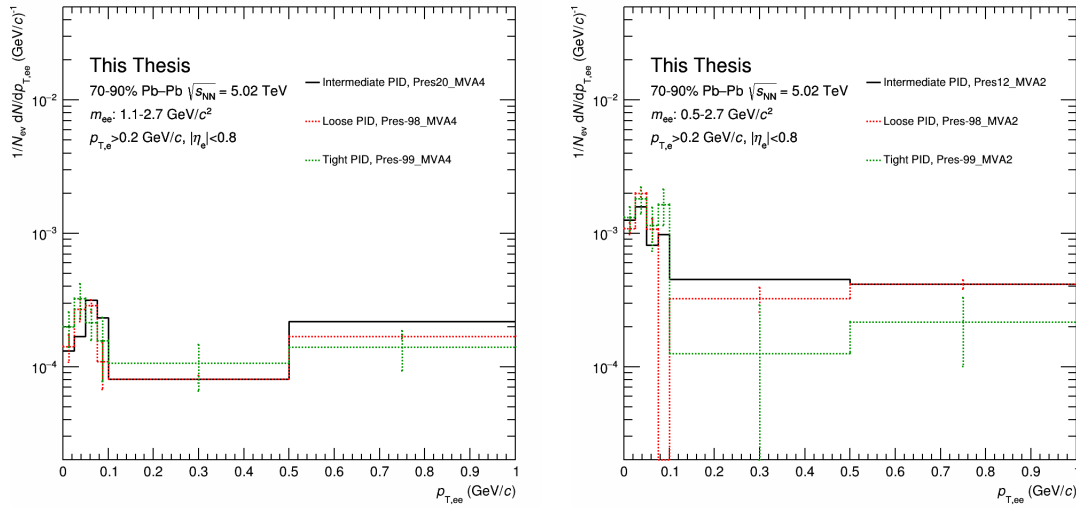


Figure 5.35.: Comparison of the selected spectra with the ones obtained with loose and tight PID cuts in $1.1 - 2.7 \text{ GeV}/c^2$ (left) and $0.5 - 2.7 \text{ GeV}/c^2$ (right) in the centrality class of 70–90%.

5.11.2. Cut selection bias

Another possible concern could be that the cut selection procedure described in Section 5.8.2 introduces a bias. The procedure aims at selecting a cut that is

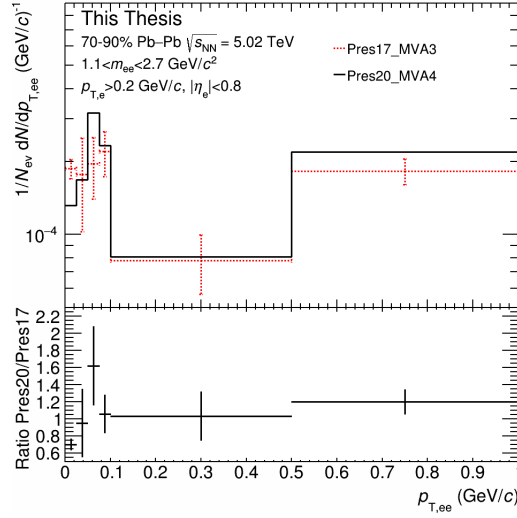


Figure 5.36.: Comparison of the spectra with the normal cut selection (Pres20_MVA4) and the inverted selection (Pres17_MVA3).

suitable for this analysis, i.e. it should yield a high statistical significance and be unbiased. The statistical significance of the corrected signal (z_{corr}) in the $p_{T,ee}$ range of 0.2 – 1 GeV/c is used to select a group of cuts which perform comparatively well. From this group the final cut is selected as the one which is closest to the z_{corr} weighted average of the selected cuts (see Section 5.8.2 for details). It would, however, be problematic if this selection is biased, for instance, with respect to the found excess.

To check whether this is the case, the final spectrum is also determined with an inverted cut selection. This means that the cuts which do not fulfill the 0.8 standard deviations cut criterion are selected. The final cut is the one which is closest to the average of these cuts. In contrast to the normal cut selection criterion, this average is calculated without z_{corr} weighting. The unweighted average is chosen since the weighting may introduce again a bias towards the cuts with high statistical significance.

The spectra with the normal and the inverted cut selection are compared in Fig. 5.36 for the m_{ee} range of 1.1 – 2.7 GeV/c². In both spectra the error bars of the spectrum selected by the normal procedure (Pres20_MVA4) are subtracted in quadrature from the error bars. This shall reflect the fact that the spectra were produced from the same data set and are therefore correlated. The statistical error bars of the individual spectra would be inappropriate to decide if the spectra are statistically compatible. If the spectra were produced from data sets such that one is a subset of the other, the subtraction in quadrature would represent the expected statistical fluctuations between the two spectra [139]. For the two com-

pared spectra this is, however, not the case. The cut Pres20_MVA4 has a tighter MVA cut than Pres17_MVA3, but a looser upper limit for $n\sigma_{\text{ITS}}^e$ and a looser lower limit for $n\sigma_{\text{TOF}}^e$ if available (see Table 5.2). Therefore, the error bars obtained from the subtraction in quadrature represent a lower bound on the ones which would correctly account for the statistical correlation between the underlying data sets of the two spectra.

Figure 5.36 shows no sign of a statistical incompatibility or a systematic trend (up- or downwards) between the normal (black) and the inverted (red) cut selection.

5.11.3. Like-sign subtraction

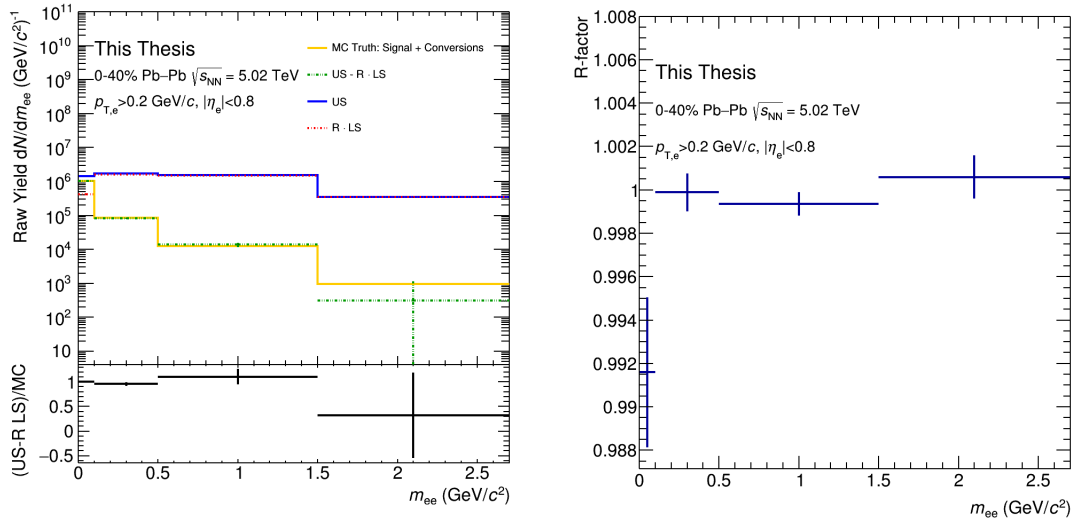


Figure 5.37.: Left: Comparison of the signal + conversion m_{ee} spectrum based on the MC truth (orange) and the spectrum extracted using like-sign subtraction (green). Right: The R-factor used for the like-sign subtraction.

The signal extraction in this analysis relies on the validity of Eq. (5.2), which states that the like-sign subtraction can be used to extract the spectrum of the unlike-sign signal pairs. In MC simulations this assumption can be tested using the MC truth, i.e. information from the MC generator that is used to infer if a dielectron is combinatorial (uncorrelated) or correlated. This study is based on a subset of the MC data used for the efficiency correction. Dielectrons coming from Hijing and the LF+ J/ψ injections (see Section 5.8.1) are used. Since the decay chains of heavy-flavour hadrons can be complicated, it is rather involved to determine unambiguously if such correlations exist for dielectrons coming from such

decays. To avoid this issue all dielectrons that have a heavy-flavour particle in the decay chain of one of their tracks are discarded. In addition, correlated dielectrons coming from conversions are also included in this study. They only affect the mass range below $\sim 0.1 \text{ GeV}/c^2$.

Figure 5.37 (left) shows a comparison of the m_{ee} spectra based on the MC truth information (orange) and the like-sign subtraction method (green). To maximise the statistical significance the test is performed on a $p_{T,ee}$ integrated spectrum and in the centrality range of 0–40%. The spectra are obtained using the preselection cut 20 (see Table 5.2) and the MVA cut 3 (see Section 5.4.3). No statistically significant deviation is observable and therefore no systematic uncertainty is assigned to the signal extraction. Figure 5.37 (right) shows the R-factor used in the like-sign subtraction, which, apart from a dip in the first bin, is compatible with unity.

5.12. Discussion and outlook

In the centrality range of 0–40% the $p_{T,ee}$ spectra (see Fig. 5.30) are compatible with the hadronic cocktail. An identification of thermal dielectrons on top of the cocktail is not possible with the present statistical uncertainties. The analysis is not sensitive to dielectron photo-production due to the large hadronic background. The $p_{T,ee}$ spectra in 70–90% (see Fig. 5.24) exhibit an excess below $0.1 \text{ GeV}/c$ with respect to the hadronic cocktail and thermal radiation. In both mass ranges the overall excess yield is in line with models of coherent photo-production. The three compared photo-production models differ significantly in terms of the shape of the $p_{T,ee}$ distribution. The model by Kłusek-Gawenda et al. (red) posits a sharp peak at $p_{T,ee} \rightarrow 0 \text{ GeV}/c$. This is in contrast to the calculations by Zhangbu et al. (green and purple), which both result in a peak at $p_{T,ee} \approx 0.04 \text{ GeV}/c$.

The measured spectrum in m_{ee} : $1.1 - 2.7 \text{ GeV}/c^2$ (Fig. 5.24, top) shows a peak around $p_{T,ee} \approx 0.06 \text{ GeV}/c$. The model by Kłusek-Gawenda et al. seems incompatible with the data. The models by Zhangbu et al. are in better agreement with the data, despite a peak position that is slightly too low. Therefore, it appears that the models by Zhangbu et al. are favoured by the data. These two models are too similar to differentiate between them.

In the mass range of $0.5 - 2.7 \text{ GeV}/c^2$ (Fig. 5.24, bottom) only calculations by Zhangbu et al. are available. Both models show excellent agreement with the data. An important aspect to be addressed is the inclusion of resolution effects in the model calculations. As discussed in Section 5.7, only estimations on these effects are currently possible. As shown in Fig. 5.16 (right), the estimated effect of the

resolution effects leads to a peak at non-vanishing $p_{T,ee}$ for the model by Klusek-Gawenda et al., and thus reduces the discrepancies to the data (see Fig. 5.25). The resolution effects on the models by Zhangbu et al. are less pronounced. Applying the resolution effects results in a similar agreement with data for all three models. Despite these potential caveats for the comparison of different models, the $p_{T,ee}$ spectra in Fig. 5.24 can be regarded as the first indication of coherent dielectron photo-production in peripheral HICs at the LHC.

The effect of the finite tracking resolution is to be addressed in a more rigorous way than with the present estimation. In addition, more differential data analyses could be used to address possible effects of a strong magnetic field, interactions with the QGP or the initial geometry (see Section 3.3.2). A first step in this direction are the event plane dependent spectra presented in Section 5.10. Here a hint for a larger low- $p_{T,ee}$ yield for tracks in the event plane than for tracks out of plane is found (see Fig. 5.31).

Very recently the STAR collaboration observed a correlation between the azimuthal angles of the dielectron and the individual e^\pm tracks in UPCs and HICs of 60–80% centrality. This result is interpreted as an indication of vacuum birefringence caused by an enormous magnetic field [140]. The feasibility of analogous analyses in ALICE is to be investigated.

Including Pb–Pb data from the heavy-ion run at the LHC in 2018 will double the amount of data in peripheral collisions. The statistical uncertainties may be further reduced by implementing additional background rejection methods. For instance, the main cocktail contribution, which is coming from correlated decays of heavy-flavour hadrons, could eventually be reduced by exploiting similar track observables (e.g. *DCA*) as was done for conversion rejection.

6. A search strategy for highly-charged particles

Motivated by the theoretical considerations discussed in Section 3.4.1, a strategy for searches of magnetic monopoles in Pb–Pb collisions at ALICE is developed. Typically ALICE does not conduct searches for rare and heavy particles, like hypothesised Beyond Standard Model particles. The reason for this is that the decay products of such particles are characterised by high p_T (> 50 GeV/ c), for which ALICE is not optimised (see Chapter 4). In addition, the maximum event recording rate of ALICE in pp collisions is orders of magnitude lower than in ATLAS and CMS. As the reach of exclusion limits from searches for rare particles depends on the amount of available data, ALICE is usually not competitive in such searches in pp collisions.

These arguments do not apply to the searches for magnetic monopoles in Pb–Pb collisions. First, the amount of recorded data in Pb–Pb collisions is rather similar among ALICE and ATLAS/CMS. For instance, in the latest Pb–Pb run at the LHC in 2018 ALICE recorded 0.55 nb $^{-1}$ [141] and ATLAS (CMS) 1.76 nb $^{-1}$ (1.85 nb $^{-1}$) [142, 143]. The LHC delivered 0.25 nb $^{-1}$ in this period to Point 8, where LHCb and MoEDAL are located. Thus, ALICE did not record orders of magnitude less Pb–Pb data than ATLAS and CMS, and more than LHCb and MoEDAL. Similarly, the drawback of ALICE in high- p_T track reconstruction does not play a role for magnetic monopole searches. These particles are expected to be stable and thus are not searched via high- p_T decay products but would be directly detected as they traverse the detector. The higher the mass of the monopole, the less collision energy that can be converted to kinetic energy of the monopole and consequently the lower is the monopole p_T . Therefore, it is beneficial that ALICE has the lowest material budget of the four large detectors at the LHC. The low material budget maximises the chances that a highly ionising particle (HIP), i.e. a particle with stopping power ($-dE/dx$) values more than ten times higher than for relativistic standard model particles, reaches sensitive detector elements that allow its identification. It can be expected that monopoles would be accelerated along the strong initial magnetic field in the HICs and thus they would be primarily produced at mid-rapidity ($|y| \approx 0$) [144]. Figure 6.1 shows the minimal

kinetic energy of magnetic monopoles at mid-pseudorapidity to be detected by the various different detectors at the LHC according to simulations. Owing to its low material budget and comparably low B field, the ALICE detector requires the lowest monopole energies [96].

In summary, the theoretical considerations discussed in Section 3.4.1 together with unique capabilities of ALICE motivate searches for magnetic monopoles in Pb–Pb collisions with ALICE.

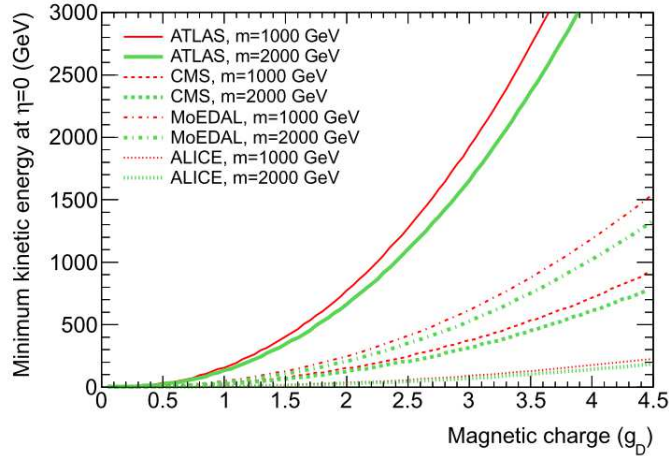


Figure 6.1.: The minimal kinetic energy necessary for magnetic monopoles at mid-pseudorapidity to reach detector elements that can be used in their searches at different detectors at the LHC [96].

6.1. Concept

For readers not familiar with the TPC in ALICE it is advisable to first read the corresponding parts in Chapter 4.

The reconstruction of tracks corresponding to HIPs by the standard algorithms is rather unlikely as the involved procedures are not optimised for this task. Therefore, the most reliable and unbiased data set for the search is not the reconstructed data but rather the raw data. This raw data contains information on the clusters of detector hits, including potentially malfunctioning regions of the detector. The TPC (Chapter 4) is selected as the most suitable sub-detector in ALICE to conduct monopole searches on raw data. It provides up to 159 three-dimensional track points (x, y, z) along with $-dE/dx$ information at each track point. Thus,

searches with the TPC can exploit the high $-dE/dx$ of monopoles as well as their curvature along the B field. The latter would require dedicated track reconstruction, which is computationally very expensive, especially for Pb–Pb raw data. The $-dE/dx$ information, in contrast, can be directly used as input for the search without further data preprocessing steps. Due to these aspects the search is based primarily on the analysis of recorded $-dE/dx$ information. However, in case an anomaly in the $-dE/dx$ -based search is encountered, the track curvature along the B field could be used to determine if magnetic charges are involved.

For HIPs at $\beta < 0.9999$ the dominant energy loss mechanism is ionisation, which is described by Eq. (3.18) [97]. For masses below $100 \text{ GeV}/c^2$ monopoles at the LHC could exceed this β value and the total $-dE/dx$ would be even higher as bremsstrahlung starts to become significant. However, monopole production in HICs is not expected to be the result of hard scattering processes but rather a consequence of the involved B fields. The estimated β values are thus expected to be smaller than 0.995 [144], justifying the consideration of ionisation only. Nevertheless, if the monopole $-dE/dx$ would be higher, for instance because it has multiple unit charges or bremsstrahlung is relevant, the presented search strategy would still be applicable.

In the following, $-dE/dx$ values for electrically and magnetically charged particles are compared. For electrically charged particles the $-dE/dx$ calculations are based on the Bethe-Bloch equation Eq. (4.2). For magnetic monopoles $-dE/dx$ is calculated using the Ahlen equation Eq. (3.18). The validity of both equations is restricted to $\beta > 0.1$ [96].

Figure 6.2 shows the $-dE/dx$ values according to these equations for protons, fully ionised carbon ions and magnetic monopoles of unit charge in Argon gas as a function of β . The stopping power for relativistic (i.e. $\beta \approx 1$) monopoles is three (two) orders of magnitude higher than for the protons (carbon ions).

The dynamic range of the $-dE/dx$ measurement with the TPC reaches up to ≈ 60 times the $-dE/dx$ of a minimally ionising particle (MIP), which corresponds approximately to the minimum $-dE/dx$ of the proton in Fig. 6.2). Thus, a relativistic monopole would exceed this range by far. The TPC is not designed and calibrated for the large charge depositions by tracks with monopole-like stopping power. To conduct a search for such tracks it is crucial that the characteristics of the hypothetical signal is known with maximum precision. Ideally, one would study the TPC data corresponding to tracks with $-dE/dx$ values in the same range as for monopoles. Observing such high $-dE/dx$ tracks would allow the formulation of reliable search criteria based on expectations that are derived from empirical data. This would be in contrast to the monopole searches conducted by ATLAS, which are primarily based on models of the response [145].

As electrically charged particles slow down ($\beta \rightarrow 0$) their stopping power increases

$-dE/dx$ in Argon ($Z = 18$, $A = 24$, $I = 180$ eV)

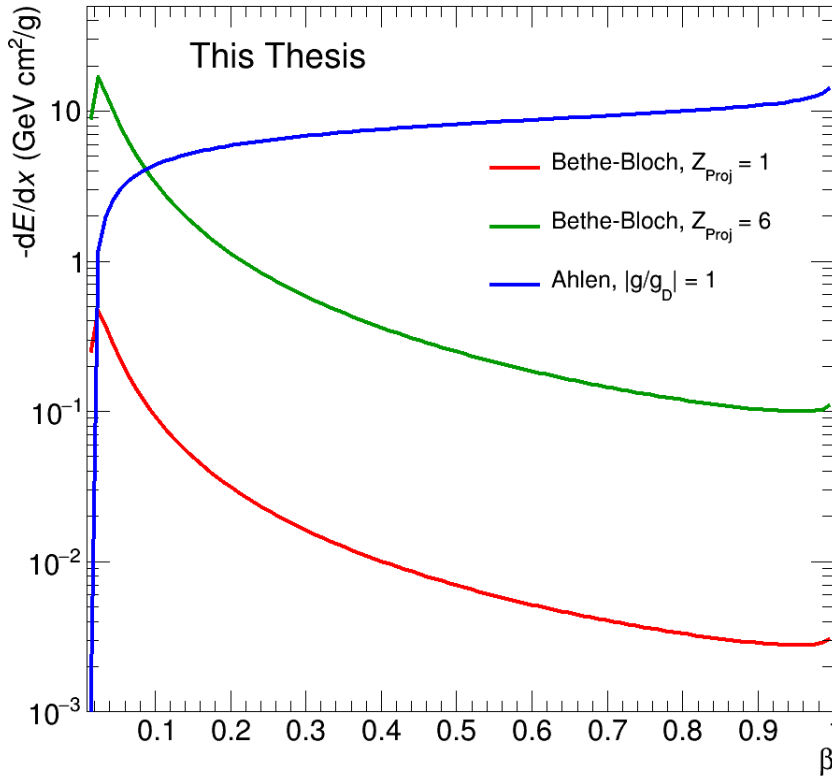


Figure 6.2.: Comparison of $-dE/dx$ in Argon calculated for protons (red), carbon ions (green) and magnetic monopoles (blue) of unit magnetic charge g as a function of β .

drastically. Consequently, they deposit an over-proportionally large fraction of their energy just before they stop. This intense energy deposition is called Bragg peak. At $\beta \approx 0.1$, which is the lower limit of the validity range of Fig. 6.2, the $-dE/dx$ of the proton is still roughly an order of magnitude lower than that for a relativistic monopole. In the Bragg peak ($\beta \leq 0.1$) of carbon ions, however, $-dE/dx$ is in the same region as for a relativistic monopole of unit charge. Nuclear fragments in the TPC, i.e. products of collisions between nuclei belonging to detector material and particles created in HICs, could in principle have atomic numbers up to the one of the main component of the TPC gas, Argon ($Z=18$). Such fragments are not tracked as they do not come from the primary interaction vertex and are thus in general not relevant to analyses of HICs. For the present search, however, they may allow an investigation of what the TPC data would look

like if tracks with $-dE/dx$ values comparable to the one expected for magnetic monopoles pass through the TPC.

If the charge deposition in a TPC read-out channel, a so-called pad (Fig. 6.3), exceeds the maximally measurable signal, the observed signal is expected to remain above the maximum value, the so-called threshold, for a time period that is proportional to the total charge deposition. This so-called Time Over Threshold (TOT) behaviour is caused by the read-out electronics. It shall be studied and calibrated under real data taking conditions as it would play a central role in a monopole search. As Fig. 6.2 shows, a proton's Bragg peak should result in $-dE/dx$ values more than 60 times larger than the minimal $-dE/dx$ value of a proton. Therefore, it should exhibit the time over threshold behaviour. To verify this expectation, one has to find a stopping proton in the TPC raw data. Subsequently, one could study higher $-dE/dx$ values by searching for heavier nuclear fragments.

6.2. Data structure

Before discussing the event selection in TPC raw data, the structure of the data shall be outlined. The TPC provides information on the x , y and z position and charge deposition. The x and y coordinates are inferred from the read-out pad location (see Fig. 6.3) and z from the time at which the charge signal arrives and the drift velocity. The charge is read out in 72 different sectors, which are framed by the support structures in Fig. 6.3 (left). Figure 6.3 (right) shows two sectors (one called inner chamber and one outer chamber). They contain read-out pads which are organised in pad rows. The pad area is on the order of $\approx 5 \times 10 \text{ mm}^2$ and the z resolution is typically on the order of $\approx 1 \text{ cm}$.

Clusters of pad signals are formed by grouping adjacent pads, which indicate a charge signal, in the pad direction (i.e. along a given pad row) and the z direction. Saving information like position and measured charge for a cluster rather than for individual pads is more resource efficient (see [148] for details). In the following, clusters are analysed in terms of the maximal signal amplitude in the cluster. The TPC signal amplitude is the digitised charge information of integers in the range of 0 – 1000, where 1000 corresponds to charge deposition expected from a track with a stopping power approximately 60 times higher than that for a minimally ionising particle. Thus, each cluster is represented by the highest charge deposition in the pads and time bins associated to this cluster. In the presence of a high $-dE/dx$ signal, that is spread out due to charge diffusion and TOT, the clusterisation may split large clusters at local minima of the signal, which correspond to fluctuations.

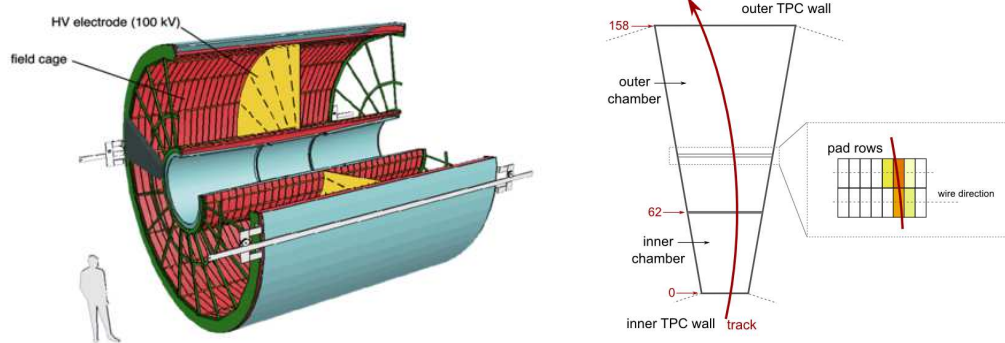


Figure 6.3.: Left: Schematic geometry of the TPC and its sectors, which are framed by the support structures (green) [146]. Right: Structure of two sectors in terms of pad rows and individual pads [147].

Therefore, it is expected that there are multiple clusters in azimuthal (pad) and z (time) direction that are associated to the same charge deposition.

6.3. Demonstration

The search for stopping nuclear fragments starts with a preselection of potentially interesting events. The criterion for event selection is that there has to be a TPC sector which exhibits a TOT of three clusters in at least three consecutive pad rows (see Fig. 6.3). This aims at a radially outwards going nuclear fragment that deposits enough charge to result in non-vanishing TOT in its Bragg peak. Apart from fragments, this selection also yields tracks with momentum vectors along the z -axis. Such tracks would produce a signal in several consecutive time bins around a pad position, mimicking TOT of a high $-dE/dx$ signal. Using more complicated event selection criteria, which can suppress this background by performing a simplified tracking, was found to be computationally too expensive. For test purposes the event selection is applied to a subset of the data set from the Pb–Pb run in 2015. The fraction of selected events is 2.5×10^{-4} . In total 650 events were selected for this test.

In the next step, events with promising tracks are selected based on histograms of the charge distribution of clusters in the $x-y$ and $z-y$ plane. For this demonstration it is judged visually if a track appears to correspond to a particle that stopped in the TPC. A more sophisticated automated selection could be implemented in the future, as at this stage the data volume is already massively reduced.

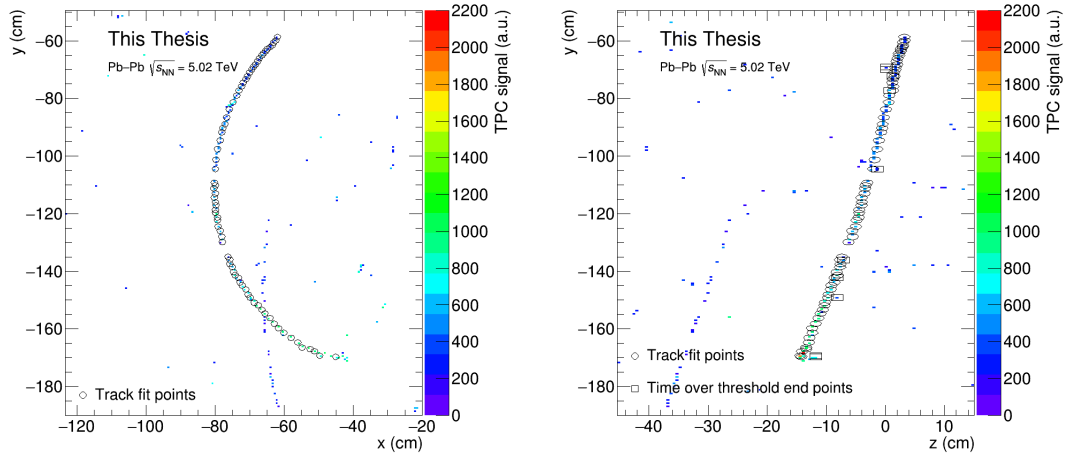


Figure 6.4.: Projection of the TPC signal of a selected track in the $x - y$ and $z - y$ plane. See text for details.

Figure 6.4 shows the $x - y$ and $z - y$ projections of clusters that belong to a selected track. The shown cluster positions represent the central positions of clusters. The colour indicates the highest signal amplitude within the cluster. It exceeds 1000 if two clusters are projected into the same bin, which is the case in Fig. 6.4 (right) at the lower end of the track. The increase of the signal, and thus $-dE/dx$, towards the end of the track in the bottom half of Fig. 6.4 is clearly visible. Figure 6.4 (right) also shows that at the end of the track the signal appears to be smeared out in the z direction, which is interpreted as TOT.

To calibrate the $-dE/dx$ measurement based on the charge deposition, it is necessary to infer the energy loss by means that are independent of the $-dE/dx$ measurement. This is achieved by deducing the particle species of a track using geometrical observables.

The ratio p_T/Z , where Z is the charge of a particle, can be determined via the track curvature, which is estimated from manually selected track points. These points are encircled in Fig. 6.4. The corresponding x, y, z coordinates are fit with a helical track template¹. The ratio p_T/Z is estimated using the relation $p_T/Z = Br$, where B is the strength of the magnetic field along the beam direction and r the curvature radius of the track. The fit for p_T/Z is performed at a given track point using in addition the ten track points before and the ten track points afterwards. No fits are performed for track points within a distance of less than ten track points from the track start or track end point.

To identify the particle species a further quantity is necessary. Since the tracks

¹Using the class AliRoot/STEER/STEER/AliRiemann.h.

under consideration stop in the TPC one can extract the remaining range for a track at each point. This quantity can also be extracted from the coordinates of the manually selected track points.

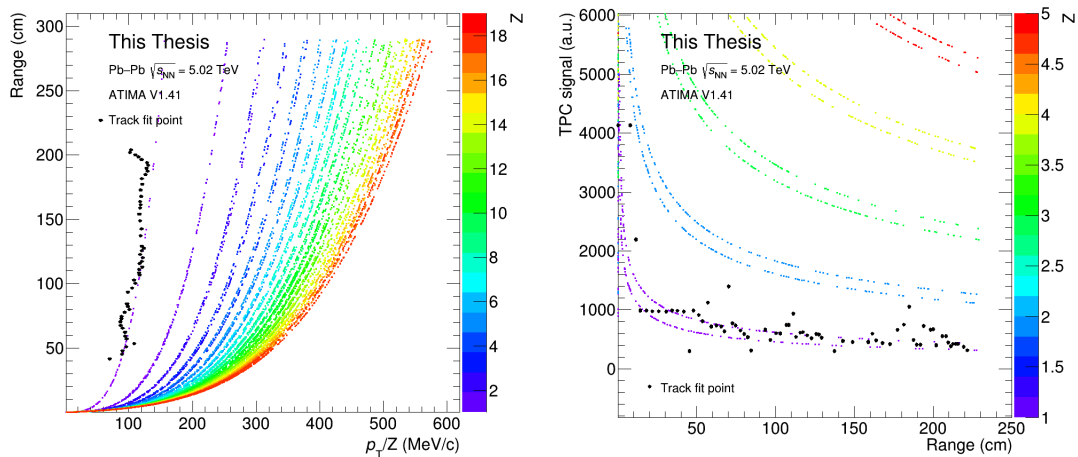


Figure 6.5.: Left: Comparison of p_T/Z and the remaining range values to expectations of nuclei of varying charge Z and mass (not indicated). Right: Comparison of the measured TPC signal and the remaining range to expectations of various nuclei. Expectations are based on [149].

Figure 6.5 (left) shows the comparison of the found values of p_T/Z and the remaining range of the track points to the values expected for nuclei of various charges (Z) and masses (not indicated) [149]. The track under consideration can be identified rather unambiguously as a proton ($Z = 1$).

The comparison of the measured TPC signal and the expected stopping power for a proton with a given remaining range is shown in Fig. 6.5 (right). The shown TPC signal is the maximum signal amplitude in the cluster which is selected as a track point. To deal with TOT in Fig. 6.4 (right), the row of bins in z direction which contains a selected cluster and the two adjacent bin rows (i.e. the ones above and below), are scanned in the direction which would be expected for TOT (i.e. towards $z = 0$) for further clusters within 10 centimeters. If a cluster is found, the corresponding signal amplitude is added to the one associated to the original track point and the search continues for another 10 cm. Clusters which are associated to track points by this procedure are framed in squares in Fig. 6.4 (right). They indicate the duration of a potential TOT signal. Along the track such clusters are found several times but presumably they do not indicate a TOT signal but are caused by noise or other tracks. These misidentifications cause the peaks at large remaining range in Fig. 6.5 (right). Figure 6.5 (right) further shows that the

TPC signal amplitude does not continue to rise with $-dE/dx$ as the track has less than 50 cm range left, but remains constant at the maximum signal value of 1000. Below 10 centimeters of range the TPC signal amplitude jumps to a value just above 2000, indicating that TOT clusters are found. Around the Bragg peak the signal amplitude reaches values just above 4000. That the measured signal amplitude in Fig. 6.5 (right) rises before the expectation when approaching the track end point is attributed to the finite resolution of the track points and the resulting uncertainty of the track end point position.

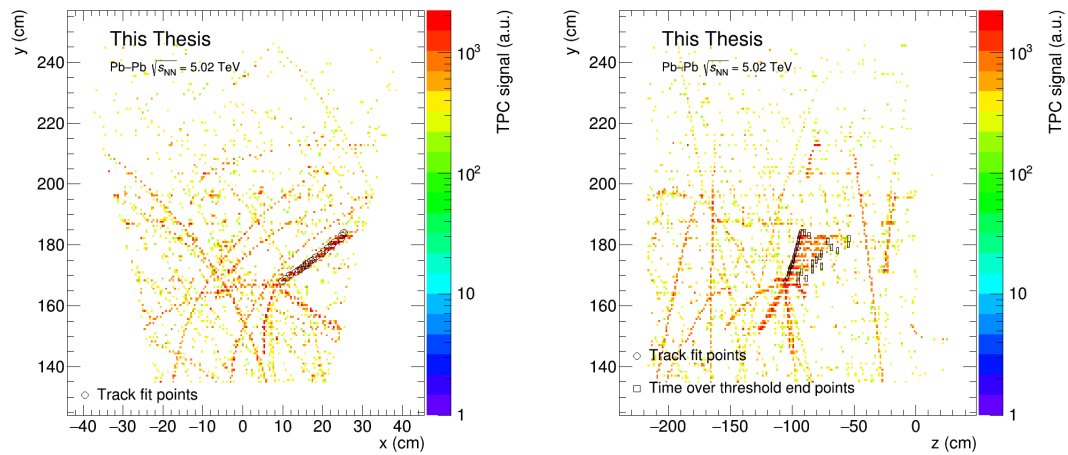


Figure 6.6.: Projection of the TPC signal of a fragment candidate in the $x - y$ and $z - y$ plane. See text for details.

The example of the proton track suggests that stopping power values well above the usual range can be measured in the TPC raw data. The proton $-dE/dx$ in the Bragg peak is still roughly an order of magnitude lower than the typical values for a magnetic monopole (see Fig. 6.2). Nuclear fragments heavier than a proton are needed to learn about the TPC response in this stopping power realm. The aforementioned 650 events from raw data are used for this purpose. The events are inspected visually for potential candidates of heavy fragments.

Figure 6.6 shows the clusters of a selected candidate event. The $x - y$ (left) and $z - y$ (right) projections exhibit signs of a nuclear reaction, i.e. several fragments originating from the same point. The track corresponding to a heavy fragment, indicated by the encircled cluster positions, can be identified by the substantial TOT in the $z - y$ projection. Due to the short track length, a track identification using p_T/Z and the remaining range is not possible. However, based on the found TOT to $-dE/dx$ correspondence in the case of the proton track, one can perform an analysis of the TOT signal for this track to identify it via its $-dE/dx$.

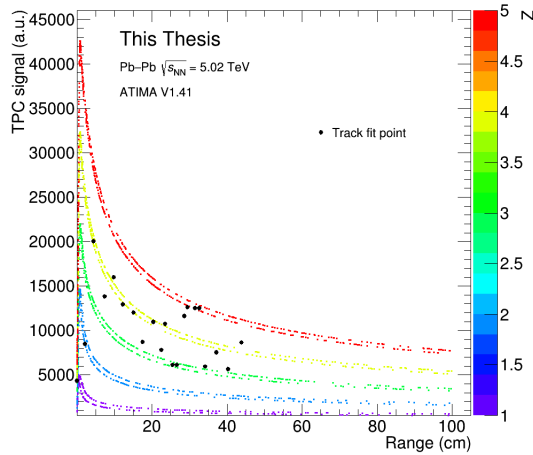


Figure 6.7.: Comparison of the measured TPC signal and the remaining range to expectations of various nuclei of varying charge Z and mass (not indicated). Expectations are based on [149].

Figure 6.7 shows the expected TPC signal for nuclei with various charges Z and isotopes with mass numbers of $A = 2Z$ and $A = 2Z - 1$. The different isotopes cannot be distinguished. The fragment is most likely of charge $Z = 4 (\pm 1)$.

6.4. Discussion and outlook

The TPC is not calibrated for tracks with stopping powers that are expected for a magnetic monopole. Using the TPC signal in the Bragg peak of nuclear fragments allows the investigation of this $-dE/dx$ regime. The examples of the proton track and the heavier nuclear fragment demonstrate the feasibility of a high $-dE/dx$ calibration under real data taking conditions.

Refining the event preselection, the tracking and development of an automated track candidate selection should allow future studies to find more heavy fragments and to establish an understanding of the TPC signal in conditions as expected for a monopole. Robust search criteria for HIPs, like e.g. monopoles, can then be derived from the results of the high $-dE/dx$ calibration. Based on the TPC signal associated to the Bragg peak of heavy fragments, a lower bound for the TOT expected from the monopole can be defined. The search criterion for magnetic monopoles could require this TOT in a certain number of consecutive pad rows in a TPC sector. If the search aims, for instance, at traversing monopoles one

could demand that this TOT is measured in all or at least most pad rows. The only background for such a search should be the very unlikely case of extremely high fragment density in a TPC sector. It is expected that a signal region can be defined, which is practically background free.

To complete a search for magnetic monopoles, simulations are needed to estimate the monopole detection efficiencies in the phase space of the monopole kinematics, mass and charge. The GEANT4 implementation of magnetic monopoles [150] was made available in the ALICE simulation framework for this purpose. It allows simulations of the propagation of magnetic monopoles through a realistic model of the ALICE detector. These simulations were cross checked against the results in [96], like e.g. Fig. 6.1 [151]. Once the search is carried out, the corresponding efficiencies could be estimated from these simulations.

Interpretation of the search results in terms of a monopole mass limit would require that monopole production cross sections are extracted for HICs based on the models discussed in Section 3.4.1. There is ongoing effort in the theory community to achieve this goal. Without the input of the monopole production cross section a search could, nonetheless, be interpreted in terms of the first limits on the magnetic monopole production cross section in HICs in a fiducial phase space region (similarly to [102]).

7. Conclusion

This thesis presents a machine learning based approach to the rejection of photon-conversion background, which is one of the most important and critical steps in the analysis of dielectrons in heavy-ion collisions. A strategy for data-driven performance evaluation and optimisation of the signal selection is introduced. The superiority of this method with respect to conventional photon-conversion rejection is demonstrated.

Employing these new tools, Pb–Pb collisions at $\sqrt{s_{\text{NN}}} = 5.02$ TeV are analysed. The results show evidence for dielectron photo-production in heavy-ion collisions at LHC energies. A comparison to corresponding model calculations points to a rather good, but imperfect overall agreement. For a more rigorous comparison detector resolution effects will have to be taken into account in the models. Motivated by several theoretical proposals, the analysis is carried out for dielectrons in and out of the event plane. Despite large statistical uncertainties, the results could be interpreted as sign for a larger dielectron photo-production yield in the spectra that are based on tracks in the event plane.

The second project of this thesis deals with the design and demonstration of a strategy for a magnetic monopole search with ALICE. Due to the exotic properties of magnetic monopoles, the expected detector response to these hypothetical particles cannot be inferred unambiguously from standard detector calibrations. This problem is overcome by exploiting the similarity in the energy deposition of stopping nuclear fragments and magnetic monopoles. A search for these fragments is carried out on raw data of the ALICE Time Projection Chamber. Candidate tracks are analysed using a custom track fitting procedure. The particle species associated to the tracks is determined by the comparison of the track parameters to calculated expectation values. These results can be regarded as a successful proof of concept for a monopole search with the ALICE detector. Extending these studies should allow the first magnetic monopole search in heavy-ion collisions at the LHC. The results of such searches could provide the experimental basis for the most stringent, general mass limit on magnetic monopoles.

A. Kinematic variables

This section provides the definitions of the kinematical variables used in this thesis. In the following natural units are used, i.e. $c = 1$.

In relativity the kinematics of a particle is defined by its four-momentum, which is determined by the energy E and the three-momentum vector $\vec{p} = (p_x, p_y, p_z)$ associated to the particle:

$$p = (E, p_x, p_y, p_z).$$

Based on this four-vector the following particle properties are defined:

- Invariant mass m_0 : $p^2 = E^2 - \vec{p}^2 = m_0^2$
- Transverse momentum: $p_T = \sqrt{p_x^2 + p_y^2}$
- Transverse mass: $m_T = \sqrt{p_T^2 + m_0^2}$
- Rapidity: $y = \frac{1}{2} \ln \frac{E+p_z}{E-p_z} = \operatorname{arctanh} \frac{p_z}{E}$.

The determination of y requires information on E or the particle species, which implies m_0 . In experiments this information is often not available. For highly relativistic particles ($|\vec{p}| \gg m_0$) this is not problematic. In these cases the rapidity y along the beam axis, which usually defines the z -axis, can be approximated by the pseudorapidity η :

$$\eta = -\ln \tan \frac{\theta}{2},$$

where θ is the angle between the beam axis and \vec{p} . The transverse direction ($\theta = \pi/2$) corresponds to $\eta = 0$, $\theta = \pi/4$ to $\eta = 0.88$ and $\theta \rightarrow 0$ to $\eta \rightarrow \infty$.

For pairs of particles, like dielectrons, the pair four-momentum $p_{1,2}$ is defined via the sum of four-momenta (p_1 and p_2) of the two individual particles (denote by the indices 1 and 2) as:

$$p_{1,2} = p_1 + p_2.$$

Using this definition the same quantities as in the single particle case above can be defined for pairs.

Bibliography

- [1] S. S. Walter Greiner and E. Stein, *Quantum Chromodynamics*, 2053-2563. Springer, Berlin, Heidelberg, 2006, <https://doi.org/10.1007/978-3-540-48535-3>. (Cited on page 4, 5, 26)
- [2] S. Sarkar, H. Satz and B. Sinha, *The physics of the quark-gluon plasma*, vol. 785. Springer-Verlag Berlin Heidelberg, 2010, 10.1007/978-3-642-02286-9. (Cited on page 4, 6, 7, 11, 21, 24, 81)
- [3] H. Satz, *Extreme States of Matter in Strong Interaction Physics*, vol. 945. Springer-Verlag Berlin Heidelberg, 2018, 10.1007/978-3-319-71894-1. (Cited on page 4, 6, 10, 21)
- [4] D. J. Gross and F. Wilczek, *Ultraviolet Behavior of Non-Abelian Gauge Theories*, *Phys. Rev. Lett.* **30** (1973) 1343. (Cited on page 4)
- [5] H. D. Politzer, *Reliable Perturbative Results for Strong Interactions?*, *Phys. Rev. Lett.* **30** (1973) 1346. (Cited on page 4)
- [6] S. Bethke, *Determination of the QCD coupling α_s* , *J. Phys.* **G26** (2000) R27 [[arXiv:hep-ex/0004021](https://arxiv.org/abs/hep-ex/0004021)]. (Cited on page 5)
- [7] A. K. Chaudhuri, *A short course on Relativistic Heavy Ion Collisions*. IOPP, 2014, 10.1088/978-0-750-31060-4, [[arXiv:1207.7028](https://arxiv.org/abs/1207.7028)]. (Cited on page 5, 9)
- [8] N. Cabibbo and G. Parisi, *Exponential Hadronic Spectrum and Quark Liberation*, *Phys. Lett.* **59B** (1975) 67. (Cited on page 6)
- [9] J. C. Collins and M. J. Perry, *Superdense Matter: Neutrons Or Asymptotically Free Quarks?*, *Phys. Rev. Lett.* **34** (1975) 1353. (Cited on page 6)
- [10] P. Braun-Munzinger, V. Koch, T. Schäfer and J. Stachel, *Properties of hot and dense matter from relativistic heavy ion collisions*, *Phys. Rept.* **621**

(2016) 76 [arXiv:1510.00442]. (Cited on page 6, 7, 8, 9, 12)

- [11] T. Boeckel and J. Schaffner-Bielich, *A little inflation at the cosmological QCD phase transition*, *Phys. Rev.* **D85** (2012) 103506 [arXiv:1105.0832]. (Cited on page 7)
- [12] C. Schmidt and S. Sharma, *The phase structure of QCD*, *J. Phys.* **G44** (2017) 104002 [arXiv:1701.04707]. (Cited on page 7, 9, 19)
- [13] I. Ya. Pomeranchuk, *On the theory of multiple particle production in a single collision*, *Dokl. Akad. Nauk Ser. Fiz.* **78** (1951) 889. (Cited on page 7)
- [14] R. Hagedorn, *Statistical thermodynamics of strong interactions at high-energies*, *Nuovo Cim. Suppl.* **3** (1965) 147. (Cited on page 7)
- [15] J. Rafelski, ed., *Melting Hadrons, Boiling Quarks - From Hagedorn Temperature to Ultra-Relativistic Heavy-Ion Collisions at CERN*. Springer, 2016, 10.1007/978-3-319-17545-4. (Cited on page 8, 12)
- [16] M. E. Peskin and D. V. Schroeder, *An Introduction to quantum field theory*. Addison-Wesley, Reading, USA, 1995. (Cited on page 8)
- [17] V. Koch, *Aspects of chiral symmetry*, *Int. J. Mod. Phys.* **E6** (1997) 203 [arXiv:nucl-th/9706075]. (Cited on page 9)
- [18] T. Dahms, *Dilepton spectra in p+p and Au+Au collisions at RHIC*, arXiv:0810.3040. (Cited on page 9, 74, 75)
- [19] P. Foka and M. A. Janik, *An overview of experimental results from ultra-relativistic heavy-ion collisions at the CERN LHC: Bulk properties and dynamical evolution*, *Rev. Phys.* **1** (2016) 154 [arXiv:1702.07233]. (Cited on page 9)
- [20] Y. Nambu and G. Jona-Lasinio, *Dynamical Model of Elementary Particles Based on an Analogy with Superconductivity. I*, *Phys. Rev.* **122** (1961) 345. (Cited on page 9)
- [21] Y. Nambu and G. Jona-Lasinio, *Dynamical Model of Elementary Particles Based on an Analogy with Superconductivity. II*, *Phys. Rev.* **124** (1961) 246. (Cited on page 9)
- [22] A. Andronic, P. Braun-Munzinger, K. Redlich and J. Stachel, *Decoding the*

phase structure of QCD via particle production at high energy, Nature **561** (2018) 321 [arXiv:1710.09425]. (Cited on page 10)

- [23] E. Shuryak, *Strongly coupled quark-gluon plasma in heavy ion collisions, Rev. Mod. Phys.* **89** (2017) 035001 [arXiv:1412.8393]. (Cited on page 11)
- [24] J. D. Bjorken, *Highly Relativistic Nucleus-Nucleus Collisions: The Central Rapidity Region, Phys. Rev.* **D27** (1983) 140. (Cited on page 12)
- [25] N. Armesto and E. Scapparini, *Heavy-ion collisions at the Large Hadron Collider: a review of the results from Run 1, Eur. Phys. J. Plus* **131** (2016) 52 [arXiv:1511.02151]. (Cited on page 13)
- [26] R. Snellings, *Collective Expansion at the LHC: selected ALICE anisotropic flow measurements, J. Phys.* **G41** (2014) 124007 [arXiv:1408.2532]. (Cited on page 13)
- [27] M. L. Miller, K. Reygers, S. J. Sanders and P. Steinberg, *Glauber modeling in high energy nuclear collisions, Ann. Rev. Nucl. Part. Sci.* **57** (2007) 205 [arXiv:nucl-ex/0701025]. (Cited on page 14)
- [28] ALICE Collaboration, *Centrality determination in heavy ion collisions, ALICE-PUBLIC-2018-011* (2018) . (Cited on page 14, 15)
- [29] M. Martenson, *Elliptic flow of π , K, p and Φ in Pb-Pb collisions at the Large Hadron Collider*. Bachelor Thesis, Lund University, 2015. (Cited on page 16)
- [30] ALICE Collaboration, *Performance of the ALICE Experiment at the CERN LHC, Int. J. Mod. Phys.* **A29** (2014) 1430044 [arXiv:1402.4476]. (Cited on page 16, 50, 51, 62, 64)
- [31] I. Selyuzhenkov and S. Voloshin, *Effects of non-uniform acceptance in anisotropic flow measurement, Phys. Rev.* **C77** (2008) 034904 [arXiv:0707.4672]. (Cited on page 16)
- [32] V. Gonzales, *"QnCorrections framework: Performance and usage", Talk at ALICE Mini Week, 4.10.2016*. (Cited on page 17)
- [33] A. Caliva, *Low-mass dielectron measurement in Pb-Pb collisions at $\sqrt{s_{NN}} = 2.76$ TeV with ALICE at the LHC*. Doctoral Thesis, Utrecht University, 2017. (Cited on page 18)

- [34] P. M. Hohler and R. Rapp, *Is ρ -Meson Melting Compatible with Chiral Restoration?*, *Phys. Lett.* **B731** (2014) 103 [arXiv:1311.2921]. (Cited on page 19)
- [35] D. Adamova et al., *Modification of the rho-meson detected by low-mass electron-positron pairs in central Pb-Au collisions at 158-A-GeV/c*, *Phys. Lett.* **B666** (2008) 425 [arXiv:nucl-ex/0611022]. (Cited on page 19)
- [36] S. Damjanovic et al., *NA60 results on the ρ spectral function in In-In collisions*, *Nucl. Phys.* **A783** (2007) 327 [arXiv:nucl-ex/0701015]. (Cited on page 19, 22, 23, 24)
- [37] R. Rapp, J. Wambach and H. van Hees, *The Chiral Restoration Transition of QCD and Low Mass Dileptons*, arXiv:0901.3289. (Cited on page 19)
- [38] Hans J. Specht for the NA60 Collaboration, *Thermal Dileptons from Hot and Dense Strongly Interacting Matter*, arXiv:1011.0615. (Cited on page 20)
- [39] PHENIX Collaboration, *Dielectron production in Au + Au collisions at $\sqrt{s_{NN}} = 200$ GeV*, *Phys. Rev. C* **93** (2016) 014904. (Cited on page 20)
- [40] STAR collaboration, *Dielectron Mass Spectra from Au+Au Collisions at $\sqrt{s_{NN}} = 200$ GeV*, *Phys. Rev. Lett.* **113** (2014) 022301 [arXiv:1312.7397]. (Cited on page 20, 21)
- [41] STAR Collaboration, *Energy dependence of acceptance-corrected dielectron excess mass spectrum at mid-rapidity in Au+Au collisions at $\sqrt{s_{NN}} = 19.6$ and 200 GeV*, *Physics Letters B* **750** (2015) 64 . (Cited on page 20)
- [42] ALICE Collaboration, *Measurement of dielectron production in central Pb-Pb collisions at $\sqrt{s_{NN}} = 2.76$ TeV*, *Phys. Rev.* **C99** (2019) 024002 [arXiv:1807.00923]. (Cited on page 21, 23)
- [43] R. Rapp and H. van Hees, *Thermal Electromagnetic Radiation in Heavy-Ion Collisions*, *Eur. Phys. J.* **A52** (2016) 257 [arXiv:1608.05279]. (Cited on page 20)
- [44] F. Antinori et al., *Thoughts on opportunities in high-energy nuclear collisions*, arXiv:1903.04289. (Cited on page 20)
- [45] N. M. Kroll and W. Wada, *Internal pair production associated with the emission of high-energy gamma rays*, *Phys. Rev.* **98** (1955) 1355. (Cited on

page 21, 81)

- [46] PHENIX Collaboration, *Enhanced production of direct photons in Au+Au collisions at $\sqrt{s_{NN}} = 200$ GeV and implications for the initial temperature*, *Phys. Rev. Lett.* **104** (2010) 132301 [arXiv:0804.4168]. (Cited on page 22, 23)
- [47] Z. Citron, A. Dainese, J. F. Grosse-Oetringhaus, J. M. Jowett, Y. J. Lee, U. A. Wiedemann et al., *Future physics opportunities for high-density QCD at the LHC with heavy-ion and proton beams*, arXiv:1812.06772. (Cited on page 24)
- [48] G. Baur, K. Hencken and D. Trautmann, *Electron-Positron Pair Production in Relativistic Heavy Ion Collisions*, arXiv:0706.0654. (Cited on page 25, 27)
- [49] G. Baur, K. Hencken, D. Trautmann, S. Sadovsky and Y. Kharlov, *Coherent $\gamma\gamma$ and γA interactions in very peripheral collisions at relativistic ion colliders*, *Physics Reports* **364** (2002) 359 . (Cited on page 25, 37)
- [50] G. Breit and J. A. Wheeler, *Collision of Two Light Quanta*, *Phys. Rev.* **46** (1934) 1087. (Cited on page 25)
- [51] R. Ruffini, G. Vereshchagin and S.-S. Xue, *Electron-positron pairs in physics and astrophysics: from heavy nuclei to black holes*, arXiv:0910.0974. (Cited on page 25)
- [52] E. J. Williams, *Nature of the high-energy particles of penetrating radiation and status of ionization and radiation formulae*, *Phys. Rev.* **45** (1934) 729. (Cited on page 25)
- [53] C. F. v. Weizsäcker, *Ausstrahlung bei Stößen sehr schneller Elektronen*, *Zeitschrift für Physik* **88** (1934) 612. (Cited on page 25)
- [54] A. J. Baltz, *The Physics of Ultraperipheral Collisions at the LHC*, *Phys. Rept.* **458** (2008) 1 [arXiv:0706.3356]. (Cited on page 26)
- [55] CMS Collaboration, *Coherent J/ψ photoproduction in ultra-peripheral PbPb collisions at $\sqrt{s_{NN}} = 2.76$ TeV with the CMS experiment*, *Phys. Lett. B* **772** (2017) 489 [arXiv:1605.06966]. (Cited on page 26)
- [56] ATLAS Collaboration, *Electromagnetic processes in ultra-peripheral Pb+Pb collisions with ATLAS*, *Nucl. Phys. A* **967** (2017) 281. (Cited on page 26)

- [57] W. Zha, L. Ruan, Z. Tang, Z. Xu and S. Yang, *Coherent photo-produced J/ψ and dielectron yields in isobaric collisions*, arXiv:1810.02064. (Cited on page 26)
- [58] ALICE Collaboration, *Charmonium and e^+e^- pair photoproduction at mid-rapidity in ultra-peripheral Pb-Pb collisions at $\sqrt{s_{NN}}=2.76$ TeV*, *Eur. Phys. J.* **C73** (2013) 2617 [arXiv:1305.1467]. (Cited on page 26)
- [59] STAR Collaboration, *Production of e^+e^- pairs accompanied by nuclear dissociation in ultra-peripheral heavy ion collision*, *Phys. Rev.* **C70** (2004) 031902 [arXiv:nucl-ex/0404012]. (Cited on page 26)
- [60] ALICE Collaboration, *Measurement of an excess in the yield of J/ψ at very low p_T in Pb-Pb collisions at $\sqrt{s_{NN}} = 2.76$ TeV*, *Phys. Rev. Lett.* **116** (2016) 222301 [arXiv:1509.08802]. (Cited on page 27, 28)
- [61] STAR Collaboration, *Observation of excess J/ψ yield at very low transverse momenta in Au+Au collisions at $\sqrt{s_{NN}} = 200$ GeV and U+U collisions at $\sqrt{s_{NN}} = 193$ GeV*, arXiv:1904.11658. (Cited on page 28, 29, 35)
- [62] M. Klusek-Gawenda and A. Szczurek, *Photoproduction of J/ψ mesons in peripheral and semicentral heavy ion collisions*, *Phys. Rev.* **C93** (2016) 044912 [arXiv:1509.03173]. (Cited on page 28)
- [63] W. Zha, S. R. Klein, R. Ma, L. Ruan, T. Todoroki, Z. Tang et al., *Coherent J/ψ photoproduction in hadronic heavy-ion collisions*, *Phys. Rev.* **C97** (2018) 044910 [arXiv:1705.01460]. (Cited on page 28, 34, 35)
- [64] X. Zhao and R. Rapp, *Medium Modifications and Production of Charmonia at LHC*, *Nucl. Phys.* **A859** (2011) 114 [arXiv:1102.2194]. (Cited on page 28)
- [65] Y.-p. Liu, Z. Qu, N. Xu and P.-f. Zhuang, *J/ψ Transverse Momentum Distribution in High Energy Nuclear Collisions at RHIC*, *Phys. Lett.* **B678** (2009) 72 [arXiv:0901.2757]. (Cited on page 28, 29)
- [66] ALICE Collaboration, *J/ψ suppression at forward rapidity in Pb-Pb collisions at $\sqrt{s_{NN}} = 5.02$ TeV*, *Phys. Lett.* **B766** (2017) 212 [arXiv:1606.08197]. (Cited on page 28)
- [67] ALICE Collaboration, *Centrality, rapidity and transverse momentum dependence of J/ψ suppression in Pb-Pb collisions at $\sqrt{s_{NN}}=2.76$ TeV*,

Phys. Lett. **B734** (2014) 314 [arXiv:1311.0214]. (Cited on page 28)

- [68] ALICE Collaboration, *Inclusive, prompt and non-prompt J/ψ production at mid-rapidity in Pb-Pb collisions at $\sqrt{s_{NN}} = 2.76$ TeV*, *JHEP* **07** (2015) 051 [arXiv:1504.07151]. (Cited on page 28)
- [69] X. Zhao and R. Rapp, *Charmonium in Medium: From Correlators to Experiment*, *Phys. Rev.* **C82** (2010) 064905 [arXiv:1008.5328]. (Cited on page 29)
- [70] ATLAS Collaboration, *Observation of centrality-dependent acoplanarity for muon pairs produced via two-photon scattering in Pb+Pb collisions at $\sqrt{s_{NN}} = 5.02$ TeV with the ATLAS detector*, *Phys. Rev. Lett.* **121** (2018) 212301 [arXiv:1806.08708]. (Cited on page 29, 30, 37)
- [71] S. R. Klein, J. Nystrand, J. Seger, Y. Gorbunov and J. Butterworth, *STARlight: A Monte Carlo simulation program for ultra-peripheral collisions of relativistic ions*, *Comput. Phys. Commun.* **212** (2017) 258 [arXiv:1607.03838]. (Cited on page 29, 31)
- [72] STAR Collaboration, *Low- p_T e^+e^- Pair Production in Au + Au Collisions at $\sqrt{s_{NN}} = 200$ GeV and U + U Collisions at $\sqrt{s_{NN}} = 193$ GeV at STAR*, *Phys. Rev. Lett.* **121** (2018) 132301 [arXiv:1806.02295]. (Cited on page 30, 31, 32, 33, 37)
- [73] S. R. Klein, *Two-photon production of dilepton pairs in peripheral heavy ion collisions*, *Phys. Rev. C* **97** (2018) 054903 [arXiv:1801.04320]. (Cited on page 31, 35, 37)
- [74] W. Zha, L. Ruan, Z. Tang, Z. Xu and S. Yang, *Coherent lepton pair production in hadronic heavy ion collisions*, *Physics Letters B* **781** (2018) 182 [arXiv:1804.01813]. (Cited on page 31, 35)
- [75] X.-G. Huang, *Electromagnetic fields and anomalous transports in heavy-ion collisions — A pedagogical review*, arXiv:1509.04073. (Cited on page 32)
- [76] M. Klusek-Gawenda, R. Rapp, W. Schäfer and A. Szczurek, *Dilepton radiation in heavy-ion collisions at small transverse momentum*, *Physics Letters B* **790** (2019) 339 [arXiv:1809.07049]. (Cited on page 35, 36, 37, 38)
- [77] W. Zha, J. D. Brandenburg, Z. Tang and Z. Xu, *Initial*

transverse-momentum broadening of Breit-Wheeler process in relativistic heavy-ion collisions, arXiv:1812.02820v2. (Cited on page 37, 38, 39, 40)

- [78] S. Klein, A. H. Mueller, B.-W. Xiao and F. Yuan, *Acoplanarity of Lepton Pair to Probe the Electromagnetic Property of Quark Matter*, arXiv:1811.05519. (Cited on page 38)
- [79] T. Song, W. Cassing, P. Moreau and E. Bratkovskaya, *Discrepancy in low transverse momentum dileptons from relativistic heavy-ion collisions*, *Phys. Rev. C* **98** (2018) 041901 [arXiv:1806.09377]. (Cited on page 39)
- [80] A. Rajantie, *Introduction to Magnetic Monopoles*, *Contemp. Phys.* **53** (2012) 195 [arXiv:1204.3077]. (Cited on page 40, 41, 43, 46)
- [81] L. Alvarez-Gaumé and M. A. Vázquez-Mozo, *An Invitation to Quantum Field Theory*. Springer-Verlag Berlin Heidelberg, 2012. (Cited on page 41)
- [82] Y. Aharonov and D. Bohm, *Significance of Electromagnetic Potentials in the Quantum Theory*, *Phys. Rev.* **115** (1959) 485. (Cited on page 41)
- [83] R. Heras, *Dirac quantisation condition: a comprehensive review*, *Contemp. Phys.* **59** (2018) 331 [arXiv:1810.13403]. (Cited on page 41, 42, 43)
- [84] P. A. M. Dirac, *Quantised singularities in the electromagnetic field., Proc. Roy. Soc. Lond.* **A133** (1931) 60. (Cited on page 41, 43)
- [85] O. Gould, D. L. J. Ho and A. Rajantie, *Towards Schwinger production of magnetic monopoles in heavy-ion collisions*, *Phys. Rev.* **D100** (2019) 015041 [arXiv:1902.04388]. (Cited on page 43, 44, 45)
- [86] J. Ellis, N. E. Mavromatos and T. You, *The Price of an Electroweak Monopole*, *Phys. Lett.* **B756** (2016) 29 [arXiv:1602.01745]. (Cited on page 43)
- [87] Particle Data Group Collaboration, *Review of Particle Physics*, *Phys. Rev. D* **98** (2018) 030001. (Cited on page 43, 45, 46, 47, 48, 52, 81, 83)
- [88] ATLAS Collaboration, *Search for magnetic monopoles and stable high-electric-charge objects in 13 TeV proton-proton collisions with the ATLAS detector*, arXiv:1905.10130. (Cited on page 43, 47, 48)
- [89] S. Baines, N. E. Mavromatos, V. A. Mitsou, J. L. Pinfold and A. Santra, *Monopole production via photon fusion and Drell-Yan processes:*

MadGraph implementation and perturbativity via velocity-dependent coupling and magnetic moment as novel features, *Eur. Phys. J.* **C78** (2018) 966 [arXiv:1808.08942]. (Cited on page 44)

- [90] R. Heras, *Comment on "Monopole production via photon fusion and Drell-Yan processes: MadGraph implementation and perturbativity via velocity-dependent coupling and magnetic moment as novel features"*, arXiv:1902.11138. (Cited on page 44)
- [91] J. T. Reis and W. K. Sauter, *Production of magnetic monopoles and monopolium in peripheral collisions*, *Phys. Rev.* **D96** (2017) 075031 [arXiv:1707.04170]. (Cited on page 44)
- [92] A. Rajantie, *Monopole-antimonopole pair production by magnetic fields*, in *Topological avatars of new physics London, United Kingdom, March 4-5, 2019*, 2019, arXiv:1907.05745. (Cited on page 44, 45)
- [93] O. Gould and A. Rajantie, *Magnetic monopole mass bounds from heavy ion collisions and neutron stars*, *Phys. Rev. Lett.* **119** (2017) 241601 [arXiv:1705.07052]. (Cited on page 44)
- [94] Y. D. He, *Search for a Dirac magnetic monopole in high-energy nucleus-nucleus collisions*, *Phys. Rev. Lett.* **79** (1997) 3134. (Cited on page 44)
- [95] S. P. Ahlen, *Stopping Power Formula for Magnetic Monopoles*, *Phys. Rev.* **D17** (1978) 229. (Cited on page 45)
- [96] A. De Roeck, A. Katre, P. Mermoud, D. Milstead and T. Sloan, *Sensitivity of LHC Experiments to Exotic Highly Ionising Particles*, *Eur. Phys. J.* **C72** (2012) 1985 [arXiv:1112.2999]. (Cited on page 45, 46, 52, 115, 116, 124)
- [97] MoEDAL Collaboration, *Search for magnetic monopoles with the MoEDAL prototype trapping detector in 8 TeV proton-proton collisions at the LHC*, *JHEP* **08** (2016) 067 [arXiv:1604.06645]. (Cited on page 47, 116)
- [98] MoEDAL Collaboration, *Search for Magnetic Monopoles with the MoEDAL Forward Trapping Detector in 13 TeV Proton-Proton Collisions at the LHC*, *Phys. Rev. Lett.* **118** (2017) 061801 [arXiv:1611.06817]. (Cited on page 47)
- [99] MoEDAL Collaboration, *Search for magnetic monopoles with the MoEDAL*

forward trapping detector in 2.11 fb^{-1} of 13 TeV proton-proton collisions at the LHC, *Phys. Lett.* **B782** (2018) 510 [arXiv:1712.09849]. (Cited on page 47)

- [100] MoEDAL Collaboration, *Magnetic Monopole Search with the Full MoEDAL Trapping Detector in 13 TeV pp Collisions Interpreted in Photon-Fusion and Drell-Yan Production*, *Phys. Rev. Lett.* **123** (2019) 021802 [arXiv:1903.08491]. (Cited on page 47, 48)
- [101] ATLAS Collaboration, *Search for magnetic monopoles in $\sqrt{s} = 7 \text{ TeV}$ pp collisions with the ATLAS detector*, *Phys. Rev. Lett.* **109** (2012) 261803 [arXiv:1207.6411]. (Cited on page 47)
- [102] ATLAS Collaboration, *Search for magnetic monopoles and stable particles with high electric charges in 8 TeV pp collisions with the ATLAS detector*, *Phys. Rev.* **D93** (2016) 052009 [arXiv:1509.08059]. (Cited on page 47, 124)
- [103] ALICE Collaboration, *The ALICE experiment at the CERN LHC*, *JINST* **3** (2008) S08002. (Cited on page 49)
- [104] ALICE Collaboration, “3D ALICE Schematic RUN2 - with Description.” <https://alice-figure.web.cern.ch/node/11218>, Accessed: 10.10.2019. (Cited on page 50)
- [105] G. Dellacasa et al., *ALICE: Technical design report of the time projection chamber*, *CERN-OPEN-2000-183*, *CERN-LHCC-2000-001* (2000) . (Cited on page 50)
- [106] ALICE Collaboration, *Determination of the event collision time with the ALICE detector at the LHC*, *Eur. Phys. J. Plus* **132** (2017) 99 [arXiv:1610.03055]. (Cited on page 51)
- [107] E. Botta, *Particle identification performance at ALICE*, arXiv:1709.00288. (Cited on page 53)
- [108] F. Carnesecchi, *Performance of the ALICE Time-Of-Flight detector at the LHC*, *JINST* **14** (2019) C06023 [arXiv:1806.03825]. (Cited on page 53)
- [109] ALICE Collaboration, *Particle identification in ALICE: a Bayesian approach*, *Eur. Phys. J. Plus* **131** (2016) 168 [arXiv:1602.01392]. (Cited on page 54)

- [110] C. Klein, *Dielectron Production in Pb–Pb Collisions at $\sqrt{s_{NN}} = 5.02$ TeV with ALICE*. Doctoral Thesis, Johann Wolfgang Goethe University of Frankfurt, To be published. (Cited on page 54, 83)
- [111] X.-N. Wang and M. Gyulassy, *HIJING: A Monte Carlo model for multiple jet production in p p, p A and A A collisions*, *Phys. Rev.* **D44** (1991) 3501. (Cited on page 56, 87)
- [112] T. Sjöstrand, S. Mrenna and P. Skands, *PYTHIA 6.4 physics and manual*, *Journal of High Energy Physics* **2006** (2006) 026 [arXiv:0603175]. (Cited on page 56, 81, 82)
- [113] R. Brun, F. Bruyant, M. Maire, A. C. McPherson and P. Zancarini, *GEANT3, CERN-DD-EE-84-1* (1987) . (Cited on page 56)
- [114] R. Fruhwirth, *Application of Kalman filtering to track and vertex fitting*, *Nucl. Instrum. Meth.* **A262** (1987) 444. (Cited on page 62)
- [115] A. Geron, *Hands-On Machine Learning with Scikit-Learn and TensorFlow: Concepts, Tools, and Techniques to Build Intelligent Systems*. O’Reilly Media, Inc., 1st ed., 2017. (Cited on page 67, 77)
- [116] J. Therhaag, *TMVA: Toolkit for multivariate data analysis*, *AIP Conf. Proc.* **1504** (2012) 1013. (Cited on page 68, 71)
- [117] ALICE Collaboration, *Measurement of dielectron production in central Pb-Pb collisions at $\sqrt{s_{NN}} = 2.76$ TeV*, *Phys. Rev. C* **99** (2019) 024002. (Cited on page 74, 81)
- [118] M. Abadi, A. Agarwal, P. Barham, E. Brevdo, Z. Chen and C. Citro, *TensorFlow: Large-scale machine learning on heterogeneous systems*, 2015. (Cited on page 77)
- [119] Y. Ganin, E. Ustinova, H. Ajakan, P. Germain, H. Larochelle, F. Laviolette et al., *Domain-Adversarial Training of Neural Networks*, *Journal of Machine Learning Research* **17** (2015) 1 [arXiv:1505.07818]. (Cited on page 77)
- [120] J. Shen, Y. Qu, W. Zhang and Y. Yu, *Wasserstein Distance Guided Representation Learning for Domain Adaptation*, arXiv:1707.01217. (Cited on page 77)
- [121] G. Louppe, M. Kagan and K. Cranmer, *Learning to pivot with adversarial*

networks, arXiv:1611.01046. (Cited on page 77)

- [122] I. Antcheva et al., *ROOT: A C++ framework for petabyte data storage, statistical analysis and visualization*, *Comput. Phys. Commun.* **180** (2009) 2499 [arXiv:1508.07749]. (Cited on page 78)
- [123] N. Jacazio, *Production of identified charged hadrons in Pb–Pb collisions at $\sqrt{s_{NN}} = 5.02$ TeV*, *Nucl. Phys.* **A967** (2017) 421 [arXiv:1704.06030]. (Cited on page 81)
- [124] ALICE Collaboration, *Production of $\omega(782)$ in pp collisions at $\sqrt{s} = 7$ TeV*, *ALICE-PUBLIC-2018-004* (2018) . (Cited on page 81)
- [125] ALICE Collaboration, *Production of $K^*(892)^0$ and $\phi(1020)$ in pp collisions at $\sqrt{s} = 7$ TeV*, *Eur. Phys. J.* **C72** (2012) 2183 [arXiv:1208.5717]. (Cited on page 81)
- [126] PHENIX Collaboration, *Detailed measurement of the e^+e^- pair continuum in p + p and Au+Au collisions at $\sqrt{s_{NN}} = 200$ GeV and implications for direct photon production*, *Phys. Rev.* **C81** (2010) 034911 [arXiv:0912.0244]. (Cited on page 81)
- [127] NA60 Collaboration, *Precision study of the $\eta \rightarrow \mu^+\mu^-\gamma$ and $\omega \rightarrow \mu^+\mu^-\pi^0$ electromagnetic transition form-factors and of the $\rho \rightarrow \mu^+\mu^-$ line shape in NA60*, *Phys. Lett.* **B757** (2016) 437 [arXiv: 1608.07898]. (Cited on page 81)
- [128] G. J. Gounaris and J. J. Sakurai, *Finite width corrections to the vector meson dominance prediction for $\rho \rightarrow e^+ e^-$* , *Phys. Rev. Lett.* **21** (1968) 244. (Cited on page 81)
- [129] ALICE Collaboration, *Measurement of D-meson production at mid-rapidity in pp collisions at $\sqrt{s} = 7$ TeV*, *The European Physical Journal C* **77** (2017) 550 [arXiv:1702.00766]. (Cited on page 82)
- [130] M. Cacciari, S. Frixione, N. Houdeau, M. L. Mangano, P. Nason and G. Ridolfi, *Theoretical predictions for charm and bottom production at the LHC*, *JHEP* **10** (2012) 137 [arXiv:1205.6344]. (Cited on page 82)
- [131] LHCb Collaboration, *Measurement of J/Ψ production in pp collisions at $\sqrt{s} = 7$ TeV*, *The European Physical Journal C* **71** (2011) 1645 [arXiv:1103.0423]. (Cited on page 82)

- [132] ALICE Collaboration, *J/Psi pT spectra in different centralities at $|y| < 0.9$, Public Preliminary Figure, To be published*. (Cited on page 83)
- [133] R. Rapp. Private communication (05.08.2019). (Cited on page 83)
- [134] M. Klusek-Gawenda. Private communication (09.08.2019). (Cited on page 84)
- [135] X. Zhangbu. Private communication (06.08.2019). (Cited on page 84)
- [136] S. Collaboration", *Low- p_T e^+e^- Pair Production in Au + Au Collisions at $\sqrt{s_{NN}} = 200$ GeV and U + U Collisions at $\sqrt{s_{NN}} = 193$ GeV at STAR, Phys. Rev. Lett. **121** (2018) 132301. (Cited on page 84)*
- [137] W. Zha, L. Ruan, Z. Tang, Z. Xu and S. Yang, *Double-slit experiment at fermi scale: coherent photoproduction in heavy-ion collisions, Phys. Rev. C* **99** (2019) 061901 [arXiv:1810.10694]. (Cited on page 86)
- [138] S. Lehner, *Dielectron production at low transverse momentum in Pb-Pb collisions at $\sqrt{s_{NN}} = 5.02$ TeV with ALICE, arXiv:1909.02508*. (Cited on page 95)
- [139] R. Barlow, *Systematic errors: Facts and fictions, Advanced Statistical Techniques in Particle Physics. Proceedings, Conference, Durham, UK, March 18-22, 2002* (2002) 134 [arXiv:hep-ex/0207026]. (Cited on page 100, 109, 110)
- [140] STAR collaboration, *Probing Extreme Electromagnetic Fields with the Breit-Wheeler Process, arXiv:1910.12400*. (Cited on page 113)
- [141] ALICE Collaboration, "Run2 integrated luminosity, Pb-Pb." <https://alice-figure.web.cern.ch/node/14883>, Accessed: 31.10.2019. (Cited on page 114)
- [142] ATLAS Collaboration, "Luminosity summary plots for 2018 PbPb data taking." https://twiki.cern.ch/twiki/bin/view/AtlasPublic/LuminosityPublicResultsRun2#Luminosity_summary_plots_for_AN1, Accessed: 02.10.2019. (Cited on page 114)
- [143] CMS Collaboration, "2018 lead-lead collisions at 5.02 TeV/nucleon "HI run"." https://twiki.cern.ch/twiki/bin/view/CMSPublic/LumiPublicResults#2018_lead_lead_collisions, Accessed: 02.10.2019, Accessed: 02.10.2019. (Cited on page 114)

- [144] O. Gould, “Magnetic monopole production in heavy ioncollisions.” Talk at "6th International Conference on New Frontiers in Physics (ICNFP 2017)", https://indico.cern.ch/event/559774/contributions/2676695/attachments/1509574/2353750/oliver_gould_crete_talk.pdf, Accessed: 02.10.2019. (Cited on page 114, 116)
- [145] S. Burdin, M. Horbatsch and W. Taylor, *A correction to Birks' Law in liquid argon ionization chamber simulations for highly ionizing particles*, *Nucl. Instrum. Meth.* **A664** (2012) 111. (Cited on page 116)
- [146] S. Biswas, *ALICE TPC upgrade for High-Rate operations*, *PoS ICPAQGP2015* (2017) 094 [arXiv:1511.04988]. (Cited on page 119)
- [147] A. Maire, *ALICE TPC sectors and pad rows*, *ALICE-PHO-SKE-2011-007* (2011) . (Cited on page 119)
- [148] M. Richter, *Data compression in ALICE by on-line track reconstruction and space point analysis*, *J. Phys. Conf. Ser.* **396** (2012) 012043. (Cited on page 118)
- [149] H. Weick, H. Geissel, N. Iwasa, C. Scheidenberger, J. L. Rodríguez-Sánchez, A. Prochazka et al., *Improved accuracy of the code ATIMA for energy-loss of heavy ions in matter*, *ATIMA_GSI_scientific_report_2017 – 5* (2018) . (Cited on page 121, 123)
- [150] A. V. Bagulya, M. S. Vladimirov, V. N. Ivanchenko and N. I. Starkov, *Heavy-particle energy loss simulation using the Geant4 toolkit*, *Bulletin of the Lebedev Physics Institute* **36** (2009) 127. (Cited on page 124)
- [151] H. Foidl, *Möglichkeiten der Suche nach magnetischen Monopolen mit ALICE*. Bachelor Thesis, University of Vienna, 2018. (Cited on page 124)

Personal Data

name Sebastian Lehner MSc
✉ Kohlgasse 47/41, 1050 Vienna, Austria
phone +43 (0)699/115 927 31
date of birth July 1, 1987 in Gmunden, Austria
citizenship Austria
email s.lehner@gmx.at

Professional Activities

- 08/15–ongoing **Scientific Assistant**, *Stefan-Meyer Institute for Subatomic Physics, Austrian Academy of Sciences, Vienna (AUT)*.
Data analysis of dielectron production with ALICE at LHC including development of machine learning applications and data driven analysis strategies
- 02/15–07/15 **Scientific Assistant**, *Universitätsklinik für Strahlentherapie, Medical University of Vienna, Vienna (AUT)*.
Studies of the dose deposition of C12 and O16 ion beams using Monte Carlo simulations
- 03/13–01/15 **Scientific Assistant**, *Stefan-Meyer Institute for Subatomic Physics, Austrian Academy of Sciences, Vienna (AUT)*.
Monte Carlo simulations for antihydrogen experiments
- 07/12–09/12 **Intern**, *CERN Summer Students Programme, Geneva (CH)*.
Characterization of novel superconductors and data analysis
- 10/11–07/12 **Lecture Assistant**, *Johannes Kepler University, Linz (AUT)*.
Lectures: “Atomic and Subatomic Physics” and “Waves, Optics and Photonics”
- 11/10–04/12 **Freelance Programmer**, *SLR Steyrermühl Logistik & Recycling GmbH, Laakirchen (AUT)*.
Development and maintenance of a database system based on VBA, SQL and MS Access

Education

- 08/15–ongoing **Doctoral Programme in Technical Physics,**
Doctoral Programme Particles & Interactions, FWF (08/15–08/18).
Technical University of Vienna, Vienna (AUT)
- 10/07–06/14 **Bachelor and Master Programme in Technical Physics.**
Johannes Kepler University, Linz (AUT) (DI/MSc, graduation with distinction)
- 09/98–06/06 **Secondary School.**
Bundesrealgymnasium Gmunden, AUT

Selected Publications, Talks, Posters and Theses

Publications

- 2019 S. Lehner, *Dielectron production at low transverse momentum in Pb–Pb collisions at $\sqrt{s_{NN}} = 5.02$ TeV with ALICE*, arXiv:1909.02508
- 2019 ALICE Collaboration, *Phys.Rev. C99 (2019) no.2, 024002, Measurement of dielectron production in central Pb-Pb collisions at $\sqrt{s_{NN}} = 2.76$ TeV*, arXiv:1807.00923

- 2019 ALICE Collaboration, Phys.Lett. B788 (2019) 505-518, *Dielectron and heavy-quark production in inelastic and high-multiplicity proton-proton collisions at $\sqrt{s_{NN}} = 13$ TeV*, arXiv:1805.04407v2
 - 2018 ALICE Collaboration, JHEP 1809 (2018) 064, *Dielectron production in proton-proton collisions at $\sqrt{s} = 7$ TeV*, arXiv:1805.04391v2
 - 2014 AEGIS Collaboration, Nature Commun. 5 (2014) 4538, *A Moire deflectometer for antimatter*
Talks and Posters
 - 2019 Talk at the Large Hadron Collider Physics Conference 2019, Puebla, MEX.
Low-Mass Dielectrons in pp, p-Pb and Pb-Pb Collisions at ALICE
 - 2018 Poster at Quark Matter 2018, Venice, ITA.
Multivariate background suppression in the low-mass dielectron analysis in Pb-Pb collisions at $\sqrt{s_{NN}} = 5.02$ TeV with ALICE
 - 2018 Talk at the Seminar for High Energy Nuclear Physics, University of Heidelberg, GER.
Machine Learning Methods in the Analysis of Low-Mass Dielectrons
 - 2018 Talk at the MoEDAL Collaboration Meeting at CERN, Geneva, CH.
A Magnetic Monopole Search in Pb-Pb Data
 - 2017 Poster at Quark Matter 2017, Chicago, USA.
Machine Learning Based Analysis of Low-Mass Dielectrons
 - 2016 Talk at the ALICE Machine Learning Meeting at CERN. Geneva, CH.
Machine Learning Based Conversion Rejection in the Analysis of Low-Mass Dielectrons
- Theses
- 2019 Dissertation: *Dielectron Production and the Search for Highly-Charged Particles in Pb-Pb Collisions*, Supervisors: Prof. Dr. Eberhard Widmann and Dr. Michael Weber
 - 2014 Master Thesis: *Beam Optics Simulations and Thermal Shielding for the AEGIS Antihydrogen Experiment*, Supervisor: Prof. Dr. Peter Bauer

Languages

german Mother tongue
english C1
french B1

Professional Interests & Skills

General Data Analysis, Particle Physics, Machine Learning, Deep Learning, Statistics, Causal Inference, Scientific Outreach and SciComm, Simulation

Programming C++, Python, scikit-learn, Keras, TensorFlow, NumPy, Pandas, git, ROOT, TMVA

Personal Interests

Mountaineering, Beachvolleyball, Surfing, Reading, Travelling